Stochastic variational approach to interaction of atoms and strong external fields

By

Jorge Alberto Salas

Dissertation

Submitted to the Faculty of the

Graduate School of Vanderbilt University

in partial fulfillment of the requirements

for the degree of

DOCTOR OF PHILOSOPHY

in

Physics

August 31, 2017

Nashville, Tennessee

Approved:

Andreas Berlind, Ph.D.

Thomas Weiler, Ph.D.

Gregory Walker, Ph.D.

Richard Haglund, Ph.D.

Kalman Varga, Ph.D.

TABLE OF CONTENTS

LIST OF TABLES

LIST OF FIGURES

CHAPTER 1

INTRODUCTION

The study of problems involving few particles has always been a topic of interest since the discovery of quantum mechanics. Throughout the years researchers have sought methods for efficiently solving the Schrödinger equation for these systems computationally[1].

One of the problems commonly studied in quantum mechanics is the stability of few particle systems for a given type of interaction such as Coulomb, gravitational, Van der Waals, electric and magnetic fields, among others. Stability can be determined not just by the interacting force, but also by the fermionic or bosonic nature of the particles. For example, a system of 3 negative and 2 positive charges is unbound if the particles are fermions (electron-positron), but if they were bosons then the system would be bound, despite them having the same forces acting upon them [2].

Throughout the years researchers have sought methods for efficiently solving the Schrödinger equation. Numerical calculations to solve it in many cases involve the use of grids [1]. However such methods have their limitations and are restricted to systems with few degrees of freedom due to high computational costs. For systems with few particles it is often possible to expand the wavefunction in a suitable basis and apply the variational principle. Many types of basis functions are available, and some of the most popular choices are the Hylleraas [3] and Gaussian basis [4], with the latter being the main focus of the present work, in conjunction with the Stochastic Variational Method.

The Gaussian functions have proven to be valuable due to their mathematical properties. In quantum mechanics Gaussain wavepackets are important because they give the minimum uncertainty admisible under the Heisenberg principle [5], and they are also used to for solving electron scattering problems (e.g. See Salas et. al. [6]). Additional properties of Gaussians include the possibility of calculating matrix element integrals analyti-

cally. It is possible to employ different forms of Gaussians, such as with variable widths or shifted origins and use them in cartesian, cylindrical or spherical coordinates [1]. They are therefore versatile wavefunctions that can be used together with the Stochastic Variational Method for computing energies.

One of the systems that has received lots of attention in computational atomic physics is the helium atom for multiple reasons. One of the main ones is that it has only two electrons, and therefore it is simple to represent with basis functions.

For the case of a two-electron system the critical nuclear charge needed to achieve stability has been calculated to be $Z_{2e} = 0.910850$ (see Ref. [7]), rendering helium a stable atom. However, for the case of a three-electron system the critical nuclear charge to make it bound has been calculated to be $Z_{3e} = 2.0090$ (See Ref.[7]), which would mean that helium would not be able to form stable negative ions, unless the conditions changed. Nevertheless there are other ways that it could form stable structures.

Helium is known as a noble gas because its lack of reactivity to form compounds. It's few known compounds form under exotic conditions such as high pressure or low temperatures. The most recently discovered helium compound consists of sodium and helium formed at high pressures, above 113 GPa [8]. Helium atoms can interact by means of the Van der Waals forces [9], but such interactions are so weak that they are only significant for low temperatures. Even at absolute zero He^3 and He^4 do not solidify in the absence of external pressure because of the zero-point energy motion [9]. This property is due to its relatively low mass, which fails to keep the nuclei near their equilibrium position, unlike other inert atoms of higher mass. However for the case of He^4, a boson, it is possible to obtain structures known as Efimov trimers due to the bosonic nature, but very low temperatures are required [10].

Advances in low temperature physics have allowed the experimental observation of phenomena that were long predicted ago such as the formation of Efimov states, Bose-Einstein condensates as well as Wigner crystals. The study of such phenomena requires

methods for making accurate calculations for these systems. In Chapter 3 we show the use of the Stochastic Variational Method for calculations of few boson systems.

Since the 1960's theoretical works have suggested a different mechanism under which helium can form a negative ion. Under very strong magnetic fields, the electronic structure of atoms can change drastically, and under such conditions it has been predicted that He^- becomes stable. Moreover atoms in general are predicted to drastically change their properties under such fields. The discovery of very strong magnetic fields in celestial bodies such as neutron stars has prompted research into the behavior of atoms under such conditions. In the present work we computationally explore these effects for the case of small systems in Chapter 4.

A Gaussian basis can also be used for simulating interactions with electric fields, which in combination with time-dependent methods can be used to simulate absorption and emission of radiation and High Harmonic Generation. This simulation can be done by representing the eigenstates of the system, as well as the dipole moments. However, the Stochastic Variational Method is best for ground or low excited states, rather than Rydberg or unbound because the accuracy of each one depends on that of the states below (See for example Ref.[11]).

On the other hand, there exists a Gaussian basis set, known as the Kaufmann basis, which is good for scattering states, but not very accurate for ground states. In Chapter 5 we use the Stochastic Variational Method to enhance the Kaufmann basis and use it for simulations with strong laser fields. In particular we show the Mollow sideband generation for the hydrogen atom and the effects on the higher harmonics, going beyond the typical 2-level models. We also confirm our results with a separate method consisting of a confined hydrogen model.

CHAPTER 2

FORMALISM

This chapter is organized as follows: We first give an introduction to the Hamiltonian for different potentials in section 2.1 and to the variational principle in 2.2. Then an overview of the Hylleraas basis is given in 2.3, followed by the Explicitly Correlated Gaussians 2.4 and their deformed variant in 2.5. Finally the Stochastic Variational Method is explained in 2.6.

2.1 Hamiltonian

The Hamiltonian of a nonrelativistic Coulombic N-particle system is defined as

$$H = \sum_{i=1}^{N}\left(-\frac{\hbar^2}{2m}\nabla_i^2\right)+\sum_{i}^{N}U_i(r_i)+\sum_{i<j}^{N}V_{ij}(r_{ij}), \tag{2.1}$$

where U_i is the single-particle potential and V_{ij} the two-body interaction, with specific forms to be specified for each case individually.

2.1.1 Center of mass reduction

If there are no external fields present it is natural to separate the center of mass motion from the intrinsic one of the system, which can be achieved by the use of a relative coordinate system [12]. Two common choices are the Jacobi coordinates and one where the origin is placed on one of the particles[13].

The laboratory frame coordinates $(\mathbf{x}_1,\mathbf{x}_2,\ldots,\mathbf{x}_N)$ and the relative (Jacobi) coordinates $(\mathbf{r}_1,\mathbf{r}_2,\ldots,\mathbf{r}_N)$ ($\mathbf{r}_N$ is the position of the center of mass, $\mathbf{r}_{\rm cm}$) are related by [12]:

$$\mathbf{r}_i=\sum_{j=1}^{N}\Omega_{ij}\mathbf{x}_j,\qquad \mathbf{x}_i=\sum_{j=1}^{N}(\Omega^{-1})_{ij}\mathbf{r}_j,\qquad i=1,\ldots,N. \tag{2.2}$$

For the case of the Jacobi coordinates the transformation matrix Ω is [12]:

$$\Omega_{\text{Jac}} = \begin{pmatrix} 1 & -1 & 0 & \cdots & 0 \\ \frac{m_1}{M_2} & \frac{m_2}{M_2} & -1 & \cdots & 0 \\ \vdots & \vdots & \vdots & \ddots & \vdots \\ \frac{m_1}{M_{N-1}} & \frac{m_2}{M_{N-1}} & \frac{m_3}{M_{N-1}} & \cdots & -1 \\ \frac{m_1}{M_N} & \frac{m_2}{M_N} & \frac{m_3}{M_N} & \cdots & \frac{m_N}{M_N} \end{pmatrix}. \tag{2.3}$$

The transformation matrix for relative coordinates respect to particle 1 is:

$$\Omega_{\text{rel}} = \begin{pmatrix} -1 & 1 & 0 & \cdots & 0 \\ -1 & 0 & 1 & \cdots & 0 \\ \vdots & \vdots & \vdots & \ddots & \vdots \\ -1 & 0 & 0 & \cdots & 1 \\ \frac{m_1}{M_N} & \frac{m_2}{M_N} & \frac{m_3}{M_N} & \cdots & \frac{m_N}{M_N} \end{pmatrix}, \tag{2.4}$$

where

$$M_k = \sum_{i=1}^{k} m_i. \tag{2.5}$$

It is also possible to write out the inverse transformation explicitly[12, 13]. Placing the origin on one of the particles can be a natural choice in many situations, such as when one of them much more massive than others (i.e. an atom, which has massive nucleus and electrons that are significantly less heavier) [12].

The corresponding linear momenta $\mathbf{p}_i$, conjugated to Jacobi or particle-1 relative coordinates $\mathbf{r}_i$, are obtainable by means of the application of the inverse transformation:

$$\mathbf{p}_i = \sum_{j=1}^{N} (\Omega^{-1})_{ij} \mathbf{q}_j, \quad \mathbf{q}_i = \sum_{j=1}^{N} \Omega_{ij} \mathbf{p}_j, \quad i = 1, \ldots, N, \tag{2.6}$$

where $\mathbf{q}_i = m_i \mathbf{x}_i$. Upon executing a coordinate transformation using the relations in Eq. (2.3) or (2.4), the resulting kinetic energy operator T of the new Hamiltonian will contains

two terms: the kinetic energy of $n = N - 1$ (pseudo)particles motion respect to the new reference frame and the kinetic energy of the center of mass [12]:

$$T = \frac{1}{2} \sum_{i,j=1}^{n} \Lambda_{ij} \mathbf{p}_i \cdot \mathbf{p}_j + T_{\mathrm{cm}}, \tag{2.7}$$

where Λ is a $n \times n$ "mass" matrix with the corresponding elements

$$\Lambda_{ij} = \sum_{k=1}^{N} \frac{1}{m_k} \Omega_{ik} \Omega_{jk}. \tag{2.8}$$

The center of mass kinetic energy operator is given by

$$T_{\mathrm{cm}} = \frac{\mathbf{p}_{\mathrm{cm}}^2}{2M_{\mathrm{N}}}. \tag{2.9}$$

In the absence of external fields the potential can only depend on the inter-particle coordinates, so the total Hamiltonian of the system in the new coordinates will be independent of $\mathbf{r}_{\mathrm{cm}}$. The total wavefunction can therefore be represented as a product between a plane wave, corresponding to the motion of the system as a whole, and a wavefunction ψ describing the intrinsic motion [12]:

$$\psi_{\mathrm{tot}} = \exp(i\mathbf{p}_{\mathrm{cm}} \cdot \mathbf{r}_{\mathrm{cm}}) \psi(\mathbf{r}_1, \ldots, \mathbf{r}_n). \tag{2.10}$$

Afterwards the focus is on approximating the intrinsic wave function.

2.2 Variational Principle

The variational method allows the calculation of an upper bound for the energies of a quantum system. It is based upon the variational principle [5, see ch 7]. This can be formulated as follows. Let ψ be an arbitrary normalized wavefunction that satisfies the required boundary conditions of the system. Then the ground state of the system, E_{gs}, is always

lower or equal to the expectation value of the Hamiltonian in that arbitrary wavefunction:

$$E_{gs} \leq \langle \psi | \hat{H} | \psi \rangle. \tag{2.11}$$

The wavefunction in Eq. (2.11) is referred to as a *trial* wavefunction, and the degree of accuracy of the method relies on how closely it resembles the ground state. The strategy employed to obtain the minimum energy possible consists in using a trial function that depends on some adjustable parameter, and then vary the parameter to obtain the value for which the expectation value is minimized.

For greater accuracy the trial wavefunction can be constructed as a linear combination of N basis functions ϕ_i, as in Eq. (2.12). Each of the basis functions has its own variational parameter α_i that can be adjusted individually.

$$\psi_{trial} = \sum_{i=1}^{N} c_i \phi_i, \tag{2.12}$$

2.2.1 Generalized method

It is also possible to calculate energies for the excited states, although the method has its limitations. In general the energies of the system can be obtained by solving the generalized eigenvalue problem [1, 13].

$$Hc_k = \varepsilon_k S c_k, \tag{2.13}$$

In Eq. (2.13) ε_k and c_k are the eigenvalues and eigenvectors respectively, H is the Hamiltonian matrix with elements given by

$$H_{ij} = \langle \phi_i | \hat{H} | \phi_j \rangle, \tag{2.14}$$

S is the overlap matrix:

$$S_{ij} = \langle \phi_i | \phi_j \rangle, \tag{2.15}$$

If the energies of the system are sorted so that $E_{k+1} > E_k$, and the eigenvalues $\varepsilon_{k+1} > \varepsilon_k$, then the eigenvalues form upper bounds for each energy such that:

$$\varepsilon_k \geq E_k, \ \forall k. \tag{2.16}$$

One disadvantage of the method is that the accuracy of any given state depends on how well converged are the ones below, so obtaining an accurate excited state can demand a very large basis.

For the calculation of the eigenvalues, it is necessary to compute the matrix elements Eq. (2.14) and (2.15). These calculations involve integrals that can sometimes be computed numerically, but in many cases this can be unfeasible (especially when there are multiple particles in the system). Usually it is desirable to have functions that permit this to be done analytically.

Some of the most popular basis functions are: Gaussians [14, 15], Hylleraas [16] and plane waves[1] because they allow such analytical calculations. The choice of basis functions will greatly influence the accuracy of the results. The chosen functions should have the same symmetry as the actual wavefunction to enable good convergence with less basis functions.

2.3 The Hylleraas basis

The Hylleraas basis [17], has been used for a long time, since the early days of quantum mechanics [18] but yet remains to be a method of the greatest importance in the present due to its good accuracy and analytical integration of the matrix elements.
The Hylleraas expansion is given by [17]:

$$\psi(s,u,t) = e^{-1/2s} \sum_{n,l,m} C_{n,l,m} s^l u^m t^n, \tag{2.17}$$

where $C_{n,l,m}$ is a constant.

For a two electron atom the Hylleraas basis Eq.(2.17) is defined in terms of the coordinates are $u = r_1 + r_2$, $u = r_1 - r_2$, $t = r_{12}$, with

$$r_{12} = \sqrt{r_1^2 + r_2^2 - r_1 r_2 \cos(\theta_{12})}. \tag{2.18}$$

The variable θ_{12} in Eq.(2.18) is the angle between $\vec{r}_1$ and $\vec{r}_2$.

The expansion can be generalized for many electrons, but its is not straightforward to do so. Performing calculations with $N \geq 5$ electrons is now possible due to the existence of symbolic algebra software packages [17].

The Hylleraas approach has been vastly used to investigate lithium ground state energies [17]. With a 1589-term expansion it is possible to obtain an energy with 11 significant decimals[17]. Calculations have also been done for isoelectronic ions [19, 20], as well as larger systems such as beryllium and boron [17].

A Hylleraas-like wavefunction for three electron systems is given by:

$$\psi(\vec{r}_1, \vec{r}_2, \vec{r}_3) = r_1^{j_1} r_2^{j_2} r_3^{j_3} r_{12}^{j_{12}} r_{13}^{j_{13}} r_{23}^{j_{23}} \exp(-\omega_1 r_1 - \omega_2 r_2 - \omega_3 r_3) \mathscr{Y}^{L,M_L}_{(l_1 l_2) l_{12}, l_3}(\vec{r}_1, \vec{r}_2, \vec{r}_3), \tag{2.19}$$

where the j's are integers, ω_i are non-linear variational parameters and $\mathscr{Y}$ are vector-coupled product of spherical harmonics:

$$\mathscr{Y}^{L,M_L}_{(l_1 l_2) l_{12}, l_3}(\vec{r}_1, \vec{r}_2, \vec{r}_3) = r_1^{l_1} r_2^{l_2} r_3^{l_3} \sum_{m_1, m_2, m_3} \langle l_1 m_1; l_2 m_2 | l_1 l_2; l_{12} m_{12} \rangle \langle l_{12} m_{12}; l_3 m_3 | l_{12} l_3; L M_L \rangle \times$$
$$Y_{l_1, m_1}(\hat{r}_1) Y_{l_2, m_2}(\hat{r}_2) Y_{l_3, m_3}(\hat{r}_3) \tag{2.20}$$

2.4 Explicitly Correlated Gaussians (ECG)

For a system with n particles the general form of the ECG is given in Cartesian coordinates by

$$G(\mathbf{x}_1 ... \mathbf{x}_n) = \exp\left(-\frac{1}{2}\sum_{i,j=1}^{n} A_{ij}\mathbf{x}_i \cdot \mathbf{x}_j\right), \tag{2.21}$$

where A_{ij} is a variational parameter and $\mathbf{x}$ is the position vector.

It is also possible to employ spherical coordinates and have each basis function be the product of Spherical Gaussian-Type Orbitals (SGTO) [14]. However, for systems with interacting particles the SGTO can have a slow convergence of the variational energy. An improvement consists on using Explicitly Correlated Gaussians in Spherical coordinates, which give a faster convergence. For a system of n particles they are given by

$$\phi_k = \exp\left(-\frac{1}{2}\sum_{i,j=1}^{n} A_{ij}(\mathbf{r}_i - \mathbf{r}_j)^2\right)\prod_{j=1}^{n} r_j^{l_j} Y_{l_j m_j}(\hat{r_j}), \tag{2.22}$$

where $\mathbf{r}_i$ is the position vector for particle i, Y_{lm} is a spherical harmonic [15].

This basis has the advantage of having matrix elements that are analytically available for the overlap, kinetic energy and multiple potentials [15]. Also it has more variational parameters than SGTOs allowing a faster convergence with less basis functions.

Another advantage is that the permutation symmetry of the wavefunction can be easily imposed, and be made either symmetric or anti-symmetric and coupled to an appropriate spin wavefunction as needed.

2.4.1 Matrix elements

An important feature of the ECG based methods is the simplicity of the matrix elements of the Hamiltonian as well as other operators [12]. We take take for example the overlap between two spherically symmetric ECGs, defined in Eq. (2.21). Let, det(...) and tr(...)

denote the determinant and trace of a matrix, respectively. We then have:

$$S(A_k,A_l) \quad = \quad \langle G(A_k)|G(A_l)\rangle = \left(\frac{\pi^n}{\det(A_{kl})}\right)^{\frac{3}{2}}, \tag{2.23}$$

where $A_{kl} = A_k + A_l$. The kinetic energy matrix element has the following form:

$$\langle G(A_k)|T|G(A_l)\rangle = 3\mathrm{tr}\left(A_k A_{kl}^{-1} A_l \Lambda\right) S(A_k,A_l). \tag{2.24}$$

Any one-body operator, based on the spatial coordinate, has matrix elements that can be written as [12]

$$\langle G(A_k)|V(\mathbf{r}_i)|G(A_l)\rangle = I(\beta_i)S(A_k,A_l). \tag{2.25}$$

where $I(\beta)$ is defined by [12]

$$I(\beta) = \left(\frac{\beta}{\pi}\right)^{\frac{3}{2}} \int V(\mathbf{a}) \exp\left(-\beta a^2\right) d\mathbf{a} \tag{2.26}$$

and

$$\frac{1}{\beta_i} = w_i' A_{kl}^{-1} w_i, \tag{2.27}$$

where w_i is a vector with elements $w_i = \delta_{im}$. A two body interaction $V(\mathbf{r}_i - \mathbf{r}_j)$ matrix elements can be expressed in a similar way to Eq. (2.25):

$$\langle G(A_k)|V(\mathbf{r}_i - \mathbf{r}_j)|G(A_l)\rangle = I(\beta_{ij})S(A_k,A_l), \tag{2.28}$$

but with

$$\frac{1}{\beta_{ij}} = w_{ij}' A_{kl}^{-1} w_{ij}, \qquad w_{ij} = \delta_{im} - \delta_{jm}. \tag{2.29}$$

The functional form of the potential has almost no restrictions. For the particular case of central interactions the integral of Eq. (2.26) is reduced to an integral in one-dimension, and can be easily evaluated either analytically or by numerical methods. For example, for

the case of power law potentials, $V(r) = r^k$ ($k > -3$), one obtains

$$I(\beta) = \frac{2}{\sqrt{\pi}\beta^{\frac{k}{2}}}\Gamma\left(\frac{k+3}{2}\right), \tag{2.30}$$

where Γ is the Euler gamma function [12]. Another property important of the ECG basis is that the analytical complexity of the matrix elements does not change when the number of particles is increased, unlike the Hylleraas basis. The computational effort done to evaluate the matrix elements, for pairwise interactions, increases as as $n^3 \times k!$, where k is the number of identical particles in the system (for an atom, $k = n$). The $k!$ factor comes from antisymmetrizing the wave function, and its dependence has limited the application of ECG methods to systems few particles [12].

2.5 Deformed ECG's

For problems that have cylindrical symmetry, such as those with external fields, the form Eq. (2.22) may not be the best choice. An alternative is to use a deformed form of the correlated Gaussians (DCG), which is defined in terms of cylindrical coordinates [12, 13]:

$$\exp\left\{-\frac{1}{2}\sum_{i,j=1}^{N} A_{ij}\rho_i \cdot \rho_j - \frac{1}{2}\sum_{i,j=1}^{N} B_{ij} z_i \cdot z_j\right\}, \tag{2.31}$$

where the nonlinear parameters A_{ij}, B_{ij} can be different and are independent in both the radial and vertical direction.

For a system with no external torques along the z axis, the angular momentum operator L_z has its corresponding eigenvalue M conserved. The form of the DCG in Eq. (2.31) belongs to $M = 0$ and can be extended to allow for $M \neq 0$ states multiplying the basis by

$$\prod_{i=1}^{N} \xi_{m_i}(\rho_i), \tag{2.32}$$

where

$$\xi_m(\rho) = (x+iy)^m. \tag{2.33}$$

Thus the spatial variational trial function is then

$$\Phi_M(\mathbf{r}) = \left(\prod_{i=1}^{N} \xi_{m_i}(\rho_i)\right) \exp\left\{-\frac{1}{2}\sum_{i,j=1}^{N} A_{ij}\rho_i \cdot \rho_j - \frac{1}{2}\sum_{i,j=1}^{N} B_{ij} z_i \cdot z_j\right\}, \tag{2.34}$$

where $M = m_1 + m_2 + ... + m_N$, and m_i are integers.

2.5.1 Correlation and inter-particle distances

A quantity of interest for many systems is the average value of the distances between particles or from the origin, since they yield information on the structure. These can be obtained by means of the correlation function, which is defined as:

$$C(\mathbf{r}) = \langle \Psi | \sum_{i<j}^{N} \delta(\mathbf{r}_i - \mathbf{r}_j - \mathbf{r}) | \Psi \rangle. \tag{2.35}$$

Using $C(r)$, the radial part of the correlation function, the powers of interparticle distances are given by

$$< r^k >= \int_0^\infty r^k C(r) dr. \tag{2.36}$$

Similarly Eq. (2.35), (2.36) can be also defined for single particles, by instead considering the distance from the origin of coordinates.

2.6 Stochastic Variational Method (SVM)

The variational approach is employed selecting the optimal parameters capable of minimizing the eigenvalues in Eq. (2.13). More in depth explanations can be found in Refs[12, 13]. A problem with increased number of parameters is that multi-variable optimization can be a complicated task [13]. The Stochastic Variational Method (SVM) consists in selecting values for the nonlinear parameters at random and keeping the ones that minimize

the energy. The algorithm is divided in two stages: increasing the size of the basis, and refining an existing one, both briefly described below.

2.6.1 Increasing a basis

Given a starting basis of size N, the goal is to increase the basis to size N+1 by finding an additional basis function that will reduce the eigenvalue ε. The variational principle guarantees that the addition of an additional basis function will not make the eigenvalue value increase. A set of many candidate nonlinear parameters are generated at random and tested. Whichever gives the smallest eigenvalue is then kept as the new basis function. A more detailed explanation can be found in Ref. [13].

2.6.2 Refining a basis

In the next stage the basis size remains a constant and another pool of candidate functions is generated. The existing basis functions are then swapped by turns with candidate ones and the eigenvalue is checked. Whichever of the two functions gives the lowest eigenvalue is kept.

It is important to take into account that the variational principle can fail in the event of numerical accuracy problems, which can arise due to over-completeness of the basis. Countermeasures can be taken to avoid over-completeness, such as discarding any candidate functions that give a high overlap with existing ones [13]. Afterwards, further increases of the basis and subsequent refinements are possible until an adequate basis size with a satisfactory eigenvalue is obtained.

CHAPTER 3

FEW-BOSON SYSTEMS

In the present chapter the Stochastic Variational Method is used to study systems with few bosons, with different types of interactions. The chapter is organized as follows: we first present the motivation for this study in 3.1. We then present the results in 3.2 and the conclusions in 3.3. The work described in the chapter was published in Ref.[21], and reproduced with permission from the publisher.

3.1 Motivation

The recent experimental activity studying dilute ultracold atomic and molecular systems [22–28] has produced theoretical interest in few-body systems composed of bosons [23, 29–46].

The investigation of bosonic systems covers many different subjects ranging from atom interferometry to quantum universality: Efimov state governed phase transitions [27], dynamics of degenerate Bose-gas [28], halo states [45], and physics of bosons in harmonic traps [47, 48] have been studied. The accurate solution of quantum mechanical few-body problems is an indispensable tool in this research field.

Diverse theoretical and computational approaches have been previously used to calculate the energy levels and structure of few-boson systems. The Gaussian variational [43, 49], and hyperspherical [29, 37, 38, 41, 42] calculations are the most popular approaches. There are many benchmark calculations to check the accuracy and efficiency of computational approaches for fermionic few-particle systems, e.g. for atoms and molecules [2, 13]. The number of test systems as well as test calculations for few-boson cases is much less. The goal of this chapter is to provide benchmark calculations for N bosons. In addition to the energies, the particle-particle distances and correlation functions are also calculated

in order to add extra information that can be compared for different approaches.

3.1.1 He-He molecule

Helium atoms, due to their noble gas nature, are well known for their lack of stable negative ions and molecules, but exceptions do exist to this behavior [8]. Few body systems formed of helium atoms have been a subject of theoretical and experimental work [50]. The He-He molecule has been verified experimentally. Due to its large scattering length this molecule is one of the largest diatomic molecules in existence [50].

Multiple model potentials have been proposed to describe the helium dimer interactions. Such potentials are attractive, but become highly repulsive at close range [50], becoming problematic for the purpose of calculations. The nature of the potential limits the calculations of multiple He atoms. Although some methods have been employed for this purpose [51], most calculations only address the case of three helium atoms [50].

The LM2M2 potential is an example of these potentials [51–53]. It is obtained ab-initio, and is known to give reasonable agreement with experimental observations, despite small discrepancies [53].

Systems with more than two helium atoms can be difficult to describe, because the kinetic and potential energy present a large cancellation and the bound state is very shallow [54].

A *soft-core* potential employed is an attractive Gaussian shaped given by [50, 54]:

$$V(r) = V_0 e^{-r^2/R^2}, \tag{3.1}$$

with $V_0 = 1.227$ K and $R = 10.03$ a.u. This potential can be considered a regularized form of LM2M2 [53], and despite being an effective field approximation, it is capable of giving reasonable agreement with experimental results [50]. Both LM2M2 and Gaussian predict similar scattering lengths, effective range and phase shifts in the low energy limit [50].

However the Gaussian potential is much easier to use for calculations.

The potential Eq.(3.1) has been used to investigate the three ^{4}He system [54], as well as the spectra of helium clusters with up to six atoms[50]. Since these few atom systems have long scattering lengths, they are in the regime where the Efimov [55] effect takes place, which we will describe in section 3.1.2.

3.1.2 Efimov states

One of the topics that has recently received much attention in low temperature physics is the formation of Efimov states. They have attracted so much interest due to their strange and counterintuitive properties, the large difficulty to observe them experimentally and their close relationship to Bose Einstein Condensation, among other reasons [56].

In 1971 Vitaly Efimov studied the bound states of three identical bosons and predicted the possibility that three particles could form a bound state whereas only two of them would be otherwise unbound [57]. Furthermore the system would have an infinite number of bound states, currently known as Efimov states. A typical analogy to understand Efimov states are the Borromean rings, which are linked together such that if one of them is removed they all become unbound [56]. This type of behavior is independent of the type of interaction between the particles [56]. Also, the model predicts an infinite number of bound states with the following property: upon scaling the length by a factor of 22.7 another state is found such that its length is larger by that same factor, but its energy is diminished by a factor of 22.7^2 [56].

Efimov's prediction was investigated for many years. Observation of the Efimov resonance was made in Insbruck in 2002 during attempts to obtain a Bose-Einstein condensation, but the work was not published and the effect was not identified at the time [56]. It was not until 2006 when the experimental observation was confirmed and published using Caesium atoms [56, 58].

Further research has also focused on the universality of the effect and the existence of

trimers with more particles. Four-body states have also been found [59, 60]. Higher Efimov states had still yet to be observed. That discovery was not an easy task because the binding energy of the state is strongly diminished for excited states, so lower temperatures must be reached in order to keep the system stable. In 2014 this was finally done, with a measured scaling factor close to the predicted one [61].

Throughout the years Helium has been an important candidate for the formation of Efimov states. Many theoretical works addressed this problem, but experiments on molecular beams were unable to confirm the predictions [56]. However, the formation of Helium trimers was finally observed and published in 2015 [10]. This was done by means of Coulomb explosion imaging. The observed size matched the predicted one, and it showed that the structure is such that two atoms are close to each other and the third one is far away.

3.1.3 Wigner Crystals

Eugene Paul Wigner conjectured that when the density of electrons in a metal is low enough the Coulomb potential dominates over the kinetic energy, making the electrons localize by forming a crystalline structure [62]. In his model the electrons oscillate around their equilibrium positions even in the ground state, and can happen when the density is low, $n_e \ll 1$ [62].

Observation of Wigner crystals is not easy, but has been achieved experimentally after more than forty years [62]. Its first experimental observation was obtained in a classical 2D Coulomb system formed by a monolayer of electrons trapped in a potential well above the surface of liquid helium [63].

3.2 Solutions for few body systems

In addition to the energies, particle-particle distances and correlation functions are also calculated to add extra information that can be compared for different approaches.

The Hamiltonian for the N-boson system is given by (2.1). The variational method was

N	E	$E_{literature}$	$< r^{-1} >$	$< r >$	$< r^2 >$
2	-0.001296	-0.001296[a]	0.026	98.490	18065.006
3	-0.15042	-0.1504[a]	0.088	16.346	355.849
4	-0.75138	-0.75137[a]	0.113	11.827	173.745
5	-1.94522	-1.9452[a]	0.130	10.105	124.212
6	-3.81093	-3.8109[a]	0.143	9.114	100.129
7	-6.40326		0.154	8.442	85.463
8	-9.76331	-9.7633[b]	0.163	7.943	75.419
9	-13.9232		0.171	7.552	68.022
10	-18.9102	-18.910[b]	0.178	7.235	62.334

Table 3.1: Energies (in Kelvin) and average powers of inter-particle distances (in a.u.) of bosons interacting via soft-core Gaussian potential. Results are compared to [a] Ref. [50] and [b] Ref. [37]. (Source: Horne, Salas & Varga 2014 [21])

used with a trial function consisting of Explicitly Correlated Gaussians, given by Eq. (2.21) and are symmetrized to give the bosonic behavior [4, 13].

3.2.1 Bosons with Soft core Gaussian interaction

In this scenario there is no external field $(U(r) = 0)$ in Eq.(2.1) and the interaction is given by the soft core model in Eq.(3.1).

The results for the ground state N boson systems are given in Table 3.1, obtained from Ref.[21]. It can be seen that the potential has a very weakly bound ground state for the two-body case. The scattering length is vary large as expected and diminishes rapidly upon the addition of particles. The correlation function is shown in Fig. 3.1 and it illustrates the long scattering lengths.

As the number of particles increases the size of the system diminishes. This behavior can be observed in Table 3.1 and in Fig 3.2, where the peaks approach the origin as N increases. Additionally, the binding energies also increase due to the increase in attractive pairs.

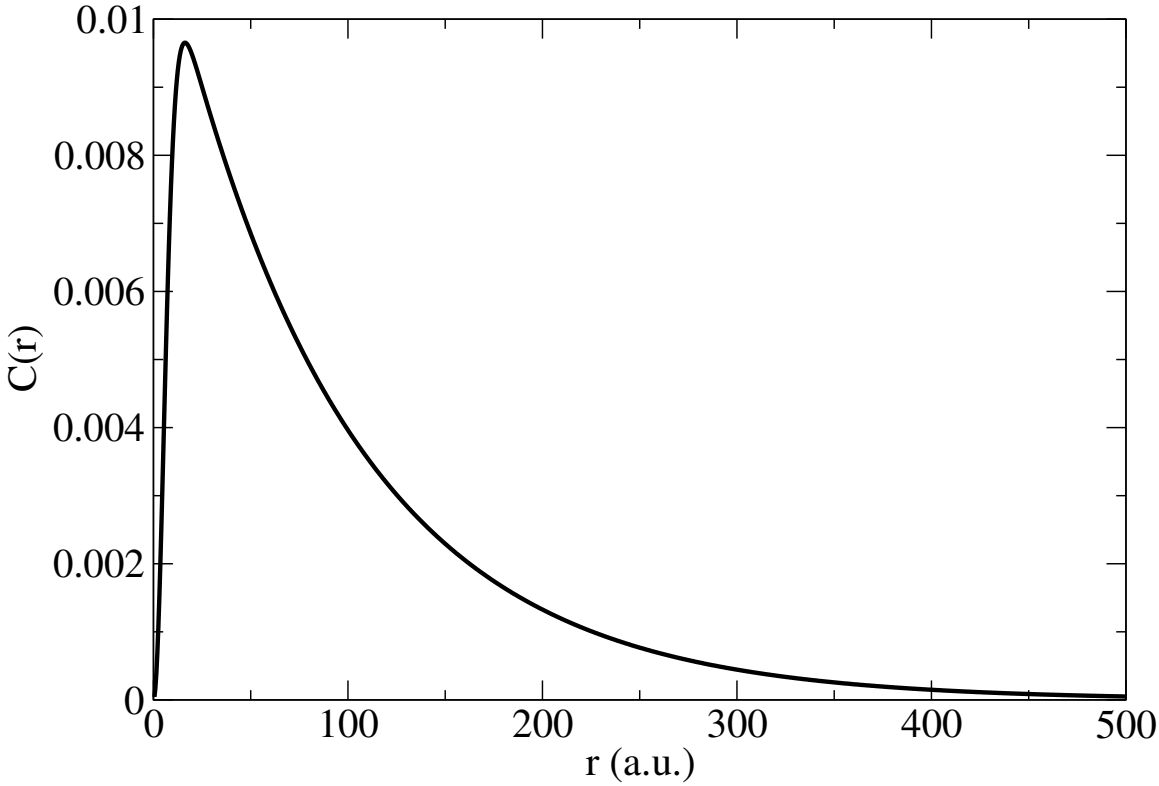

Figure 3.1: Correlation function for N=2 bosons interaction via a soft-core Gaussian potential. (Source: Horne, Salas & Varga 2014 [21], ©Springer-Verlag Wien 2014 with permission of Springer.)

The results agree with those obtained with other methods in the literature. The present method is that it can be easily employed for more particles, although there is a limitation due to the $N!$ growth of the computational time due to the symmetrization.

3.2.2 Bosons with Coulomb interaction

In this case we investigate a system that is composed by positive an negative charges, similar to an electron-positron systems but the particles are bosons. In this case the potential in Eq.(2.1) becomes

$$V_{ij}(r_{ij}) = \frac{q_i q_j}{r_{ij}}, \tag{3.2}$$

where $q_i = \pm 1$ is the charge of particle i in a.u.

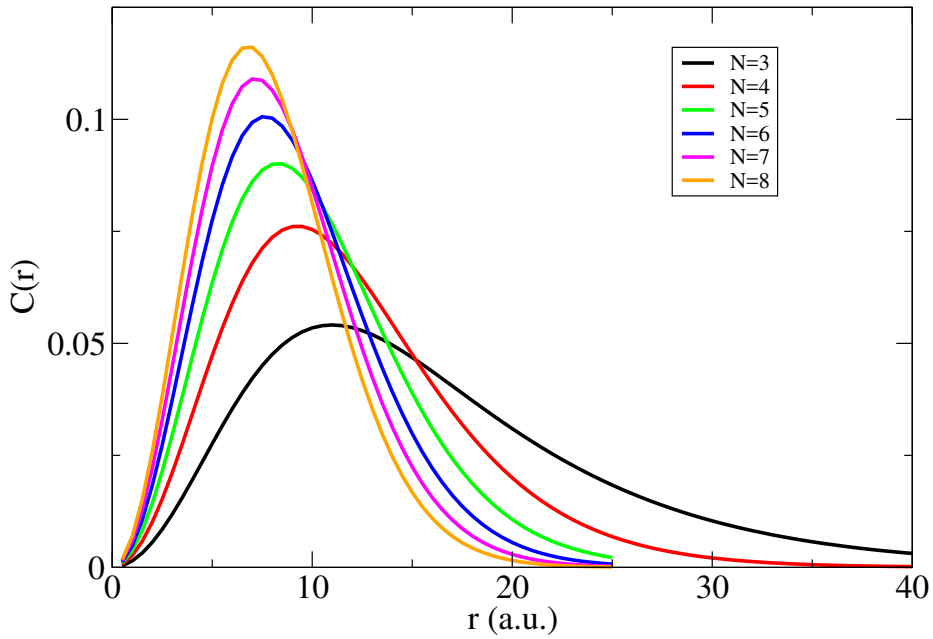

Figure 3.2: Correlation function for N=3-8 bosons interaction via a soft-core Gaussian potential. The peaks of the correlation functions moves toward the origin as the number of particles increases. (Source: Horne, Salas & Varga 2014 [21], ©Springer-Verlag Wien 2014 with permission of Springer.)

The calculations were done for the case where half of the particles are positively and the other half is negatively charged (or there is one extra positive charge if N is odd). A similar arrangement is done for the spin of the particles , with half the particles spin-up and half spin-down, with an extra spin-up when N is odd.

An important issue to discuss is the stability of these systems. Those with electrons and positrons with more than four particles have been shown to be unbound [2] due to their fermionic nature. On the other hand if the particles were bosons then bound states exist [2].

The results are presented in Table 3.2. The calculations up to four particles can be compared to the literature values (see. e.g. Ref. [4]), to show the accuracy of the present approach. For the case of the Coulombic interaction we can observe that that the addition of particles does not produce a large decrease in the size of the system (unlike the soft-core Gaussian). For opposite charges the correlation function is shown in Fig.3.3, where it can be seen that adding particles produces a slight shift of the peaks outwards, while the

N	E	$< r_{++}^{-1} >$	$< r_{+-}^{-1} >$	$< r_{++} >$	$< r_{+-} >$	$< r_{++}^{2} >$	$< r_{+-}^{2} >$
2	-0.250000		0.500		3.000		12.000
3	-0.262005	0.156	0.340	8.549	5.490	93.179	48.419
4	-0.516003	0.221	0.368	6.033	4.487	46.364	29.107
5	-0.556415	0.236	0.322	5.479	4.985	36.630	33.849
6	-0.821942	0.246	0.347	5.167	4.374	32.077	25.007
7	-0.883661	0.219	0.320	5.837	4.725	40.919	28.989
8	-1.161338	0.260	0.340	4.858	4.300	28.059	23.471

Table 3.2: Energies and average powers of inter-particle distances (all in a.u.) of positively and negatively charged bosons interacting with Coulomb potential. The distances between positive charges are denoted as r_{++}, while those between positive and negative ones with r_{+-}. (Source: Horne, Salas & Varga 2014 [21])

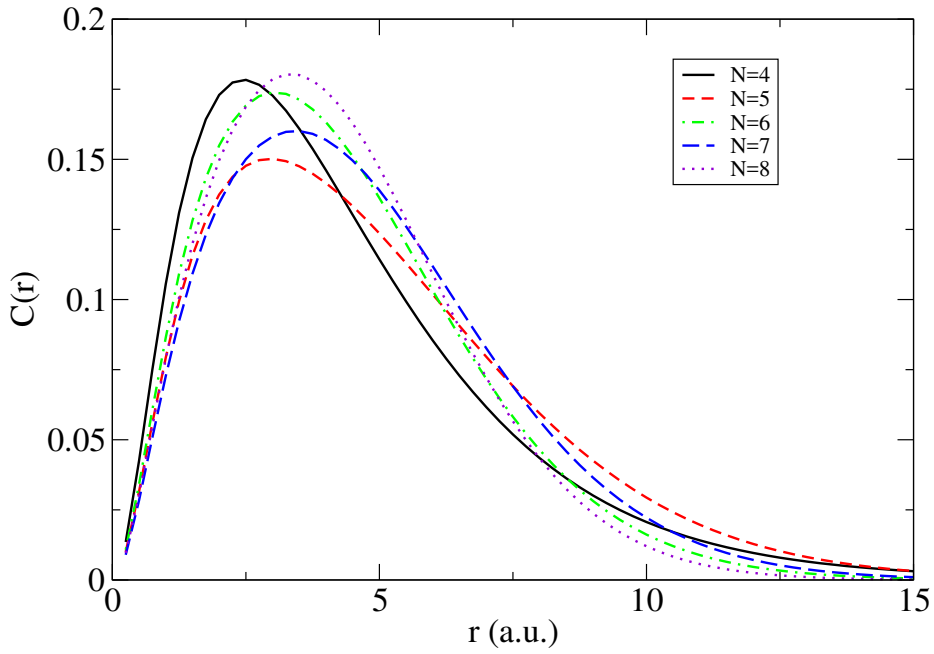

Figure 3.3: Correlation functions between opposite charges for N=4-8 particle two-component Coulomb systems. (Source: Horne, Salas & Varga 2014 [21], ©Springer-Verlag Wien 2014 with permission of Springer.)

amplitude and width of the peaks change slightly. On the other hand, for like-charges the function is shown in Fig. 3.4 and we can see that the system tends to become smaller with increasing N.

3.2.3 Self-gravitating bosons

This case is similar to the previous one but now all bosons are identical and interacting via an attractive gravitational-like potential with unitary strength (in a.u.) given by:

$$V_{ij}(r_{ij}) = -\frac{1}{r_{ij}}. \tag{3.3}$$

The calculated energies are given in Table 3.3. The behavior of the system is similar to the soft-core Gaussian, as expected. There is a rapid increase in binding energy and a reduction of the distances as N increases. The correlation functions (not shown) are very similar to those on Fig. 3.2.

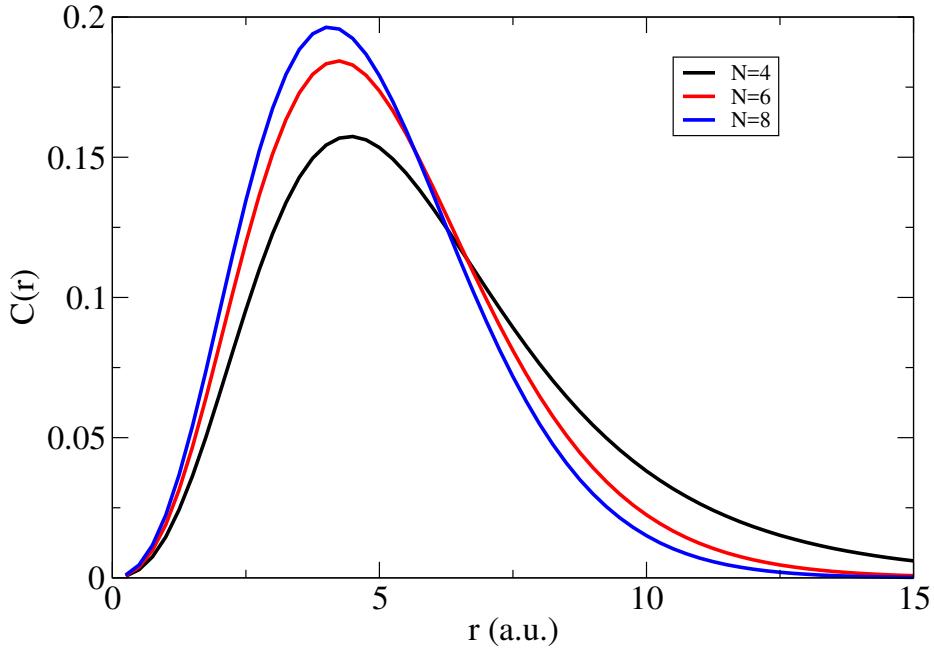

Figure 3.4: Correlation functions between like charges for N=4,6, and 8 particle two-component Coulomb systems. (Source: Horne, Salas & Varga 2014 [21], ©Springer-Verlag Wien 2014 with permission of Springer.)

N	E	$< r^{-1} >$	$< r >$	$< r^2 >$
2	-0.250000	0.500	3.000	12.000
3	-1.071779	0.715	1.994	5.101
4	-2.790733	0.930	1.494	2.814
5	-5.732369	1.146	1.195	1.782
6	-10.22220	1.363	0.996	1.229
7	-16.58536	1.579	0.854	0.899
8	-25.147016	1.796	0.747	0.686

Table 3.3: Energies and average powers of particle-particle distances (all in a.u.) of self-graviting bosons. (Source: Horne, Salas & Varga 2014 [21])

3.2.4 Confined bosons

In the last case we consider an example which is a bosonic counterpart of artificial atoms. In model artificial atoms electrons are confined by an external potential, most often by a harmonic oscillator potential. The competition between the confinement and Coulomb repulsion may lead to the appearance of Wigner crystals, where electrons are localized in crystal like positions [64]. In this example we used bosons instead of electrons, with a repulsive Coulomb interaction

$$V_{ij}(r_{ij}) = \frac{1}{r_{ij}}, \tag{3.4}$$

and a confining potential

$$U_i(r_i) = \frac{1}{2} m\omega^2 r^2, \tag{3.5}$$

where $\omega = 0.5$ and atomic units are used with m=1.

Electrons in harmonic oscillator quantum dots [64], similarly to electrons in atoms, fill up the shells obeying the Hund rule. The major difference between the harmonically confined fermions and bosons is that there is no restriction for shell filling in the bosonic system. In the case of harmonically confined electrons, $l = 1,2$ and higher angular momentum orbitals become important for $N > 2$ electron systems [64] and the total orbital momentum (L) of the ground state is not necessarily zero. In the bosonic case the lowest $l = 0$ orbital can accommodate the particles and the ground state belongs to $L = 0$.

Table 3.4 shows the energies and the properties in this case. The $N = 2$ problem is analytically solvable and the SVM easily recovers the analytical value. The energies for $N > 2$ are significantly lower than in the case of fermions. Direct comparison is not easy, because the fermionic case has different ground state quantum numbers, but for example, the lowest energy of three electrons with identical spins is 4.31 a.u. (this belongs to L=0) [64], while the energy in the bosonic case is 3.70 a.u..

Unlike the previous three cases, where there is no external potential, in this case the

energy and the structure of the system is determined by the interplay of the confining harmonic oscillator potential and the two-body repulsion. The energy levels for the $N = 2, \ldots, 8$ particle systems due to the harmonic oscillator potential alone would be equal to $3/2N\hbar\omega$. The difference between this and the calculated energy is due to the Coulomb repulsion. The inter-particle distances (see Table 3.4) and the correlation functions (see Fig. 3.5) both show that the size of the system increases by adding more particles.

3.3 Conclusions

The energies and other properties of bosonic few-particle systems were calculated using the Stochastic Variational Method with correlated gaussian basis. Four different systems were investigated and the energies were compared to the values found in the literature. The comparison with the results of hyperspherical calculations [37, 50] shows that both the hyperspherical approach and the correlated gaussians can be extended to larger systems. The soft Gaussian potential is relatively easy to calculate and we could get results up to $N = 10$ particles. The hyperspherical approach presented in Ref. [37] are extended up to 112 particles but the results for $N > 10$ case is calculated with a truncated basis and might be less accurate.

We have carefully optimized the basis and checked the convergence of the results, just as we did in previous calculations [4, 64] and the above results are expected to be accurate in all decimals shown. The calculations presented in this paper thus will be hopefully useful in benchmark calculations for bosonic systems.

Calculations for larger systems might be possible, but at present that is very computer time consuming. The major bottleneck is the need of symmetrization which requires the permutation of particles and lead to $N!$ scaling. For systems containing identical particles the permutation might be avoided by employing basis functions that are symmetric with respect to exchange of particles. This would substantially reduce the computational burden and may help in calculations for larger systems.

N	E	$< r_{sp}^{-1} >$	$< r_{sp} >$	$< r_{sp}^{2} >$	$< r_{pp}^{-1} >$	$< r_{pp} >$	$< r_{pp}^{2} >$
2	2.000000	0.721	1.745	3.553	0.447	2.685	8.210
3	3.697493	0.667	1.871	4.064	0.425	2.823	9.075
4	5.804803	0.617	2.002	4.613	0.398	3.009	10.285
5	8.297644	0.580	2.114	5.114	0.381	3.142	11.209
6	11.183827	0.553	2.218	5.643	0.369	3.256	12.076
7	14.419759	0.530	2.308	6.096	0.360	3.356	12.850
8	18.046455	0.505	2.420	6.696	0.349	3.474	13.788

Table 3.4: Energies, average powers of single particle distances (r_{sp}) and particle-particle distances (r_{pp}), all in a.u., for the case of confined bosons. (Source: Horne, Salas & Varga 2014 [21])

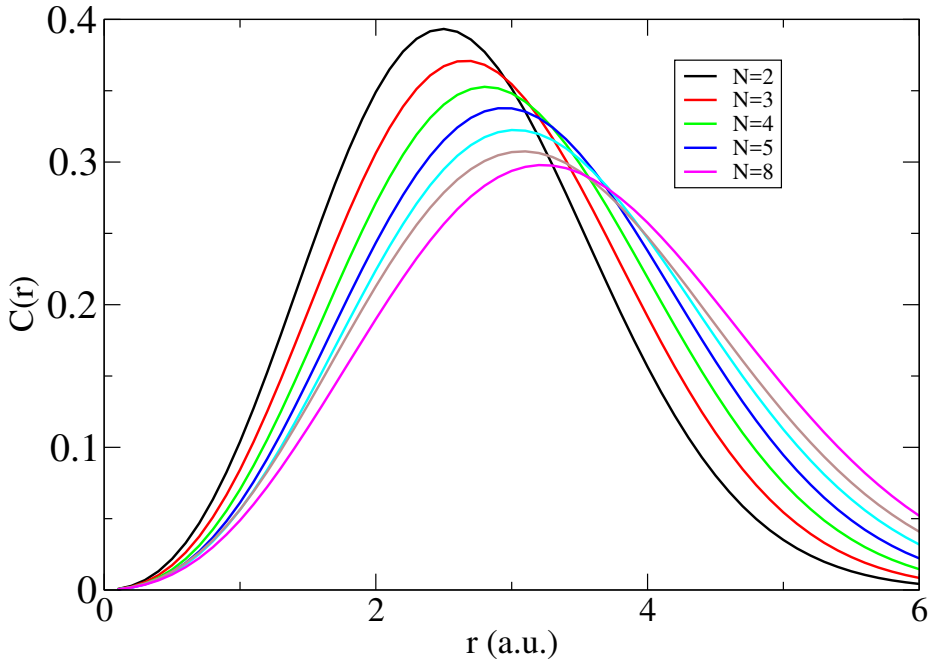

Figure 3.5: Correlation function for N=2-8 bosons interaction via a repulsive Coulomb interactions and confined with a harmonic oscillator potential. The peaks of the correlation functions moves outward from as the number of particles increases. (Source: Horne, Salas & Varga 2014 [21], ©Springer-Verlag Wien 2014 with permission of Springer.)

CHAPTER 4

INTERACTIONS WITH STRONG MAGNETIC FIELDS

The present chapter focuses on using the Stochastic Variational Method for studying the stability and structure of three-electron systems in the presence of strong magnetic fields, with a big focus on the formation of negative Helium ions. The chapter is organized as follows: An introduction to strong magnetic fields and their effects is given in 4.1. Then the computational methods are described in 4.2, and the Hamiltonian and the employed approximations explained in 4.3. The calculated energies and properties of the studied systems are then given in 4.4. The formation of He^- is discussed in 4.4, and the possibility of having stable H^{2-} is studied in 4.6. We then study the diamagnetic properties of the systems in 4.7. Finally the limitations of the study are discussed in 4.8. The works described in the present chapter were published in Refs.[65, 66], and reproduced with permission from the publishers.

4.1 Atoms in strong magnetic fields

It is well known that the presence of external magnetic fields can alter the properties of atoms. A weak external field gives rise to the Zeeman effect if the splitting of the levels is small. If the field gets strong enough, then the spin-orbit coupling breaks, producing a different splitting pattern [5], known as the Paschen-Back effect.

If the magnetic field gets even more intense, the Landau quantization becomes significant and the changes in energy levels are no longer small. Under strong magnetic fields the properties of matter can change drastically, far beyond those described by the Paschen-Back effect [67–71]. One of the most important effects is that states with adjacent energies in the field-free case can crossover depending on the field strength, implying that a ground state at a certain field intensity may become an excited state in another one and vice-versa.

These changes in the energy levels imply variations in the transition frequencies and deformation of the orbitals. These changes alter the stability of the systems, and have been predicted to induce the formation of negative ions such as He^- [72–76].

The application of a very strong uniform field produces an effective confinement of the electrons along the perpendicular plane due to the Lorentz force [77]. As the electrons are kept closer, the electric force due to the nucleus becomes stronger. At the same time the electron repulsion is also enhanced, so there is a competition between forces. Aligning spins with the external magnetic field gives a lower energy, but achieving this configuration requires placing the electrons in different orbitals. In field-free systems having higher angular momenta in general implies a higher energy, but when a field is present then the alignment of the orbital magnetic moments could instead reduce it. The magnetic field can reshape the orbitals, breaking the spherical symmetry, inducing a quadrupole moment on the atom [77–79]. The presence of a confining force on the perpendicular plane implies that the stability of the system is solely determined by the interactions along the field direction due to polarization effects. If the resulting effective 1D potential along that direction is negative then the system is guaranteed to have at least one bound state [79].

The study of the effects of strong magnetic fields on energy levels and wave functions is strongly motivated by the discovery of stars with very strong magnetic fields [80–82]. These magnetic field strengths range from the weaker fields of white dwarfs [83, 84] ($\approx 10^7$ G) through neutron stars [85] ($\approx 10^{12}$ G) all the way up to fields of 10^{14}-10^{15} G observed in magnetars [86]. On the other hand, in general the magnetic fields in the universe tend to be weak, of the order of μG [87], while in laboratory conditions the highest achievable magnetic field is around 10^5 G [88, 89].

Accurate calculations of wavelengths, dipole moments and oscillator strengths for atoms and molecules are needed to explain the observed spectra in the strong magnetic fields of these stars. Recent studies have focused on the role of the strong magnetic field in the formation of the crust of neutron stars [90]. Also, measuring magnetic fields can allow the

exploration of stellar dynamo processes, and a model for employing molecules as magnetic probes has been tested with data from realistic scenarios [91].

The effect of magnetic field on the energy levels of molecules has also been extensively studied [92–101]. High magnetic fields drastically change the binding energies, bond lengths [101], and can lead to new bonding mechanisms like *paramagnetic bonding* [95]. Calculations for molecules are very difficult, because the separation of center of mass motion [102] is not trivial and the description of nuclear and electronic structure is complicated. Recent works [92, 93, 96] using current density functional theory [103] established a non-perturbative framework to calculate the molecular properties in magnetic fields.

Another area of interest for the study of strong magnetic fields is condensed matter physics, for which similar few-body problems exist. These can be found in systems of electrons and holes in quantum dots, where the small effective masses and the large dielectric constant lead to large effective magnetic fields [64, 104–108]. This has been recently observed experimentally for Si:Se [108].

4.2 Computing solutions of few-electron systems

The computation of few-body systems in strong magnetic fields is complicated. First of all, the magnetic field breaks the symmetry of the system and this symmetry breaking has to be taken into account in constructing the wave function. Secondly, the magnetic field confines the system in the plane perpendicular to the direction of the field leading to elongated structures. In these structures the competition between the Coulomb interaction and the magnetic field determines the energy levels of the system and the correlation between the particles. At very strong fields the magnetic field dominates, e.g. the spins are aligned anti-parallel to the direction of the field and the spin flip energy is much larger than the single particle energy, at weak fields the Coulomb interaction has more pronounced effect, but there is no perturbative regime where one or the other can be neglected.

Many different computational approaches [67–71, 77, 109–111] have been used to

study the effects of strong magnetic fields on small atoms and ions, such as H, H^-, He, Li, Be. The most popular approaches include the Hartree-Fock method [78, 112–121], variational calculations with Gaussian [12, 13], Hylleraas [122, 123], or Lagrange basis functions [124], Quantum Monte Carlo (QMC) [125, 126], finite element calculations [127], or pseudospectral Hartree-Fock[128]. Most of these approaches treat all electrons explicitly, but some introduce approximations restricting the core electron degrees of freedom to reduce the computational burden [129].

Analytical calculations have also been proven to be valuable tools. It has been analytically predicted, for example, that under very strong magnetic fields neutral atoms can bind with an additional electron [76, 130]. In particular, it was claimed that Helium, despite being a noble gas, was capable of forming a stable negative ion under such conditions [72–76]. Recent works based on computational methods have verified this prediction of the He^- ion [65, 123].

The simplest system, the one-electron problem, has been intensively studied using B-splines [131], finite elements [132], power series [133] and Lagrange mesh [134] methods, and the the properties of the hydrogen atom in magnetic field is accurately known. The two electron systems, including the He atom [112–115, 124, 135–137] and the H^- ion [79, 138–145], have been also focus of numerous studies and serve as a benchmark test for quantum mechanical calculations.

The number of calculations for three-electron systems is much less. Ivanov and Schmelcher studied the Li atom in magnetic field using the Hartree-Fock method [146]. Variations of approaches restricting the core electrons [129, 147] have also been used to solve this problem. The most accurate energies of this system are calculated by the Hylleraas approach [122].

Approaches based on explicitly correlated wave functions [65, 122, 124] are likely to be restricted to smaller atoms, with the only exception being the QMC method [125, 126, 148]. For larger systems the QMC method [125, 126], the Hartree-Fock [78, 112–121, 128]

and the density functional theory (DFT) approach [149, 150] seem to be applicable. The DFT approaches are particularly important because they can help the development of better exchange correlational functionals. A recent thorough review of different approaches can by found in Ref. [151].

We first explain the Hamiltonian and the approximations used in section 4.3. We then show the calculated energies and properties for He^-, Li and Be^+ in section 4.4. More details on He^- are shown in Refs. [65, 66].

4.3 The Hamiltonian for strong magnetic fields

The Hamiltonian of a Coulombic N-particle system in magnetic field is defined as

$$H = \sum_{i=1}^{N}\left(-\frac{1}{2}\Delta_i + \frac{B^2}{8}(x_i^2+y_i^2) - \frac{Z}{r_i}\right) + \sum_{i<j}^{N}\frac{1}{r_{ij}} + \frac{B}{2}(L_z+2S_z) \quad (4.1)$$

$$= T + V_{dia} + V_{Ne} + V_{ee} + \frac{B}{2}(L_z+2S_z) \quad (4.2)$$

where L_z (S_z) is the z component of the orbital momentum (spin) of the system, the magnetic field of strength B is directed along the z axis and Z is the charge of the nucleus. In the second part of the equation we separated the terms of the Hamiltonian into kinetic energy (T), the diamagnetic term given by a two dimensional harmonic oscillator-like contribution of the magnetic field (V_{dia}) plus the Coulomb interaction between the electrons (V_{ee}) and between the nucleus and the electrons (V_{Ne}). The positions of the particles are denoted by $\mathbf{r}_i = (x_i, y_i, z_i)$, and the relative distances are defined by $\mathbf{r}_{ij} = \mathbf{r}_i - \mathbf{r}_j$. Atomic units are used, and the magnetic field in these units is equal to 2.35×10^9 G.

All this is done within the non-relativistic framework, neglecting any QED effects and center of mass motion due to an infinitely heavy nucleus, as it is commonly done in the literature. Additionally the external magnetic field is assumed to be uniform and constant in time. Any internal magnetic fields of the atom are neglected. The motion of the center of mass is neglected as well as any thermal effects.

Quantum Numbers		Electronic configuration	$\nu^{2S+1}(M)^{\pi}$
$M=0$	$S_z=-\frac{1}{2}$	$1s^2 2s$	$^2(0)^+$
$M=-1$	$S_z=-\frac{1}{2}$	$1s^2 2p_{-1}$	$^2(-1)^+$
$M=-1$	$S_z=-\frac{3}{2}$	$1s2s2p_{-1}$	$^4(-1)^+$
$M=-3$	$S_z=-\frac{3}{2}$	$1s2p_{-1}3d_{-2}$	$^4(-3)^+$

Table 4.1: Spin and angular momentum configurations for three-particle systems considered in the present work. ν is the degree of excitation and π is the parity of the state in the z direction. For all cases only the lowest degree of excitation with positive parity was considered. (Source: Salas et. al. 2015 [66])

4.3.1 States of interest and quantum numbers

For atoms in strong magnetic fields the spherical symmetry is broken, so the eigenstates of the system can no longer be identified by the usual quantum numbers. Instead each state is labeled depending on: total magnetic quantum number M, total spin quantum number S_z, parity in z (π) , and degree of excitation ν.

There are three ways the states are denoted in the literature: by their quantum numbers M and S_z, by their electronic configuration for weak/zero field, or the form $\nu^{2S+1}(M)^{\pi}$. Table 4.1 shows the equivalence between the different notations for the states of three-electron systems studied in the present work.

These states in general have different energies because of broken degeneracies. However they exhibit crossovers, such that and their ordering in energy varies depending on field strength. The points where the energy levels of two different states are equal are called *transition points* in the literature [78, 152], and we employ the same terminology (not to be confused with phase transitions or electronic transitions corresponding to emission or absorption lines).

4.3.2 Ionization Threshold and observables

To investigate the stability, we will compare the one-particle ionization threshold energy $E_T(M,S_z)$ (the energy needed to move one electron to infinity) to the energy of the three-particle system. The system is stable if the total energy is lower than the threshold energy. For example, the He^- ion it is defined as:

$$E_T(M,S_z) = \min_{M^{He},S_z^{He}} \left(E^{He}(M^{He},S_z^{He}) + E^e(M^e,S_z^e)\right), \tag{4.3}$$

where $E^{He}(M^{He},S_z^{He})$ is the total energy of the He atom, and

$$E^e(M^e,S_z^e) = \left(M^e + |M^e| + 2S_z^e + 1\right)\frac{B}{2} \tag{4.4}$$

is the energy of the Landau levels of the electron. The quantum numbers satisfy

$$M = M^{He} + M^e \qquad S_z = S_z^{He} + S_z^e. \tag{4.5}$$

We consider only those states that satisfy conservation of orbital angular momentum and spin, as given in Eq.(4.5), and calculate the threshold energy using Eq.(4.3). Once the threshold is found the binding energy can be obtained from:

$$E_{ion} = E_{tot} - E_T. \tag{4.6}$$

The procedure is analogous for H^{--}/H^-, Li/Li^+, and Be^+/Be^{++}.

Distances can also be used as a guideline to determine if a state is bound or unbound. Separations between particles in a bound system are small, and the particles are typically confined into distances of a few atomic units. Loosely bound systems tend to be larger, but still finite. In unbound systems the distances diverge. The distances can be calculated as described in section 2.5.1.

Another quantity of interest is the quadrupole moment which is defined the same way as in Ref. [78]:

$$Q_{zz} = \langle \Psi | \sum_{i=1}^{N} 2z_i^2 - \rho_i^2 | \Psi \rangle = N(2z_{Ne}^2 - \rho_{Ne}). \tag{4.7}$$

The diamagnetic term of the Hamiltonian is:

$$V_{dia} = \sum_{i=1}^{N} \frac{B^2}{8} \left(x_i^2 + y_i^2 \right), \tag{4.8}$$

while the paramagnetic term is then given by:

$$V_{par} = \frac{B}{2} \left(L_z + 2S_z \right). \tag{4.9}$$

We also define V_{mag} as the total contribution of the energy due to the magnetic field as the sum of the total paramagnetic and diamagnetic contributions to the energy:

$$\begin{aligned} V_{mag} &= V_{dia} + V_{par} & (4.10) \\ &= \sum_{i=1}^{N} \frac{B^2}{8} \left(x_i^2 + y_i^2 \right) + \frac{B}{2} \left(L_z + 2S_z \right). & (4.11) \end{aligned}$$

4.4 Energies and properties of three-electron systems

We have calculated the energies of the three-electron isoelectronic series with nuclear charge Z=1-4 for multiple values of strong magnetic fields for bound states with different angular momentum and spin configurations. N=400 basis functions are used unless otherwise noted.

To test the accuracy of our results we compare our calculation for the energies of low lying states of the Li atom to Ref. [116], the most accurate results found in the literature. The calculations presented in Ref. [116] are based on Hylleraas-type basis functions and

are expected to be very accurate for weak magnetic fields. For higher fields, the Hylleraas description needs many high orbital momentum states and becomes computationally very expensive.

Table 4.2 shows the present results and the energies predicted by the Hylleraas approach. For low fields the two calculations are in complete agreement. In the free field case it is very hard to compete with the accuracy of the Hylleraas approach. One has to use N=2000 basis functions to reach accuracy up to 6 decimal places. For higher fields the Hylleraas basis seems to be less accurate and our results improve the previous energies at the third decimal. There is one case, the $^2(-2)^+$ state with B=0.009, where our energy is significantly different from that of Ref. [122]. As other energies in this magnetic field region agree perfectly, we suspect that there might be a typo in Ref. [122].

Using our approach we have studied the low lying positive parity states shown in Table 4.1. These states can be either ground states or lowest excited states depending on the strength of the magnetic field. The evolution of the ground state as a function of the strength of the magnetic field as predicted by our calculations is shown in Fig. 4.1. For Li and Be^+ the ground state is the $^2(0)^+$ configuration for low, $^2(-1)^+$ for intermediate and $^4(-3)^+$ for very high fields. The ground state of He^- is the $^2(-1)^+$ configuration for smaller values of B [65, 123] rather than the $^2(0)^+$ configuration which is not bound. However for higher values the ground state of He^- follows the same pattern as that of Li and Be^+.

The ground state transition points for three-electron systems have been studied in several papers [78, 120, 125, 126]. The calculation of the precise location of the ground to excited states transition points requires very high accuracy for both states, and that is computationally expensive. For the case of Li, the transition has been predicted at $B = 2.153$ a.u. [78] and $B = 2.19816$ a.u. [125]. In the case of Be^+, the crossover was estimated to take place at around $B = 4.501$ a.u. in Ref. [118] and $B = 4.55328$ a.u. [125]. Our calculation is in good agreement with these predictions (see Fig. 4.1).

	$^2(0)^+$		$^2(-1)^+$		$^2(-2)^+$	
B	Energy	Ref[122]	Energy	Ref[122]	Energy	Ref[122]
0	-7.478 060 320	-7.478 060 323	-7.410 156 508	-7.410 156 524	-7.335 523 535	-7.335 523 537
0.001	-7.478 558 8	-7.478 558 8(1)	-7.411 153 7	-7.411 153 9(2)	-7.336 509 7	-7.336 500 7(2)
0.0018	-7.478 955 4	-7.478 955 5(2)	-7.411 947 5	-7.411 9475(1)	-7.338 189 4	-7.338 189 4(1)
0.009	-7.482 436 5	-7.482 436 7(2)	-7.418 932 0	-7.418 9321(2)	-7.347 954 1	-7.348 185 6(1)
0.01	-7.482 907 5	-7.482 907 6(1)	-7.419 879 5	-7.419 879 5(1)	-7.349 208 9	-7.348 823 7(1)
0.018	-7.486 566 1	-7.486 566 8(3)	-7.427 265 4	-7.427 2656(2)	-7.349 501 5	-7.358 501 7(1)
0.02	-7.487 450 5	-7.487 451 9(2)	-7.429 059 0	-7.429 059 0(1)	-7.360 614 0	-7.360 448 1(2)
0.2	-7.529 806 2	-7.529 807 (1)	-7.538 656 3	-7.538 654 8(4)	-7.458 826 2	-7.458 823 8(1)
0.4	-7.531 275 5	-7.531 188 7(2)	-7.610 167 0	-7.610 130 7(2)	-7.510 686 6	-7.510 607 6(2)
0.5	-7.523 946 2	-7.523 918 (6)	-7.637 0223 7	-7.636 927 4(3)	-7.528 106 1	-7.528 018 7(1)
0.54	-7.520 090 0	-7.520 016 (1)	-7.646 547 4	-7.646 491 6(1)	-7.533 948 3	-7.533 850 (1)
0.6	-7.513 531 7	-7.513 400 (2)	-7.659 690 7	-7.659 533 (3)	-7.541 677 5	-7.541 506 (3)
0.7	-7.501 000 4	-7.500 958 (7)	-7.678 861 1	-7.678 598 (3)	-7.552 080 7	-7.551 717 (2)
0.9	-7.471 717 4	-7.471 460 (2)	-7.708 359 3	-7.707 760 (1)	-7.564 823 8	
1	-7.455 437 7	-7.454 284 (1)	-7.719 225 9	-7.718 357 (4)	-7.567 629 82	-7.566 400 (1)

Table 4.2: The energies for Li in various configurations calculated in the present work and compared to the values in Ref[122]. The standard uncertainty is shown in parentheses where applicable. Our calculations are converged up to the six decimal places. (Source: Salas et. al. 2015 [66])

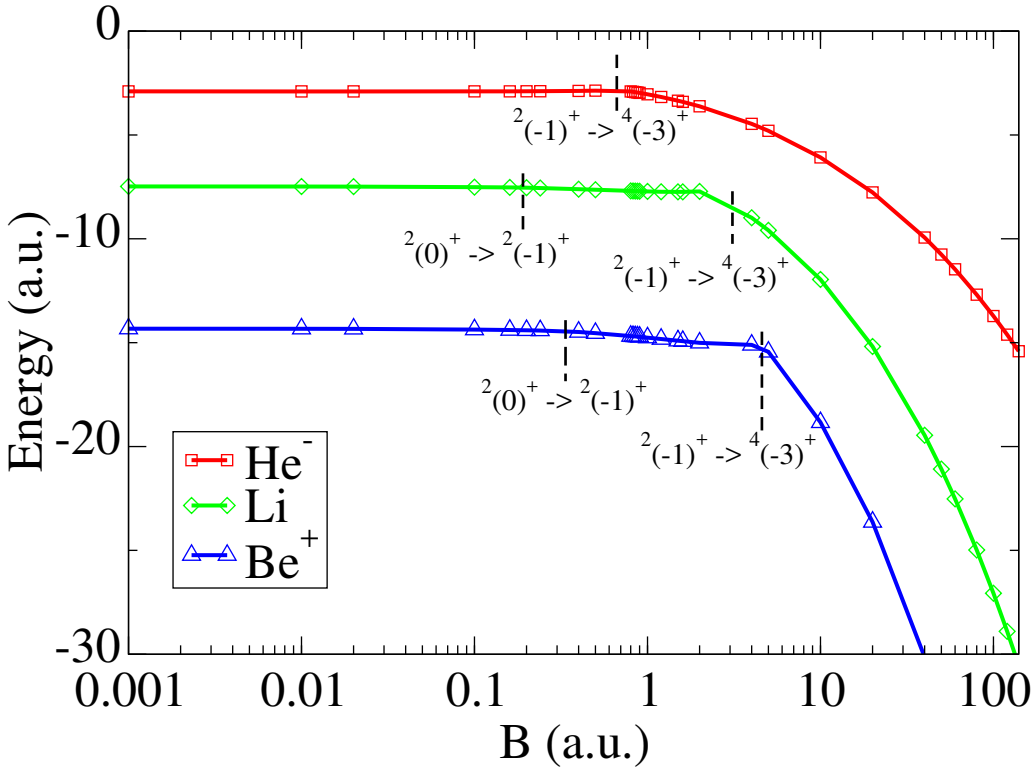

Figure 4.1: Ground states energies for different values of magnetic field in He^- (red), Li (green), Be^+ (blue). The regions where the ground state of the system makes a transition are marked with the vertical lines, and indicating the corresponding configurations. (Source: Salas et. al. [66]. ©2015 American Physical Society)

4.4.1 The $^2(0)^+$ ($M = 0, S_z = -\frac{1}{2}$) configuration

For $Z \leq 4$ only the Li atom and the Be^+ ion are bound. No bound states for He^- were found for this configuration. The threshold energy is defined by the energy of the Li^+ and Be^{++} ions with $M = 0, S_z = 0$ for all values of the magnetic field. The calculated energies for Li and Be^+ as a function of the magnetic field are shown in Fig. 4.2, and in Ref. [66].

The total energy of Li in this configuration has a local minimum, as previously reported in Ref.[78] at $B = 0.304$ a.u. A similar minimum for Be^+ is around $B = 0.8$ a.u., and general behavior of the two curves is rather similar. The binding energies of these states are shown in Fig. 4.2. The binding energies first start to increase with the magnetic field, but at a certain maximum point this trend changes leading to a local minima after which the binding increases again. The minimum values for binding energy are located around $B = 2$ a.u. for Li and $B = 4$ a.u. for Be^+. The shape of the binding energy curve is determined by the difference between the total energy of the three-electron and the total energy of the two-electron system, therefore these curves have more complicated structure than the three-electron energy curve (see Fig. 4.2). The maximum values of binding energies were found around $B = 0.4$ a.u. for Li and $B = 1.2$ a.u. for Be^+. It is important to point out that the systems undergo significant structural changes near those regions. In the interval 0.24 a.u. $< B <$ 0.4 a.u. Li becomes more elongated along the z direction and then changes back to being a less prolate shape as seen in Fig. 4.2. For the case of Be^+ a similar expansion is observed in the same figure for Z_{Ne}^2 but around the interval 0.8 a.u. $< B <$ 4 a.u.

4.4.2 The $^2(-1)^+$ ($M = -1, S_z = -\frac{1}{2}$) configuration

The total energies for He^-, Li and Be^+ are plotted in Fig. 4.3. The corresponding binding energies (see Fig. 4.3) are calculated by using the threshold energy belonging to the $^1(0)^+$ state of He atom and Li^+ and Be^{++} ions for all magnetic fields. The $^2(-1)^+$ state was found to be bound for Li and Be^+ for all values of B, and but the He^- ion is only

bound for certain B field intensities.

The $^2(-1)^+$ configuration has a local minimum in total energy for Li and Be^+ (Fig. 4.3). However, there is no minimum observed for He^-; it's total energy is monotonously increasing. This shows that the minimum in the energy curves of Li and Be^+ is due to the competition between the attractive nuclear Coulomb potential and the magnetic interaction. In the Li atom and the Be^+ ion the magnetic field forces the electron closer to the nucleus and that decreases the energy up to a certain B value. In the He^- ion the Z=2 charge is not strong enough to produce the same effect.

The He^- in this configuration is not bound without a magnetic field, and according to the present calculation a minimal field strength $B = 0.062(6)$ a.u. is needed for bound He^- ion. This is a slight improvement over the previous works [65, 123]. Determining a more accurate value is possible but computationally expensive.

The quadrupole moments of the systems in the $^2(-1)^+$ configuration are compared in Fig. 4.3 and in Ref[66]. The weakly bound He^- ion has a prolate shape and becomes gradually more spherical as the magnetic field increases. The Li and Be^+ have oblate shapes at low magnetic fields and change to prolate shapes after the magnetic field becomes strong enough.

4.4.3 The $^4(-3)^+$ ($M = -3$, $S_z = -\frac{3}{2}$) configuration

The energies for this configuration are shown in Fig. 4.5. This state is fully spin polarized and eventually becomes the ground state at higher B fields for He^-, Li and Be^+, as shown in Fig. 4.1.

The threshold for this state is similar to that of the $^4(-1)^+$ configuration, corresponding to configurations $^2(0)^+$ and $^2(-1)^+$ of the two-electron systems, as explained before. The He^- $^4(-3)^+$ is not stable below $B = 0.02$ a.u., but for stronger fields it does becomes stable and it is the ground state at higher fields.

In Ref.[66] there is greater details on the energy contributions for Li and He^-. Note that

$\langle V_{Ne} \rangle$ is always more negative for the ${}^2(-1)^+$ configuration than for the ${}^4(-3)^+$ case (see [66]). On the other hand $\langle V_{mag} \rangle$ is always more negative for the ${}^4(-3)^+$ case since its fully spin polarized. The electron repulsion tends to be less significant for ${}^4(-3)^+$ than ${}^2(-1)^+$, for all three-electron systems. This shows that having a higher angular momentum allows a reduction of the electron repulsion, while simultaneously decreasing the Coulombic attraction due to the larger distances. For large magnetic fields having larger angular momenta is energetically favored since it allows for the alignment of the magnetic moments with the external field, giving a more negative $\langle V_{mag} \rangle$. This eventually leads to crossover and the ${}^4(-3)^+$ state becomes the ground state. Due to the difference in nuclear charge the contribution of $\langle V_{Ne} \rangle$ is much larger for Li than for He^-, which also induces larger kinetic energy for Li. At the same time the magnetic contribution is comparable in the two systems, and the strong magnetic contribution supports the bound state of the He^- ion.

4.5 The He^- ion

We previously showed some of the properties of the He^- ion in section 4.4 in comparison with other systems. In this section we focus on He^- in more detail.

4.5.1 The $M = 0$, $S_z = -1/2$ state

The $M = 0$, $S_z = -1/2$ state of He^- is not bound. Note that in this case the energy of the He^- should converge to the energy of the $M = 0$, $S_z = 0$ state of He. Table 4.3 shows that our calculation indeed converges to that threshold. The convergence could be further improved by increasing the range of the Gaussians, allowing a better approximation of the wave function as a bound He and an electron in the continuum. The results of Ref.[153] are only close to the threshold in the case of weak fields and very far off in stronger field cases.

The $M = 0$, $S_z = -1/2$ state of He^- is analogous of the $M = 0$, $S_z = -1/2$ state of Li, but the latter is strongly bound (the ionization energy is about 0.2 a.u. at B=0 and

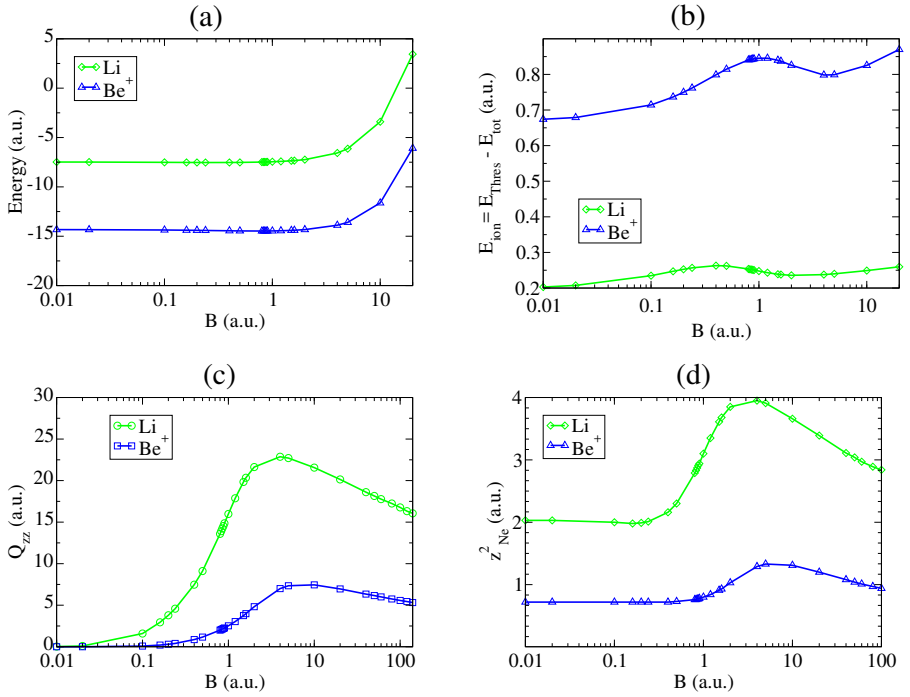

Figure 4.2: State with $^2(0)^+$ ($M = 0, S_z = -\frac{1}{2}$): (a) Total energies. (b) binding energies. (c) Q_{zz} (d) Average z^2_{Ne} for Li and Be^+. (Source: Salas et. al. [66] ©2015 American Physical Society)

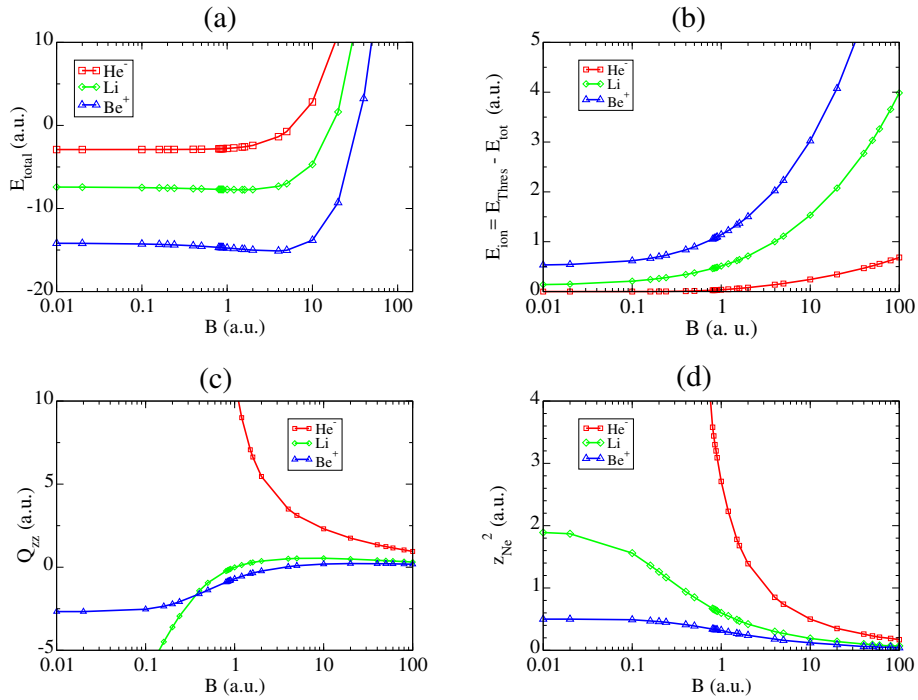

Figure 4.3: State with $^2(-1)^+$ ($M = -1, S_z = -\frac{1}{2}$): (a) Total energies, (b) binding energy, (c) Q_{zz}. (d) Average z^2_{Ne}. (Source: Salas et. al. [66] ©2015 American Physical Society)

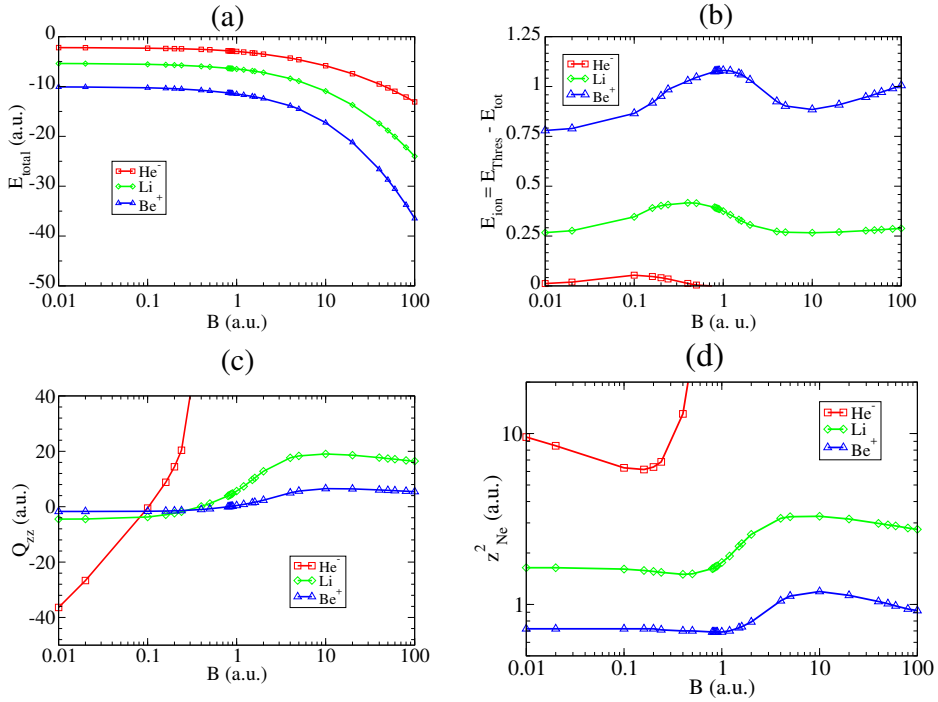

Figure 4.4: State with ${}^4(-1)^+$ ($M = -1$, $S_z = -\frac{3}{2}$) for different nuclear charge Z: (a) Total energies, (b) binding energies, (c)Q_{zz}, (d) average distance z^2_{Ne} for different values of magnetic field. (Source: Salas et. al. [66] ©2015 American Physical Society)

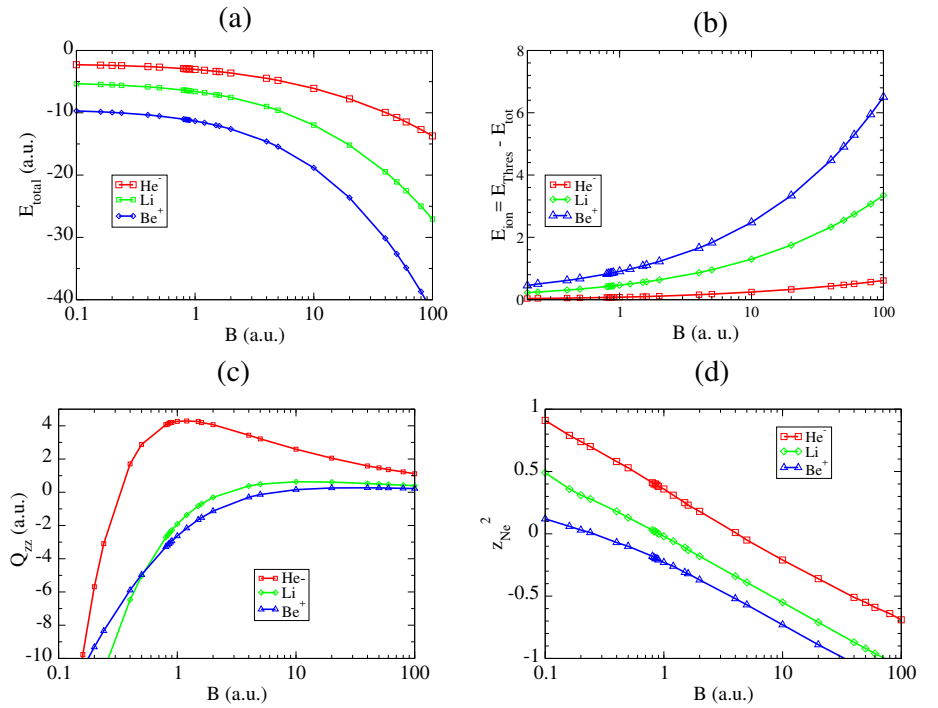

Figure 4.5: State with ${}^4(-3)^+$ ($M = -3$, $S_z = -\frac{3}{2}$): (a) Total energies, (b) binding energy, (c) Q_{zz}, (d) average z^2_{Ne}. (Source: Salas et. al. [66] ©2015 American Physical Society)

B	Total energy		Threshold
	Present work	Ref. [153]	E_T=$E^{He}(M^{He}=0, S_z^{He}=0)$
0.00	−2.90292		−2.90372 [137]
0.10	−2.90108	−2.871	−2.90174 [124]
0.16	−2.89792	−2.861	−2.89829 [135]
0.24	−2.89169	−2.848	−2.89240 [124]
0.40	−2.87230	−2.816	−2.87287 [124]
0.50	−2.85566	−2.794	−2.85624 [137]
0.80	−2.78782	−2.713	−2.78843 [124]
1.00	−2.72976	−2.652	−2.73037 [124]
1.60	−2.50821		−2.50881 [124]

Table 4.3: Energies (in a. u.) of M=0, S_z=−1/2 He^- in magnetic field are shown, as well as their respective threshold energies.

it increases with the magnetic field). The square of electron-electron ρ_{ee}^2 (z_{ee}^2) and the electron-nucleus ρ_{Ne}^2 (z_{Ne}^2) distances in the radial (perpendicular) direction are also shown in Table 4.4. The harmonic oscillator part of the Hamiltonian confines the particles in the radial direction, so the ρ_{ee}^2 and ρ_{Ne}^2 distances are finite and decreasing with increasing magnetic field. In the perpendicular direction, z_{ee}^2 and z_{Ne}^2 converge to infinity showing that an electron is detached from the He atom. By increasing the range of the Gaussians (γ_{max}) in the basis functions these distances increase. The results presented in Tables 4.3 and 4.4 are calculated with $\gamma_{max} = 100$.

4.5.2 The $M = -1$, $S_z = -1/2$ state

Our calculation confirms that this state is indeed bound. The ionization threshold for this case is given by $E^{He}(M^{He}=0, S_z^{He}=0)$. The energy of the $M = -1$, $S_z = -1/2$ state of He^- is shown in Fig. 4.6. According to our calculation, this state is stable in a magnetic field starting at around $B = 0.01$ and remains stable with increasing magnetic field. The calculation of the precise boundary of the stability region is computationally expensive (many basis functions are required to represent the very weakly bound system). This state

B	ρ_{ee}^2	z_{ee}^2	ρ_{Ne}^2	z_{Ne}^2
0.00	875.85	243.06	437.89	121.52
0.10	14.44	957.20	7.20	478.58
0.16	9.42	897.28	4.70	448.61
0.24	6.62	994.59	3.29	497.27
0.40	4.36	1255.59	2.17	627.77
0.50	3.67	1203.83	1.82	601.89
0.80	2.58	1191.26	1.28	595.61
1.00	2.19	1261.02	1.08	630.49
1.60	1.55	1260.54	0.77	630.26

Table 4.4: Averaged distances (in a. u.) of M=0, S_z=$-$1/2 He^- in magnetic field. The square of electron-electron distances in the radial and perpendicular direction, ρ_{ee}^2 and z_{ee}^2, as well as the square of the electron-nucleus distances, ρ_{Ne}^2 and z_{Ne}^2, are shown. (Source: Salas & Varga 2014 [65])

becomes the ground state for the He^- ion for weaker fields.

4.5.3 The $M = -3$, $S_z = -3/2$ state

The $M = -3$, $S_z = -3/2$ state, corresponding to the loosely bound state of Li, with the same quantum numbers, is also bound (Fig. 4.8). The relevant threshold is associated with the $(M^{He} = 0, S_z^{He} = -1)$ state of He at B$<$ 0.1. At B=0.1 a.u. and above the threshold is determined by $E^{He}(M^{He} = -1, S_z^{He} = -1)$ (see Eq. (4.3)). This He^- state is much less bound than the analogous Li state (at B=0.1 a.u the binding energy of He^- is 0.02 a.u, that of Li is 0.14 a.u) but as the energy and the particle-particle distances show the system is bound. The system becomes bound at small magnetic fields at about B=0.02 a.u and remains stable with increasing magnetic field.

At the transition points the total energies of the two configurations become equal. However, the structure of the two states can be very different. This is illustrated for He^- in Fig. 4.9.

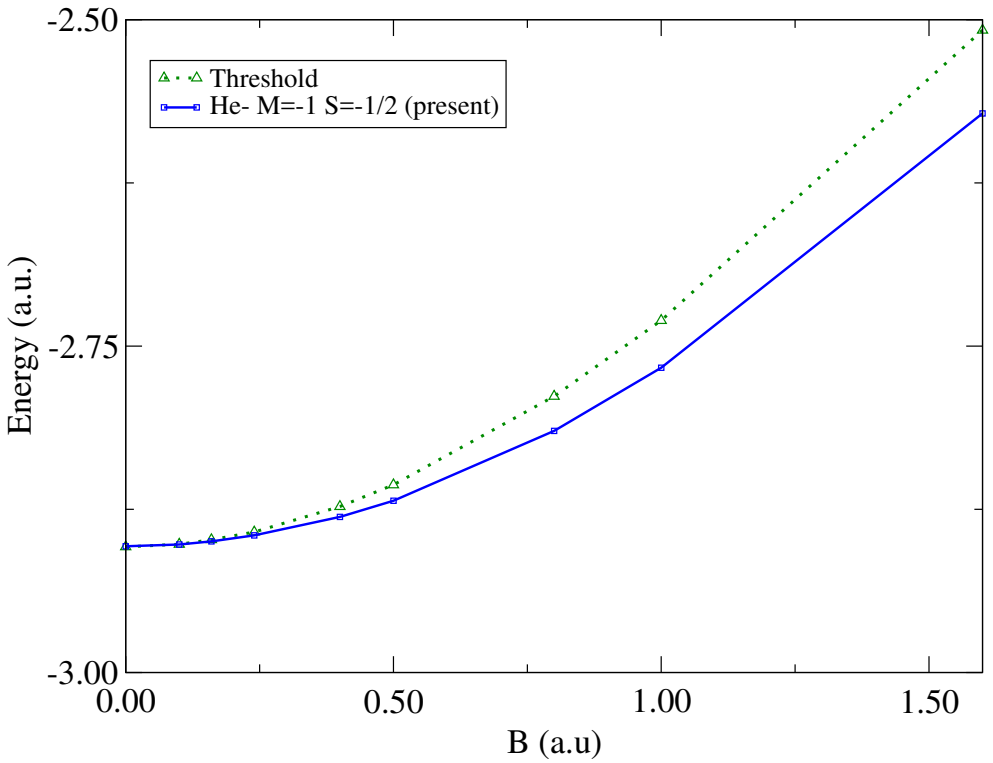

Figure 4.6: Energies and thresholds of the $M = -1$, $S_z = -1/2$ state of He^- for different magnetic field intensities. (Source: Salas & Varga [65]©2014 American Physical Society)

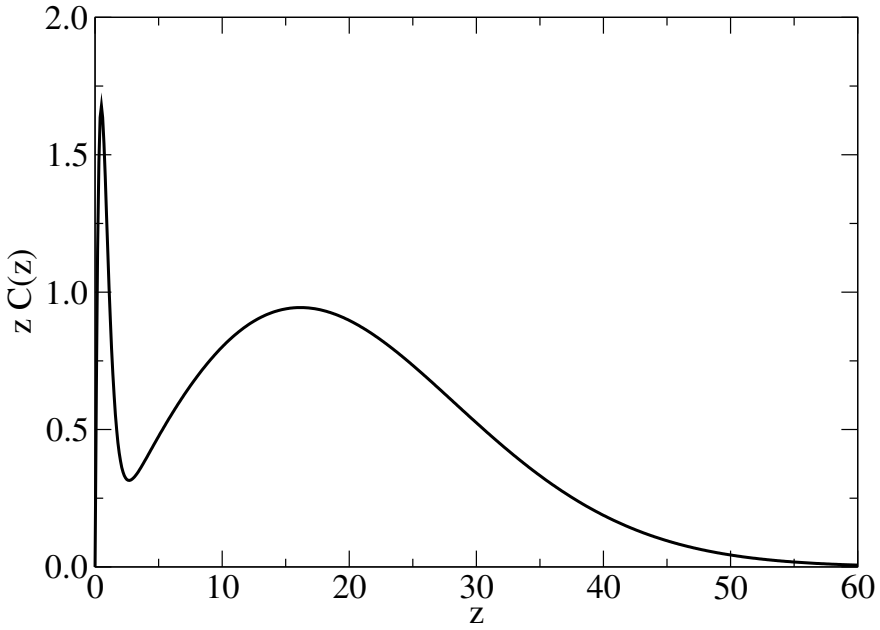

Figure 4.7: Probability density averaged over the radial coordinate and multiplied by z of the $M = -1$, $S_z = -1/2$ state of He^- in a magnetic field B=0.1 a.u. (Source: Salas & Varga [65] ©2014 American Physical Society)

B	$\langle T \rangle$	$\langle V_{ee} \rangle$	$\langle V_{Ne} \rangle$	$\langle V_{ho}/B \rangle$	$\langle V_{mag}/B \rangle$	E_{tot}
0.160	2.329	0.587	-4.943	0.943	-2.057	-2.356
0.200	2.384	0.632	-5.011	0.974	-2.026	-2.400
0.240	2.439	0.674	-5.074	0.999	-2.001	-2.441
0.400	2.664	0.811	-5.290	1.062	-1.938	-2.590
0.500	2.807	0.881	-5.406	1.088	-1.912	-2.675
0.800	3.244	1.051	-5.712	1.142	-1.858	-2.904
0.825	3.281	1.063	-5.736	1.145	-1.855	-2.922
0.850	3.318	1.075	-5.759	1.148	-1.852	-2.940
0.875	3.355	1.086	-5.782	1.152	-1.848	-2.957
0.900	3.393	1.098	-5.805	1.155	-1.845	-2.975
1.000	3.543	1.143	-5.895	1.167	-1.833	-3.042
1.200	3.848	1.224	-6.068	1.188	-1.812	-3.171
1.500	4.312	1.331	-6.314	1.214	-1.786	-3.350
1.600	4.468	1.364	-6.393	1.221	-1.779	-3.407
2.000	5.100	1.484	-6.697	1.247	-1.753	-3.619

Table 4.5: Energy contribution of different terms of the Hamiltonian for the ${}^4(-3)^+$ ($M = -3$ $S_z = -\frac{3}{2}$) configuration of He^-.

B	$\langle T \rangle$	$\langle V_{ee} \rangle$	$\langle V_{Ne} \rangle$	$\langle V_{ho}/B \rangle$	$\langle V_{mag}/B \rangle$	E_{tot}
0	5.143	0.595	-10.880	-	-	-5.143
0.001	5.143	0.594	-10.880	0.036	-2.964	-5.146
0.01	5.148	0.605	-10.896	0.293	-2.707	-5.169
0.02	5.158	0.624	-10.922	0.449	-2.551	-5.192
0.1	5.205	0.800	-11.101	0.550	-2.450	-5.341
0.16	5.254	0.884	-11.205	0.585	-2.415	-5.454
0.2	5.300	0.923	-11.273	0.626	-2.374	-5.525
0.24	5.351	0.957	-11.341	0.664	-2.336	-5.594
0.4	5.571	1.077	-11.600	0.775	-2.225	-5.842
0.5	5.715	1.143	-11.751	0.822	-2.178	-5.982
0.8	6.157	1.313	-12.161	0.917	-2.083	-6.358
0.825	6.194	1.325	-12.192	0.922	-2.078	-6.387
0.85	6.232	1.338	-12.224	0.928	-2.072	-6.416
0.875	6.269	1.350	-12.255	0.934	-2.066	-6.444
0.9	6.306	1.362	-12.286	0.939	-2.061	-6.472
1	6.456	1.409	-12.406	0.958	-2.042	-6.582
1.2	6.758	1.497	-12.635	0.991	-2.009	-6.793
1.5	7.214	1.614	-12.957	1.029	-1.971	-7.086
1.6	7.368	1.650	-13.060	1.039	-1.961	-7.179
2	7.987	1.782	-13.453	1.076	-1.924	-7.533
4	11.172	2.282	-15.172	1.182	-1.818	-8.989
5	12.795	2.477	-15.932	1.214	-1.786	-9.592
10	20.961	3.218	-19.138	1.300	-1.700	-11.958
20	37.143	4.216	-23.864	1.366	-1.634	-15.186
40	68.938	5.547	-30.438	1.412	-1.588	-19.457
50	84.667	6.060	-33.011	1.424	-1.576	-21.087
60	100.328	6.516	-35.299	1.432	-1.568	-22.520
80	131.487	7.302	-39.266	1.444	-1.556	-24.980
100	162.489	7.972	-42.661	1.451	-1.549	-27.065

Table 4.6: Energy contribution of different terms of the Hamiltonian for the ${}^4(-3)^+$ ($M = -3$ $S_z = -\frac{3}{2}$) configuration of Li.

B	$\langle T \rangle$	$\langle V_{ee} \rangle$	$\langle V_{Ne} \rangle$	$\langle V_{ho}/B \rangle$	$\langle V_{mag}/B \rangle$	E_{tot}
0	14.325	3.246	-31.895	-	-	-14.325
0.001	14.324	3.246	-31.894	0.001	-0.499	-14.325
0.01	14.324	3.246	-31.895	0.005	-0.495	-14.330
0.02	14.324	3.246	-31.895	0.011	-0.489	-14.334
0.1	14.335	3.252	-31.911	0.053	-0.447	-14.369
0.16	14.350	3.260	-31.934	0.082	-0.418	-14.391
0.2	14.363	3.267	-31.954	0.101	-0.399	-14.404
0.24	14.379	3.275	-31.977	0.117	-0.383	-14.415
0.4	14.455	3.311	-32.084	0.173	-0.327	-14.448
0.5	14.511	3.335	-32.157	0.201	-0.299	-14.461
0.8	14.690	3.399	-32.367	0.258	-0.242	-14.472
0.825	14.702	3.403	-32.379	0.261	-0.239	-14.471
0.85	14.717	3.408	-32.394	0.265	-0.235	-14.471
0.875	14.733	3.412	-32.411	0.268	-0.232	-14.470
0.9	14.748	3.417	-32.427	0.271	-0.229	-14.469
1	14.807	3.433	-32.485	0.283	-0.217	-14.463
1.2	14.925	3.460	-32.591	0.301	-0.199	-14.447
1.5	15.092	3.488	-32.718	0.319	-0.181	-14.410
1.6	15.146	3.495	-32.754	0.324	-0.176	-14.396
2	15.354	3.512	-32.871	0.338	-0.162	-14.331
4	16.485	3.561	-33.465	0.383	-0.117	-13.887
5	17.163	3.607	-33.890	0.404	-0.096	-13.599
10	21.116	3.901	-36.472	0.483	-0.017	-11.625
20	29.700	4.435	-41.425	0.560	0.060	-6.083
40	46.872	5.217	-49.204	0.622	0.122	7.764
50	55.330	5.526	-52.386	0.638	0.138	15.373
60	63.717	5.799	-55.251	0.650	0.150	23.257
80	80.309	6.271	-60.281	0.666	0.166	39.605
100	96.722	6.674	-64.642	0.677	0.177	56.492

Table 4.7: Energy contribution of different terms of the Hamiltonian for the $^2(0)^+$ ($M = 0$ $S_z = -\frac{1}{2}$) configuration of Be^+.

B	He^-		
	$^2(-1)^+$	$^4(-3)^+$	$^4(-1)^+$
0	-	-	-48.16
0.001	-	-	-48.7
0.01	-	-	-36.38
0.02	-	108.31	-26.66
0.1	1,038.67	-22.19	-0.5
0.16	411.16	-9.76	8.82
0.2	248.97	-5.68	14.41
0.24	164.92	-3.09	20.38
0.4	53.34	1.7	65.25
0.5	34.76	2.87	161.95
0.8	15.41	4.06	-
0.825	14.68	4.09	-
0.85	14.01	4.16	-
0.875	13.53	4.19	-
0.9	13.01	4.2	-
1	11.21	4.27	-
1.2	9	4.29	-
1.5	7.07	4.26	-
1.6	6.63	4.19	-
2	5.46	4.07	-
4	3.5	3.44	-
5	3.12	3.21	-
10	2.31	2.59	-
20	1.75	2.05	-
40	1.35	1.58	-
50	1.24	1.47	-
60	1.16	1.36	-
80	1.04	1.23	-
100	0.95	1.12	-
120	0.88	1.05	-
140	0.81	0.98	-
200	-	0.8	-
300	-	0.7	-
400	-	0.62	-
500	-	0.56	-
600	-	0.52	-
700	-	0.42	-
800	-	0.47	-

Table 4.8: Quadrupole moments Q_{zz} for the different configurations of He^- for different field intensities.

B	Li			
	$^2(0)^+$	$^2(-1)^+$	$^4(-3)^+$	$^4(-1)^+$
0	0	-10.81	-217.96	-4.49
0.001	0	-10.79	-217.1	-4.49
0.01	0.02	-10.7	-170.37	-4.48
0.02	0.09	-10.41	-124.5	-4.45
0.1	1.59	-6.49	-25.48	-3.73
0.16	2.94	-4.49	-15.59	-2.92
0.2	3.79	-3.61	-12.68	-2.36
0.24	4.58	-2.94	-10.74	-1.82
0.4	7.47	-1.42	-6.47	0.1
0.5	9.11	-0.94	-5.04	1.14
0.8	13.59	-0.23	-2.72	3.91
0.825	13.91	-0.19	-2.6	4.13
0.85	14.24	-0.16	-2.49	4.35
0.875	14.53	-0.13	-2.38	4.57
0.9	14.86	-0.1	-2.28	4.79
1	15.98	-0.01	-1.91	5.65
1.2	17.87	0.13	-1.37	7.34
1.5	19.84	0.26	-0.83	9.68
1.6	20.34	0.29	-0.7	10.39
2	21.63	0.37	-0.31	12.78
4	22.87	0.51	0.38	17.65
5	22.71	0.53	0.49	18.33
10	21.56	0.54	0.63	19.04
20	20.14	0.49	0.61	18.6
40	18.61	0.42	0.53	17.72
50	18.15	0.39	0.5	17.39
60	17.77	0.37	0.47	17.15
80	17.24	0.34	0.43	16.7
100	16.77	0.31	0.39	16.44
120	16.32	0.3	0.37	16.09
200	-	0.14	-	15.65

Table 4.9: Quadrupole moments Q_{zz} for the different configurations of Li for different magnetic field intensities

B	Li			
	$^2(0)^+$	$^2(-1)^+$	$^4(-3)^+$	$^4(-1)^+$
0	0	-2.67	-31.03	-1.72
0.001	0	-2.67	-31.05	-1.72
0.01	0	-2.67	-30.18	-1.72
0.02	0	-2.67	-28	-1.72
0.1	0.08	-2.53	-13.69	-1.66
0.16	0.2	-2.35	-10.59	-1.57
0.2	0.3	-2.22	-9.32	-1.49
0.24	0.4	-2.08	-8.34	-1.41
0.4	0.86	-1.61	-5.89	-1.02
0.5	1.16	-1.38	-4.96	-0.77
0.8	2	-0.9	-3.29	-0.03
0.825	2.06	-0.87	-3.19	0.02
0.85	2.13	-0.84	-3.1	0.08
0.875	2.2	-0.82	-3.01	0.14
0.9	2.26	-0.79	-2.93	0.19
1	2.52	-0.7	-2.63	0.41
1.2	3.03	-0.55	-2.16	0.83
1.5	3.75	-0.39	-1.66	1.42
1.6	3.98	-0.35	-1.53	1.61
2	4.82	-0.23	-1.13	2.34
4	7	0.03	-0.3	4.99
5	7.34	0.09	-0.14	5.64
10	7.45	0.19	0.16	6.52
20	6.96	0.22	0.26	6.43
40	6.34	0.21	0.27	6.04
50	6.16	0.21	0.26	5.89
60	6	0.2	0.25	5.77
80	5.75	0.19	0.24	5.58
100	5.57	0.18	0.23	5.43
120	5.44	0.17	0.21	5.31
200	5.05	0.14	-	4.98

Table 4.10: Quadrupole moments Q_{zz} for the different configurations of Be^+ for different magnetic field intensities.

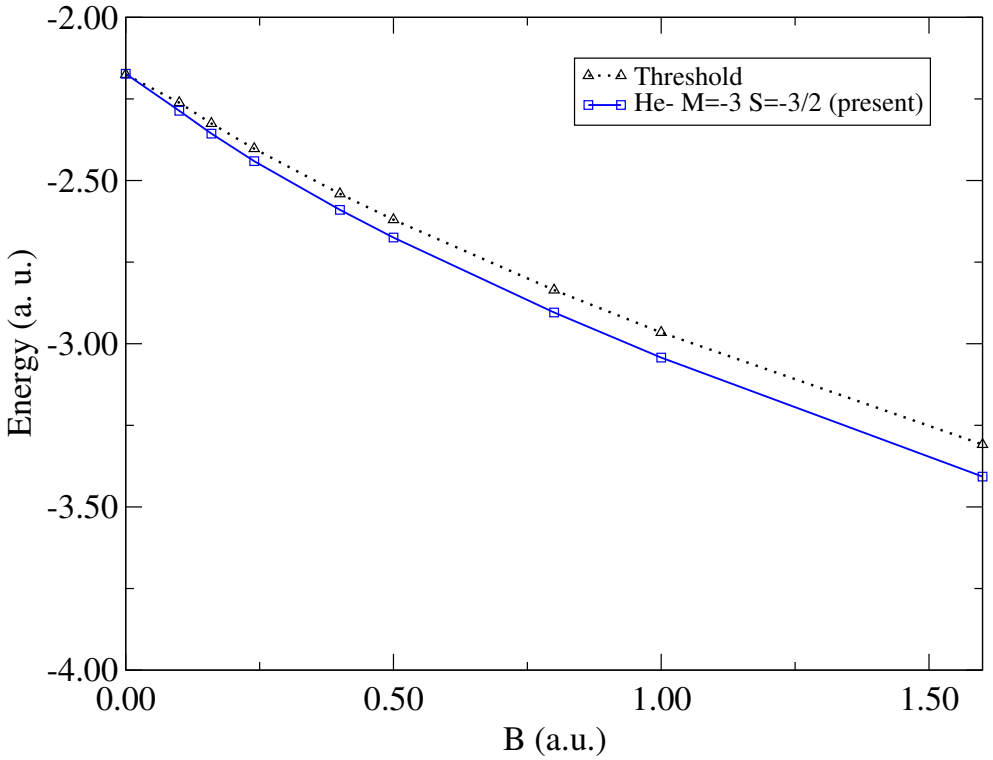

Figure 4.8: Energies and thresholds of the $M = -3$, $S_z = -3/2$ state of He^- for different magnetic field intensities. (Source: Salas & Varga [65] ©2014 American Physical Society)

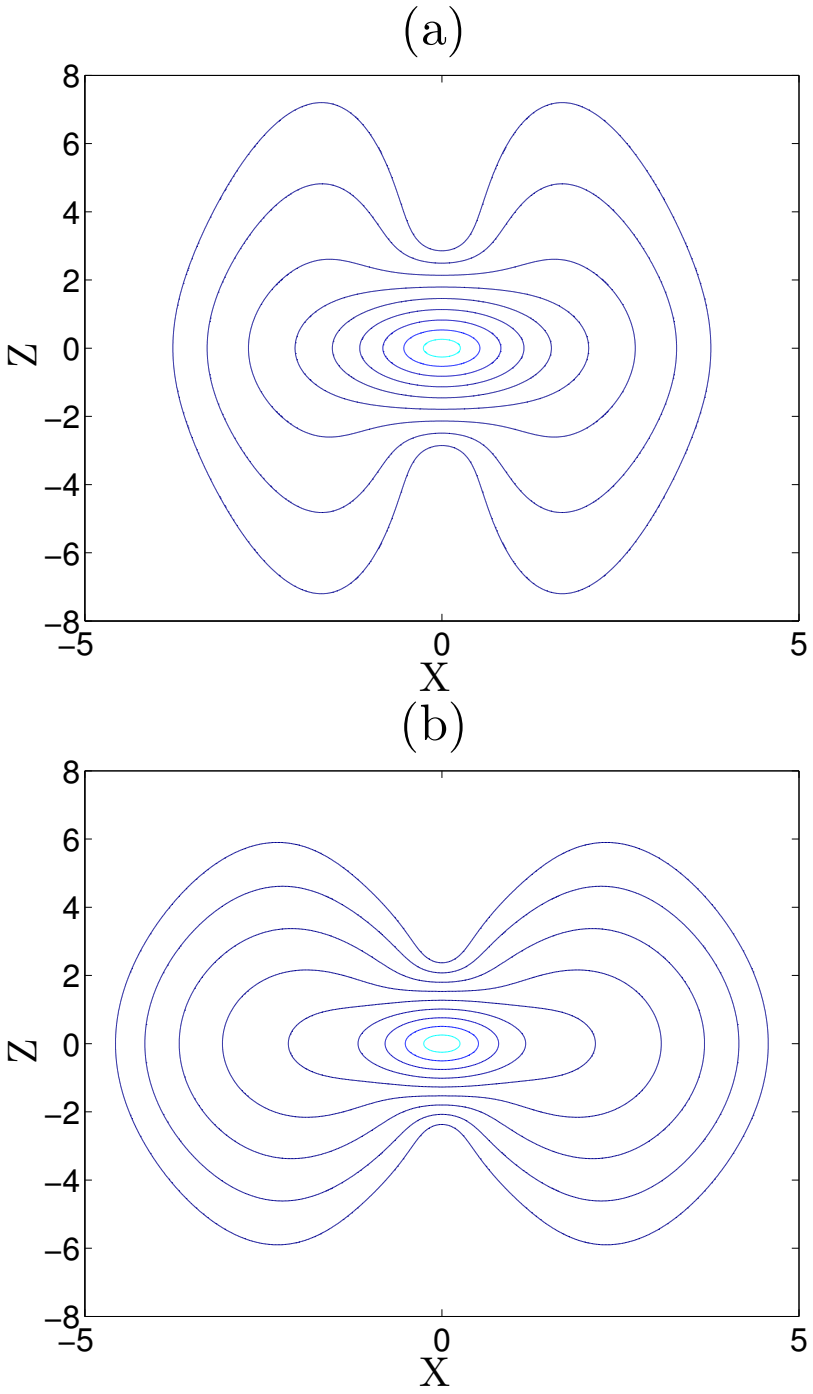

Figure 4.9: Density contour plots of He^- at the transition point. Neighboring lines differs from each other by factor of e. (a) $M = -1$, $S_z = -\frac{1}{2}$ near the transition point, for $B = 0.70416$ a.u. (b) $M = -3$, $S_z = -\frac{3}{2}$ near the transition point, for $B = 0.70416$ a.u. (Source: Salas et. al. [66] ©2015 American Physical Society)

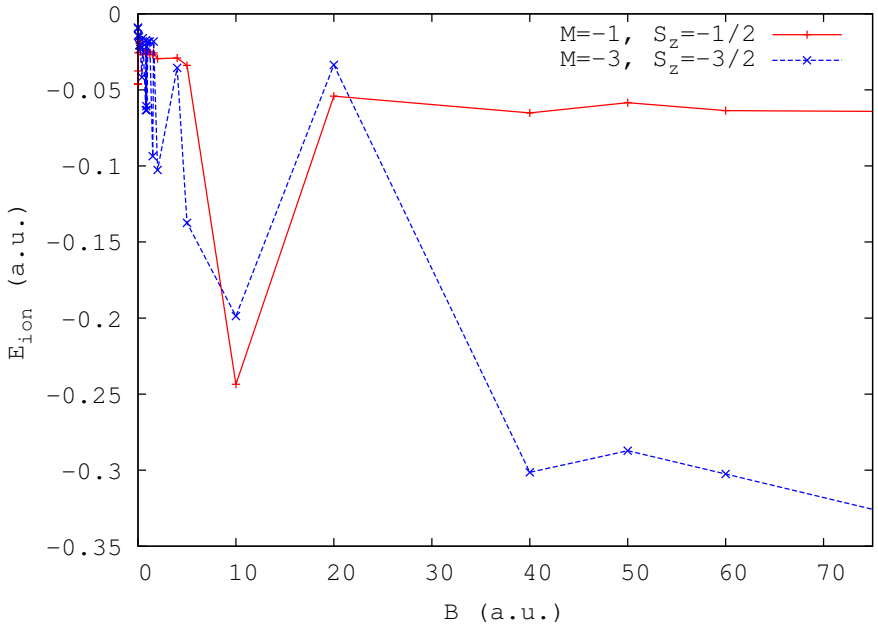

Figure 4.10: The ionization energy for H^{2-} is plotted for different field strengths. All the values of the energy are below zero, so no bound states are found.

4.6 The stability of H^{2-}

No bound states were found for H^{2-} , The energies and threshold were calculated for configurations ${}^2(0)^+$, ${}^2(-1)^+$, and ${}^4(-3)^+$. No bound states were found. The values obtained can be seen in Fig. 4.10. The limitation to this result is that the energy is obtained from two different calculations, so it carries the variational overestimate of both of them.

This result sets up a lower bound of $Z = 1$ for the minimum nuclear charge needed to bind a three-electron system together. Finding the critical charge under strong magnetic field conditions is feasible although computationally expensive.

4.7 Diamagnetism in strong fields

The quantity $\langle V_{mag} \rangle$ in Eq.(4.11) can give us some insight on the dominance of diamagnetism or paramagnetism on the system. We divide this by B so the asymptotic values can become more apparent. For the studied states $M < 0$ and $S_z < 0$, so the paramagnetic

contribution is always negative or zero. Therefore if $\langle V_{mag} \rangle < 0$ the paramagnetic term has a greater magnitude than the diamagnetic term, which is always positive.

The Langevin model [9] is typically used for describing diamagnetism in atoms with bounds electrons. In this model the magnetic field is treated as a perturbation. The diamagnetic dipole moment is given by [154]:

$$\mu_{dia} = -\frac{\partial E'}{\partial B} = -2\frac{B}{8}\sum_i \langle \rho_i^2 \rangle = -2\langle V_{dia} \rangle / B, \tag{4.12}$$

The paramagnetic dipole moment is given by:

$$\mu_{par} = \frac{1}{2}(M + 2S_z) \tag{4.13}$$

Typically both the paramagnetic and diamagnetic terms give very weak contributions, with the paramagnetic usually being the larger one. Diamagnetism becomes more noticeable with atoms that have closed shells and paired spins because the paramagnetic term vanishes.

However these trends can break under very strong magnetic field conditions, as shown by our results. The paramagnetic term, depends linearly on the magnetic field, and the magnetic moment,Eq.(4.13), has a fixed value for a given configuration. On the other hand, the diamagnetic term,Eq.(4.8), has a quadratic dependence on the field, so the diamagnetic dipole moment is not a constant.

The values of $\langle V_{mag} \rangle / B$ are shown in 4.11. For lower fields they all exhibit a more paramagnetic behavior, as expected. However when the field increases, then $\langle V_{mag} \rangle / B$ becomes less negative, and in some cases has positive values. This indicates that the diamagnetic behavior of the atom becomes more significant as the field is increased.

The magnitude of the diamagnetic dipole moment is plotted in Fig. 4.12. The paramagnetic dipole moments of the studied configurations are marked as horizontal lines. We can observe that the magnitude of the diamagnetic dipole moment can exceed that of the

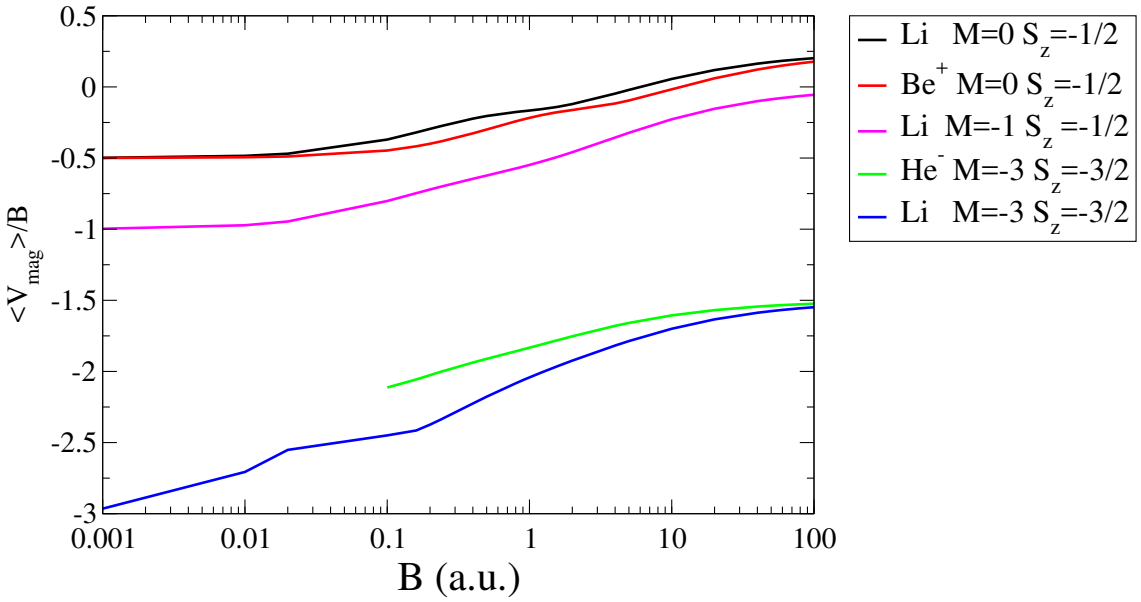

Figure 4.11: The magnetic contribution, $\langle V_{mag} \rangle / B$, is plotted as a function of the magnetic field. The increase reveals the increment in the diamagnetic term.

paramagnetic one. However, the limitation to this result is that the field produced by the electrons themselves is not accounted for, which in turn can affect the magnetic moment. This field is not uniform, and including it into the model may not be a simple task.

4.8 Limitations of the model

We must consider the fact that our results do not account for the magnetic field produced by the atom itself, due to its paramagnetic or diamagnetic character. As the diamagnetic moment increases the magnetic field should be diminished in a realistic system.

At very small distances the internal magnetic fields can become significant. Additionally the internal magnetic fields of the atom are non-uniform and have components in all directions, and they are neglected in the current work. Making a computational model that accounts for this is not easy. This lack of field uniformity also has implications for the formation of molecules or solids. Having a non-uniform field produced by the atom itself

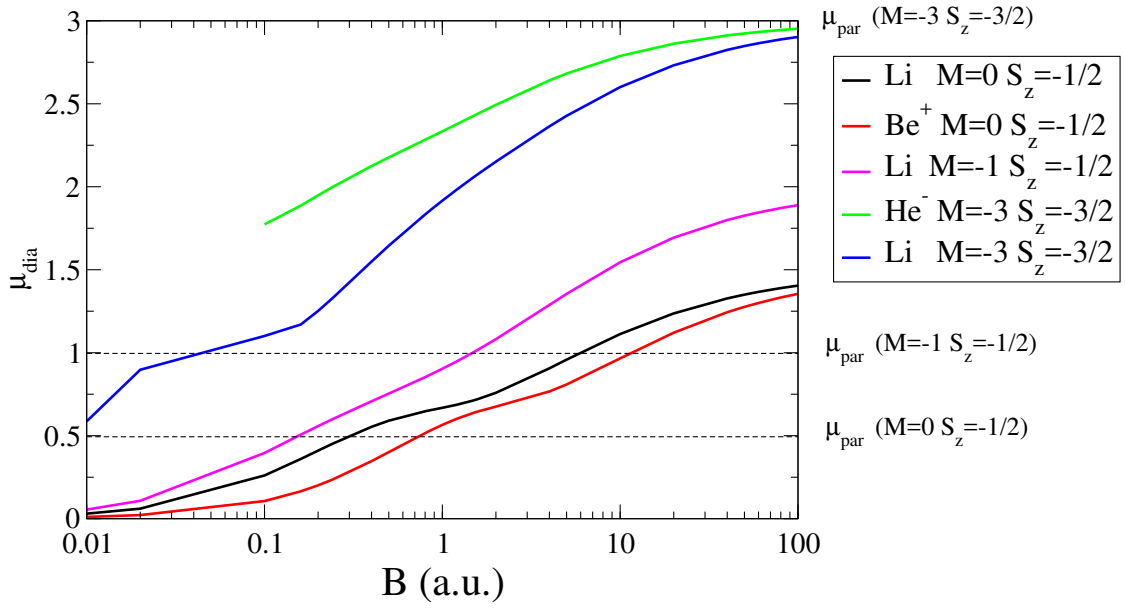

Figure 4.12: Magnitude of the induced diamagnetic dipole moments, μ_{dia}, for several studied systems. The paramagnetic dipole moment, μ_{par} , is given for the three configurations considered.

would also alter the behavior of neighboring atoms, also affecting their induced magnetic moments, similar to a ferromagnetic material. Also, since the field is non-uniform, that would imply that there is a force acting between the atoms, which will affect the stability of the new composite system.

The movement of the center of mass of the system can also play a significant role, if the nuclear mass is not infinite. This motion is coupled to the electronic motion, and other works have shown that it can change the stability of the system by limiting the number of existing bound states, which in some cases can render it unstable [68, 70, 77, 109]. Additionally thermal effects could also affect the formation of magnetically induced anions.

Another limitation is that this is a non-relativistic model. Such effects are neglected as well as QED, and corrections might be needed to get a more accurate picture. For example, the gyromagnetic factor for the electron is taken as 2 for consistency with the literature, which is in general of little importance, but it becomes more noticeable for stronger fields.

CHAPTER 5

INTERACTIONS WITH ELECTRIC FIELDS

5.1 Introduction

In the present chapter we explore the use of the SVM method to simulate the interactions of atoms with external electric fields, and use it to study the Mollow sideband generation and the high harmonics in the case of a hydrogen atom. We simultaneously employ a separate method, a confined hydrogen model, to corroborate the results. This chapter is organized as follows: we first give an introduction to the application of external electric fields and their effects. We then describe the method employed to construct the Gaussian basis in 5.2 and the confined hydrogen atom model in 5.3. Then the method used for the time dependent calculations is shown in 5.4. Afterwards we then demonstrate the use of the Gaussian basis for long wavelength ionization conditions in 5.5.1, and then study the Mollow sideband generation and its high harmonics in 5.5.2.

5.1.1 External electric fields

The application of a static external electric field on an atom gives rise to the well known Stark effect. If the external field is weak then this can be treated using perturbation theory [5]. However, as the electric field becomes larger the perturbative approach can fail. In this perturbative treatment the wavefunction is expanded in terms of bound atomic orbitals, which is a bad approximation for strong fields. The transitions between the bound states and the continuum states must be accounted for properly to get reliable results in such case.

The Stark effect for the hydrogen atom can be described in an exact manner by the use of parabolic coordinates for a static field [155]. However, for more complex systems or time-dependent fields this is no longer the case and other methods must be employed.

Different effects can arise upon the application of a strong electric field, and in the

present work we focus on the ionization, high harmonic generation and generation of Mollow sidebands and their simulations using a Gaussian basis, with the assistance of the Stochastic Variational Method. We also use a confined hydrogen model for comparison.

5.1.2 Ionization

A strong external electric field competes with the coulombic, and can cause ionization if it is intense enough. Two mechanisms can be responsible for this: *Over-the-barrier* and *Tunnel* ionization. The former is produced when the electron has enough energy to escape the barrier classically, while in the latter case is a purely quantum phenomena and the electron escapes by means of the tunnel effect. For this to take place the potential barrier has to be lowered long enough, so the process is favored the most when the laser frequency is low.

The ionization probability will be dependent on factors such as the laser intensity, wavelength, pulse shape and energy of the electron. The time it takes for the electron to get through the depressed Coulomb potential is approximately $\tau \approx L/v = 2I_p/F$, where I_p and F are the ionization potential and electric field strength respectively. There exists a quantity called the Keldysh parameter which is used as a guideline to determine the dominant ionization mechanism. It is obtained from the ratio of how fast the barrier oscillates and the time it takes for the electron to ionize by tunnel effect. The Keldysh parameter is given by [156]:

$$\gamma = \frac{\omega\sqrt{I_p}}{F}. \tag{5.1}$$

When $\gamma \ll 1$ it indicates the dominant mechanism is tunneling ionization, while the $\gamma \gg 1$ instead is for the multiphoton ionization regime [156]. Nevertheless it is important to note that the Keldysh parameter, for as popular as it may be, can also be misleading in some circumstances, as explained in Ref.[156] and references within.

5.1.3 High Harmonic Generation

The interaction of atoms with strong electric fields is known to give rise to high harmonic generation (HHG). This process has been the subject to extensive research in the literature and its description is given by the *3-step model* [157].

The first step of such model is the tunnel ionization of the electron through the Coulomb barrier. The electron then departs the atom and travels a certain distance before stopping. The electron is then rescattered back towards the nucleus where it recombines, giving off energy at higher harmonics of the laser frequency [157].

The emission and absorption of radiation by atoms in time dependent electric fields depends on the oscillations undergone by the electrons [5]. If the laser is linearly polarized along the z axis then the corresponding observable of interest is the expectation value of the dipole moment as a function of time, along such axis:

$$d(t) = \langle \psi(t)|z|\psi(t)\rangle, \tag{5.2}$$

where z is the spatial coordinate and $\psi(t)$ is the wavefunction at a given time.

The HHG spectrum is determined by the oscillations of the dipole moment in frequency domain. It can be calculated from the Fourier transform of the dipole moment[1, 158]:

$$\tilde{d}(\omega) = \frac{1}{\tau}\int_0^\tau d(t)e^{-i\omega t}dt \tag{5.3}$$

The harmonic spectrum of the dipole moment is then given by:

$$P_d(\omega) = |\tilde{d}(\omega)|^2 \tag{5.4}$$

A commonly used form for the HHG spectrum is the dipole acceleration, $\tilde{d}_{acc}(\omega) = \ddot{\tilde{d}}(\omega)$. Sometimes $\ddot{\tilde{d}}(\omega)$ is not hard to calculate directly, depending on the basis functions employed.

However, it is common to employ its approximate form [158]:

$$\tilde{d}_{acc}(\omega) \approx \omega^2 \tilde{d}(\omega), \tag{5.5}$$

for which the harmonic spectrum is then given by:

$$P_a(\omega) = |\omega^2 \tilde{d}(\omega)|^2. \tag{5.6}$$

The harmonic generation has a classical cutoff energy, after which the spectral amplitude decays significantly. This cutoff is given by [158]:

$$E_{cut} = I_{pot} + 3.17 U_{ponde}, \tag{5.7}$$

where E_{cut} is the classical cutoff energy, I_{pot} the ionization potential and U_{ponde} the ponderomotive energy, determined by the intensity I and angular frequency ω of the external field:

$$U_{ponde} = \frac{I}{4\omega^2}. \tag{5.8}$$

5.1.4 The Mollow sidebands

Whenever a two-level system is driven by a resonant strong external field the resulting spectra can exhibit sidebands accompanying the driving frequency. Such sidebands, known as Mollow sidebands [159] appear as a consequence of the Rabi frequency becoming comparable to the frequency of the laser, giving a triple peak structure in the spectra known as the Mollow triplet[160], rather than the sole driving frequency.

The Rabi frequency is defined as:

$$\Omega_R = \frac{d_{ij}\varepsilon}{\hbar} \tag{5.9}$$

where d_{ij} is the dipole moment of the transition between two levels, and ε the amplitude of the applied electric field. This quantity gives the rate at which the system is driven from the populated lower state regime (absorption dominant) to the upper state (stimulated emission dominant) being populated [161, 162].

It is very common to study quantum systems assuming that Ω_R, is much smaller than the driving frequency ω_L, in such way that the population of the levels does not affect the signal significantly. However, in the presence of a very strong field this assumption may no longer be true. In a two-level system this creates sideband frequencies given by $\omega_L \pm \Omega_R$ [163].

Previous works, experimental and theoretical, have studied quantum dots [164], GaAs [165], the hydrogen atom [166], molecules [159], solid state [167], atoms [166, 168] and optical cavities [169, 170]. There has been little interest in investigating the Mollow sidebands in the past because of the high laser intensities required to observe them, but recent developments in laser technologies have changed this. The interest in these sidebands arises from the possibility of tuning the output frequency by means of adjusting the intensity of the input beam [166, 171].

Some recent theoretical and computational works have focused on hydrogen[166] and alkali atoms [168] since they only have one active electron. For the case of hydrogen it was shown that visible light can be produced by exciting the atom with a strong laser resonant with the transition between 1s and 2p states [166]. This was done using a strong field approximation and solving the time-dependent Schrödinger equation with a pseudospectral approach[166]. In such work the changes in the peak structure were predicted theoretically and shown to be in good agreement with the computation [166].

In Ref.[168] alkali atoms were chosen over others to employ the single active electron approximation, avoiding complications such as electron correlation effects, whose role in HHG is not well understood [168]. The effect of the Mollow sidebands on HHG generation was studied computationally for sodium and potassium atoms. The effects of the

Rabi flips were seen in the third harmonic of potassium, which was stimulated with a frequency resonant with a transition, while comparing them to the spectra of sodium, which was stimulated off-resonance. Changes in the peak structure of the third harmonic were clearly visible and they could be correlated to the Rabi oscillations[161], evidenced on the population of the ground state.

One could start by assuming a simple 2-level model for any atom, but the problem is that two-level atomic system approximations are only good for in the case of relatively weak fields. In the presence of strong fields other effects must be accounted for such as population other levels and ionization. This is easiest to do for a single-electron system, so we make the hydrogen atom the focus of this chapter.

The present chapter addresses the generation of Mollow sidebands for the hydrogen atom and the study of their effects on the harmonic spectrum, as well as the roles of the bound states in the generation of the third harmonic, which to the best of our knowledge has not been previously investigated. This is done using a Gaussian basis and a confined hydrogen model, which will allow approximating transitions into unbound states, going beyond the 2-level approximation. The Mollow sidebands are of interest because of their potential applications for controlling the generation of frequencies by means of adjusting the amplitude of the driving electric field.

5.2 Representation of unbound states using Gaussian basis

One of the big challenges for computation is representing unbound states. The problem with such states is that they are associated to a continuum spectrum of allowed energies, so some form of discretization is needed to work the problem computationally. Loosely bound states can also be problematic to simulate because of their large spatial extension and small spacing between energies.

A typical solution for this problem is to employ methods based upon representation of the wavefunction on spatial grids [1]. This is computationally expensive, although still fea-

sible for single-electron systems. Grid based methods can also have difficulties representing singularities, so softened potentials are commonly used in these cases. Additionally, the simulation box boundaries can cause artifacts and affect the results, so methods such as mask functions or complex absorbing potentials are needed, which in turn can cause other artifacts.

Other methods of approximation include the use of basis functions such as Coulomb wavefunctions [172], plane waves [1], Volkov states[173] and Gaussians [174, 175].

5.2.1 Spherical Bessel and Coulomb wavefunctions

The Spherical Bessel functions [176, §10.47] constitute the exact eigenstates of a particle in free space in spherical coordinates [5]. In contrast, the Coulomb wavefunctions [176, §33] are the exact positive energy eigenstates for a hydrogen-like atom. The Spherical Bessel functions have certain advantages over the Coulomb because they can be integrated analytically in many cases, their zeros are easier to compute and they form a complete set, making them usable for wavefunction expansions. However, the drawback is that diagonalizing the Hamiltonian in this basis can have slow convergence depending on the central potential (e.g. Ref.[177]). The Coulomb wavefunctions have been extensively studied for nuclear and atomic physics (e.g. Ref.[176, §33.22] and references within) and many approximations that can be useful for computations are known (See Refs.[178–180] and within).

Both of these functions can be computed numerically with very good accuracy. However, these are intended for systems with one particle and extending them to more by taking the tensor product of the single particle basis, but this rapidly increases the computational burden.

5.2.2 Gaussian representation of scattering and Rydberg basis

A Gaussian basis representation could also be used for continuum states. Nevertheless they are limited to wavefunctions with few oscillations [12]. Highly oscillatory wavefunctions having more than about 5 nodes are difficult to represent accurately[181, 182].

For a single-particle system with low energies specific sets of Gaussian functions for representation of the continuum have been developed [174, 175]. The Nestmann basis [174] is used for the case of representing Spherical Bessel Functions, while the Kaufmann basis [175] is optimized instead for representing Coulomb wavefunctions. The latter is used for hydrogen-like systems and also for more complex atoms under the Single Active Electron (SAE) approximation.

The Kaufmann basis for continuum states has the form:

$$r^l \exp(-\alpha_i r^2) Y_{lm}(\theta,\phi), \tag{5.10}$$

with the exponents given by

$$\alpha \simeq \frac{1}{4\left(a_l n + b_l\right)^2},\ (n = 1,2,..N)\,. \tag{5.11}$$

Additionally there exists a modified form of the Kaufmann basis optimized for representation of Rydberg states[175], given by:

$$\alpha \simeq \left(\frac{Z}{2n}\right)^2 \frac{1}{\left(a_l n + b_l\right)^2},\ \left(n = 1, \frac{3}{2}, 2, \frac{5}{2}, ..N\right). \tag{5.12}$$

The subscript l denotes the angular momenta and the values of a_l and b_l given in Ref.[175] are shown in Table 5.1.

l	a_l	b_l
0	0.584342	0.424483
1	0.452615	0.309805
2	0.382362	0.251333
3	0.337027	0.215013
4	0.304679	0.189944

Table 5.1: Numerical values of a_l and b_l employed by the Kaufmann basis. These values are taken from Ref[175].

5.2.3 Stochastically enhanced Kaufmann basis

The Gaussian basis can be used with SVM to calculate the ground state very accurately, and the first few excited states. However for obtaining the Rydberg states the use of the SVM does not work well because these states require accurate calculations of all the lower states. Unbound states are therefore also problematic for the SVM for the same reason.

On the other hand, the Kaufmann basis can handle the Rydberg and continuum states in a reasonable manner, but it fails to give an accurate ground state, as one can observe in Table 5.2. A solution to this problem is to combine the Kaufmann basis with the SVM calculated basis, to get an accurate ground state, Rydberg and continuum levels at the same time.

It is important to note that it is not only the energies that need to be accurate, but also the dipole moments, which converge slower than the energies. If the ground state is not well converged then in accordance to the variational principle the initial energy of the electron will be higher, and can therefore alter the spectrum and ionization probabilities. For example, a badly converged ground *s* state would give an initial state that is a superposition with excited *s* states. Such combinations are known to be capable of augmenting the HHG emission as suggested from the findings in Ref.[183].

Additionally, the Rydberg states also play an important role in high harmonic generation, as it has been shown in previous works[184], so they must be accounted for.

Basis size	E_{gs}
12	-0.490452931051526
18	-0.490554731428998
24	-0.490762390914084
30	-0.490863150594297
36	-0.490917141044641
42	-0.490949591549928
48	-0.490970782433204
54	-0.490985504725198
60	-0.490996227764664
66	-0.491003972653931
Exact	-0.500000000000000

Table 5.2: Ground state energies E_{gs} (in a.u.) obtainable using the Kaufman basis for different sizes. The convergence is very slow, and numerical accuracy issues arise for a large basis.

Accuracy

The SVM method converges quite rapidly for the hydrogen atom, as shown in Table 5.3. The calculation for each angular momentum configuration is done separately. There is a limit on the basis size due to numerical accuracy, which can take place if the basis is too large.

The convergence of the dipole moment matrix elements for the SVM method is also important, and it can be harder because it requires the wavefunction to have the correct shape. We show the convergence of the 1s-2p transition dipole matrix element $\langle \psi_{1s}|z|\psi_{2p}\rangle$ for different basis sizes in Table 5.4 as an example. This transition is probably the most important ones in general because of its high oscillator strength, and also plays an essential role in Mollow sideband generation, as it will be discussed later.

The energies for the first states obtained of the enhanced Kaufmann are plotted in Fig. 5.1, along with the exact energy for l=0-2. This shows that the basis has good agreement for the theoretical values of the lowest Rydberg states. An advantage of enhancing the

N_{basis}	1s	2s	2p
5	-0.499373591465410	-0.124568605293151	-0.124941534826204
8	-0.499927894211061	-0.124989591784600	-0.124999284321507
12	-0.499998746913927	-0.124997993274760	-0.124999952453690
15	-0.499999312985810	-0.124999911998884	-0.124999974359063
20	-0.499999975996560	-0.124999995549977	-0.124999999443980
25	-0.499999998129445	-0.124999999728159	-0.124999999642637
Exact	-0.500000000000000	-0.125000000000000	-0.125000000000000

Table 5.3: Energies (in a.u.) obtainable using the SVM for the 1s, 2s and 2p states for different basis sizes N_{basis}. The 1s and 2s presented are obtained in the same calculation, whereas the 2p is done separately because it has a different symmetry.

Kaufmann basis is that the number of Rydberg or unbound states can be increased if needed by adding more functions using the procedure described in Ref.[175].

5.3 Confined Hydrogen model

Another way to represent the continuum states is to confine the atom with an impenetrable barrier at a radius r_0 [186]. This confinement makes the unbound continuum states become discrete ones. This method has been previously shown to be capable of giving accurate results for the photoionization cross section [186].

The calculation of HHG spectra for the confined hydrogen model is done in three stages. One first solves the time-independent Schrödinger equation for the allowed states inside the box to obtain a basis. Afterwards one calculates the matrix elements. A time propagation scheme is then employed to obtain the HHG spectrum, described in section 5.4.

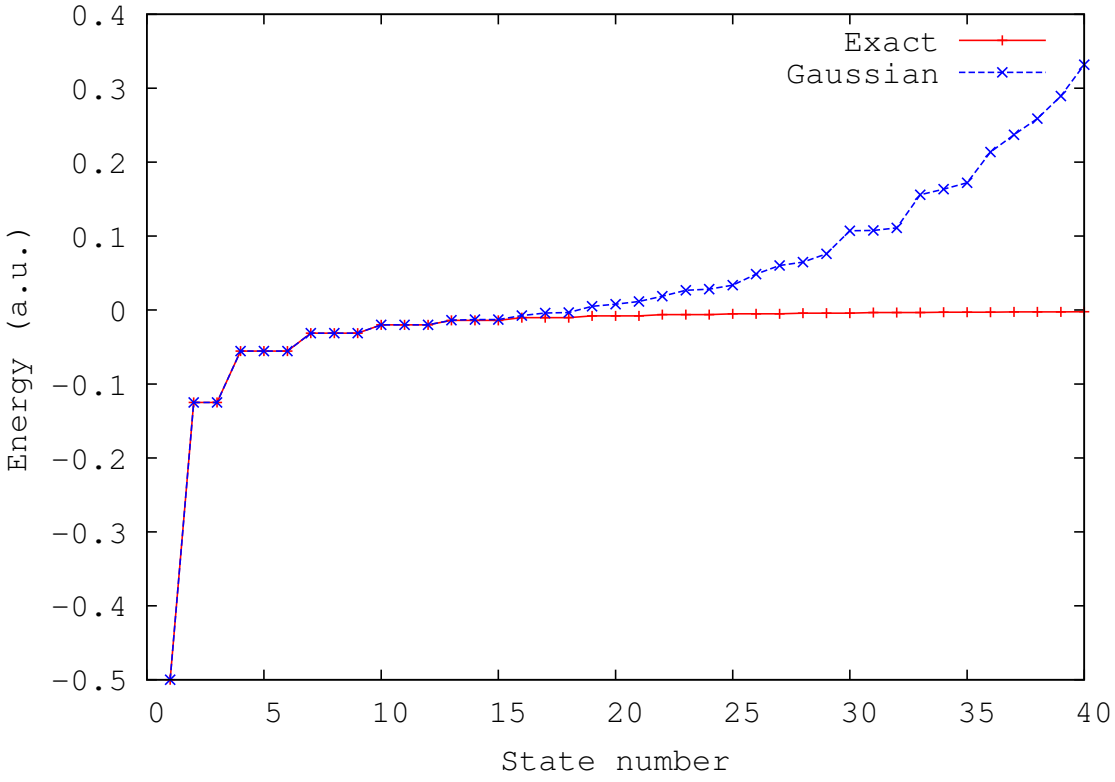

Figure 5.1: The energies for each hydrogen state calculated by enhancing the Kaufmann basis are shown along the exact energies of a hydrogen atom for l=0-2. We can observe there is a good agreement between them for the Rydberg states.

Basis size	$\langle \psi_{1s} \vert z \vert \psi_{2p} \rangle$
10	0.752278413251
16	0.745100377081
24	0.744924753679
30	0.744936719120
40	0.744935585851
50	0.744935539651
"Exact"	0.744935539028

Table 5.4: The dipole moment matrix element of the 1s-2p transition, $\langle \psi_{1s} \vert z \vert \psi_{2p} \rangle$, is given for different basis sizes. Each basis has an equal number of s and p basis functions. The "exact"value was obtained by using the explicit formula from Ref. [185], and it is limited only by numerical accuracy.

5.3.1 Hamiltonian of the confined hydrogen atom

The Hamiltonian for a Hydrogen atom confined inside a box, in a.u., is given by:

$$\hat{H}_0 = -\frac{\nabla^2}{2} - \frac{1}{r} + V(r), \tag{5.13}$$

where $V(r)$ is the confinement potential. For an impenetrable barrier it is given by:

$$V(r) = \begin{cases} 0 & , \quad r < r_0 \\ \\ \infty & , \quad r > r_0 \end{cases} \tag{5.14}$$

For the inner region we then have a similar solution as that of the free atom, and the eigenvalue problem reduces to solving the eigenvalue problem Eq.(5.15).

$$-\frac{\nabla^2}{2}\psi - \frac{1}{r}\psi = E\psi, \tag{5.15}$$

The solution of Eq.(5.15) is of the form [187]:

$$\psi = \sum_{lm} R_l(r) Y_{lm}(\theta, \phi) \tag{5.16}$$

where $R_l(r)$ are the reduced radial wavefunctions and Y_{lm} are spherical harmonics. Its is common to write the solution in term of the reduced radial wavefunction [187]:

$$u_l(r) = rR_l(r). \tag{5.17}$$

The reduced form of the time-independent Schrödinger equation inside the radius r_0 is then:

$$-\frac{1}{2}\frac{d^2u_l}{dr^2} + \left(-\frac{1}{r} + \frac{1}{2}\frac{l(l+1)}{r^2}\right) u_l = Eu_l. \tag{5.18}$$

The wavefunction must comply with the Dirichlet boundary condition:

$$u_l(r_0) = 0 \tag{5.19}$$

The continuum eigenstates of the free atom become discretized due to the confining potential, and although they are now bound states confined by the box, we will continue to refer to them as unbound states to distinguish them from the ones bound by the nucleus. The two possible cases, positive energies (unbound) and negative ones (bound states), will be examined separately in section 5.3.2

In the presence of an electric field $\varepsilon(t)$, polarized along the z axis, the Hamiltonian of a hydrogen atom inside the confining box becomes:

$$\hat{H} = \hat{H}_0 - d_z\varepsilon(t), \tag{5.20}$$

where H_0 is the field-free Hamiltonian Eq.(5.13) and d_z is the dipole moment along the z direction.

5.3.2 Allowed Energies

The solution of 5.15 is given by a form of the confluent hypergeometric function for both positive and negative energies. However, different forms of the solution are employed for each case, so the calculations are done separately.

For positive energies the reduced radial eigenfunctions $u_l(r)$ are the Coulomb wavefunctions, F_l which can also be written in terms of the Whittaker M function $M_{a,b}$, [176, see 33.2]:

$$F_l(\eta, kr) = C_l(\eta) 2^{-l-1} (\mp i)^{l+1} M_{\pm i\eta, l+\frac{1}{2}}(\pm 2ikr), \tag{5.21}$$

where η and the wavenumber k and energy E are related by:

$$\eta = -1/k \tag{5.22}$$

$$k = \sqrt{2E}. \tag{5.23}$$

The Whittaker M function is related to the confluent hypergeometric function by means of a Kummer transformation [176, see 13.2.39]. Both the Whittaker M and Coulomb functions have the same zeros, so for the purpose of calculating the allowed wavenumbers either one can be used. Both give accuracies that are sufficient for the current work. The Coulomb Wavefunctions can be obtained from the GNU Scientific library (GSL)[188] and the Whittaker M functions, with real and complex inputs, are available in MATLAB [189] as well as in the *Mpmath*[190] library for Python.

Solving for the allowed positive energies of the system is done in several steps. First it is necessary to isolate the roots of the wavefunction in separate intervals. We can then

proceed to solve numerically for the zeros of the Coulomb/Whittaker function evaluated at $r = r_0$, which will give the allowed values of k. The energies are then obtained from equation Eq.(5.23).

Since the wavefunction is smooth it is not hard to isolate the zeros. This was easily done by spanning out the radial wavefunction $R_l(kr_0)$ on a grid with 50 000 points corresponding to values of k between 10^{-10} and 10 a.u. Afterwards a peak detection algorithm was employed on the absolute value of the wavefunction to get the maxima and minima. These points correspond to the limits of the intervals where the search for the roots is to be conducted by the *fzero* solver, which is available in MATLAB/Octave or the Anderson solver available in *Mpmath*. In Fig. 5.2 we show an example of a calculation using this method for $r_0 = 500$ a.u. and $l = 0$. The absolute value of the wavefunction at $r = r_0$ is plotted as a function of k, together with the detected peaks and the located zeros. As k increases the zeros appear on a quite regular pattern, approximately in the midpoint between the peaks. The values obtained by the *fzero* solver can be easily inspected for correctness and accuracy. We must point out that the accuracy decays as l increases, but it is still sufficient for the purpose of this work.

We expect the effects of the confinement to be noticeable mostly due to the discretized energies and their separations rather than small energy shifts. We can see in Fig. 5.2 that the obtained positive energies are well separated, so small errors in their values should not be expected to make a significant difference.

For negative energies the solutions can be obtained from finding the roots of the Whittaker function:

$$R_l(r_0) = M_{\xi,l+1/2}(2r_0/\xi) = 0. \tag{5.24}$$

The value ξ in Eq.(5.24) is not necessarily an integer, and can take only certain positive values depending on the location of the radius of the box. In the limit $r_0 \to \infty$ then $\xi = n$, the principal quantum number which is an integer.

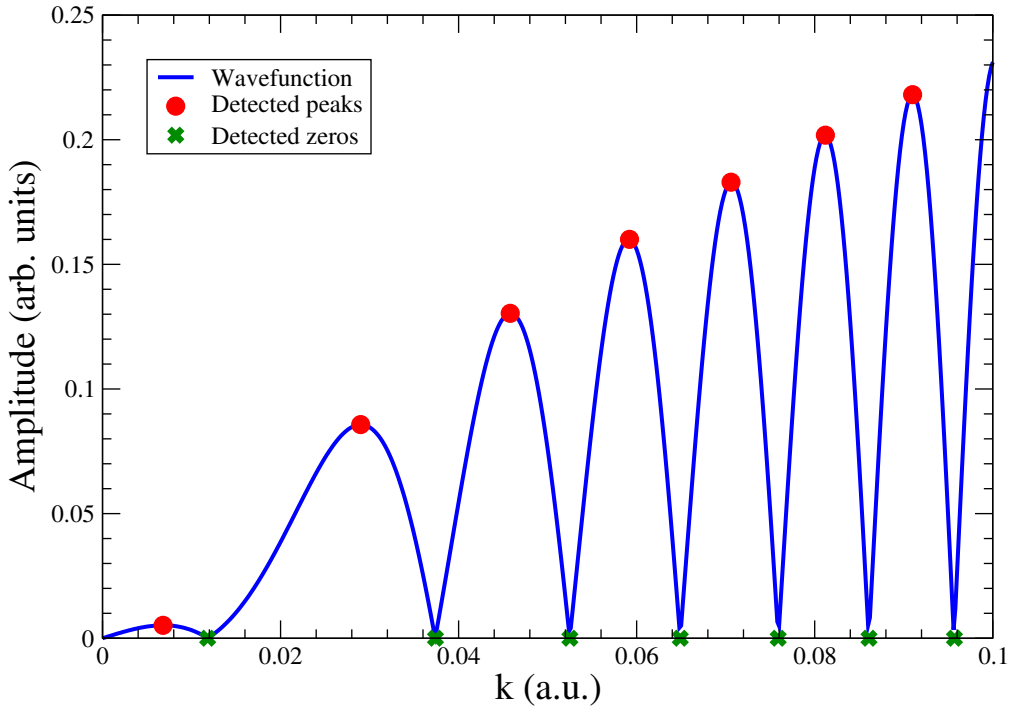

Figure 5.2: Plot of the magnitude of the Whittaker M function at $r_0 = 500$ a.u. for l=0. The detected peaks are marked, as well as the location of the detected zeros. As k gets larger the zeros tend to appear with more regular spacings. For other values of l the curves are very similar to the one depicted.

The negative energies of a hydrogen atom, confined or free, are given by:

$$E_\xi = -\frac{0.5}{\xi^2}\, a.u. \tag{5.25}$$

Whenever the boundary is far away many of the lowest eigenstates are mostly unperturbed because they have exponentially decaying tails which approximately comply with the Dirichlet boundary condition Eq.(5.24). This can be seen in Fig. 5.3, where the ground state wavefunction (unnormalized) is plotted for different confinement radii and can be seen to converge rapidly. If the confining wall is very distant the ξ values tend to be very close to their integer parts. The allowed values of ξ for some orbitals are plotted for different confinement radii in Fig. 5.4. The energy shift for the ground state, with the same r_0, is far beyond the representable range with a machine double precision variable. One can neglect the effect of the confinement for low energy Rydberg states if very high accuracy is not needed.

For large n or small r_0 the confinement can produce energy increments that are big. For a given value of n there is a critical value of r_0 for which the corresponding energy of the orbital becomes positive [191]. Conversely, this means that for a given r_0 there is a critical value of n for which the states cease to have negative energy. The exact value of the critical radius r_{crit}, for a given n and l, can be calculated from the expression [191]:

$$r_{crit}(n,l) = \frac{1}{8}\left(x_{2l+1,n-l}\right)^2, \tag{5.26}$$

where $x_{\nu,i}$ represents the ith zero of the Bessel function $J_\nu(z)$. The values of r_{crit} are given for some values of n and l in Table 5.5 and plotted in Fig. 5.5 for $l = 0$. The difference between critical radii for states with the same n tends to differ only by few atomic units, so the $l = 0$ provides a good guideline for all angular momenta. As the quantum number n becomes larger so does r_{crit} because the size of the box can be larger avoiding making the energy positive. On the other hand for a fixed quantum number n a state with higher l has

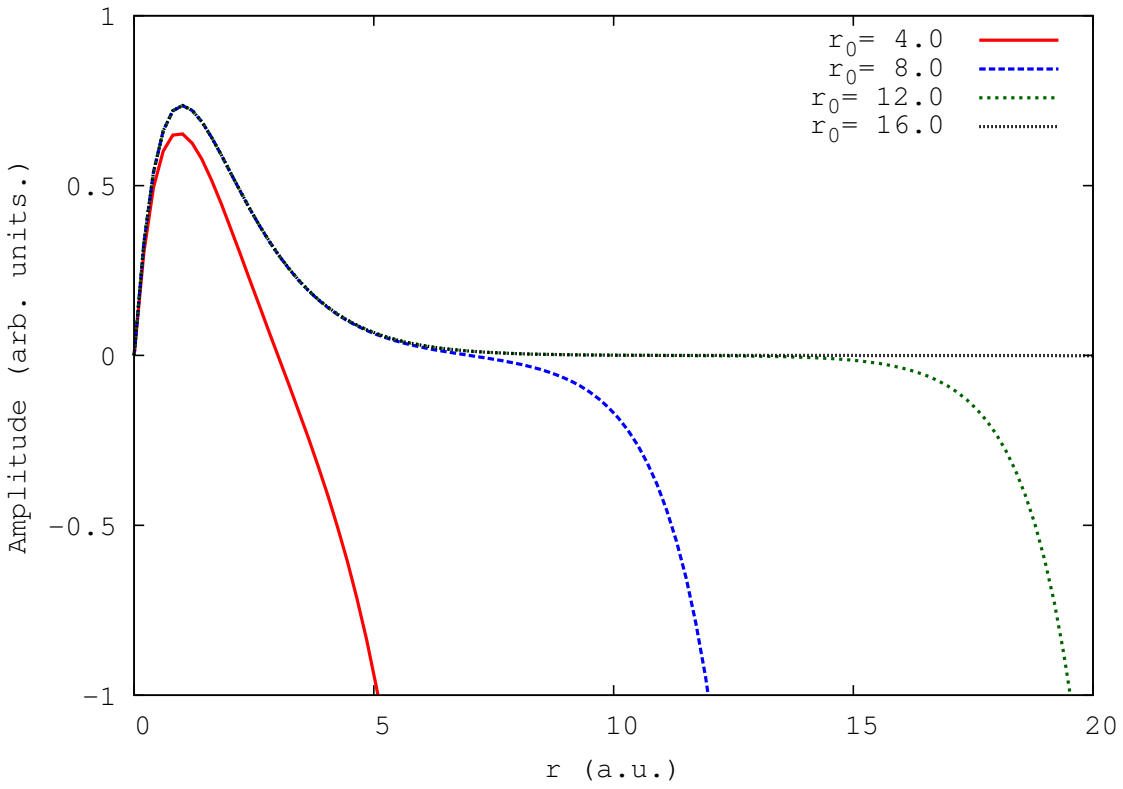

Figure 5.3: The wavefunction (unnormalized) is plotted as a function of the radial distance r for different confinement radii r_0.

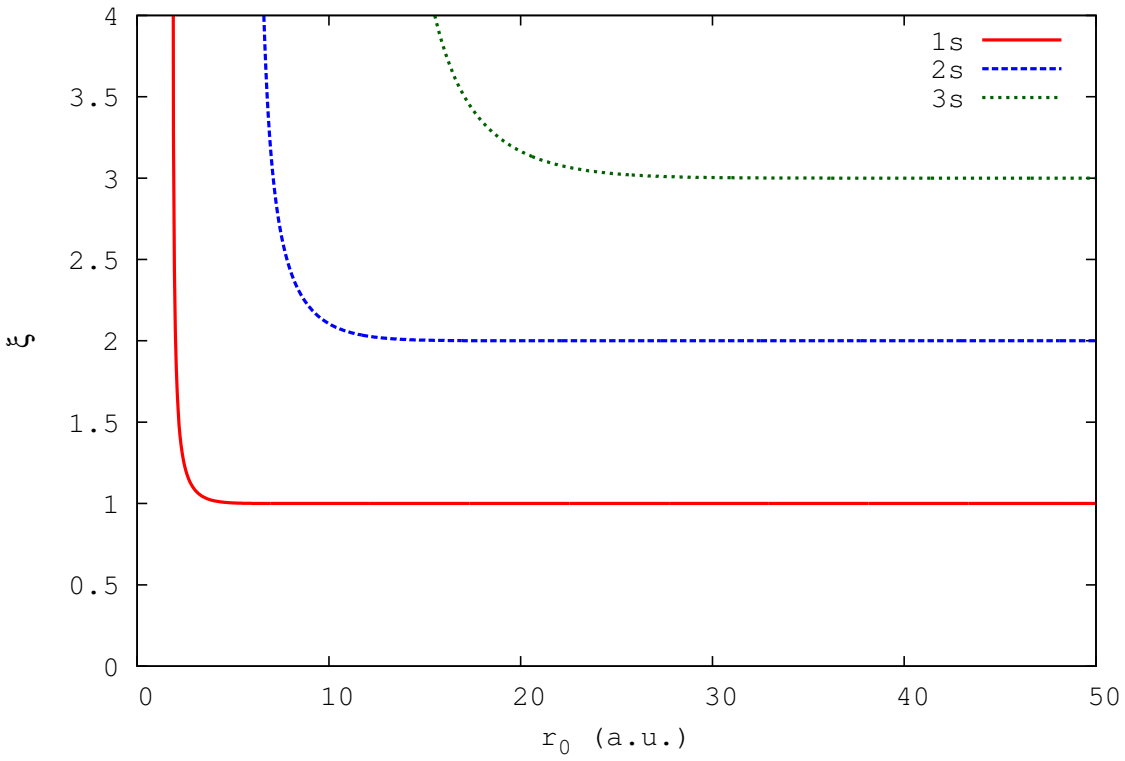

Figure 5.4: The allowed values of ξ are plotted as a function of the confinement radius r_0 for the first s states. The values can be seen to rapidly converge to the respective integer values of n.

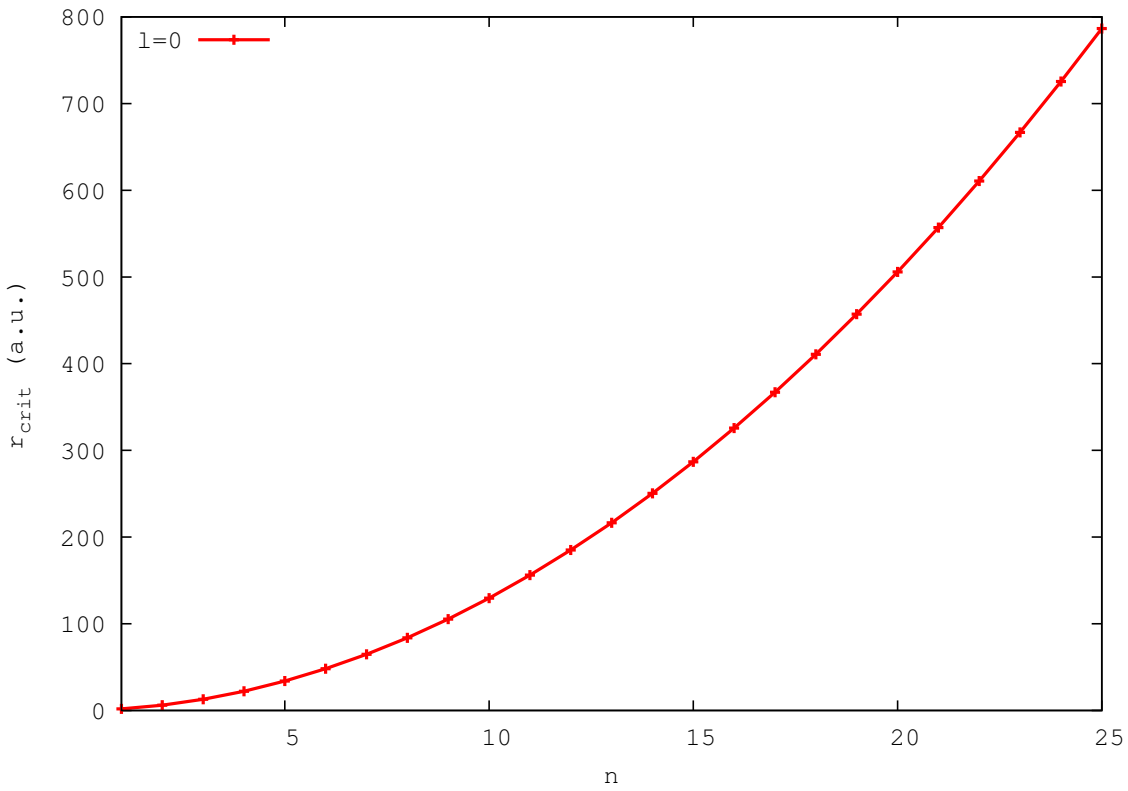

Figure 5.5: The critical radius, calculated from Eq. (5.26), is plotted as a function of quantum number n for the case of l=0.

a smaller r_{crit} because the wavefunction is less extended and therefore less affected by the wall. We could therefore interpret the critical radius as a measure of the ease to make the energy positive.

For the case of $r_0 = 500$ a.u. the highest allowed bound state has $n = 19$, which will be strongly affected by the confinement. We therefore selected $n = 14$ as our most energetic bound state. For example, the free atom state with quantum numbers n=14 and l=0 becomes shifted and now $\xi \approx 14.00099869$, slightly above the unconfined value of 14, which gives an energy shift in the order of 10^{-7} a.u. The change in energy due to the wall was shown to be small, but this by its own does not suffice to guarantee the approximation is good since the wavefunction must have the right shape. The $n = 14, l = 0$ wavefunction is shown in Fig. 5.6 for different r_0. With the confining radius at $r_0 = 500$ the deviation from the asymptotic unconfined value only appears in the last 50 a.u. before reaching the edge of

n	l=0	l=1	l=2
1	1.8352	-	-
2	6.1523	5.0883	-
3	12.9374	11.9097	9.6174
4	22.1901	21.1744	19.0301
5	33.9102	32.9001	30.8119
6	48.0977	47.0907	45.0307
7	64.7527	63.7475	61.7038
8	83.8750	82.8710	80.8379
9	105.4648	104.4616	102.4354

Table 5.5: Critical radii, in atomic units, for different quantum numbers n and l. The values are calculated from Eq.(5.26)

the box. The degree of disparity between the $r_0 = 500$ and unconfined wavefunctions can be further evaluated by projecting one onto the other:

$$P = 1 - \left|\langle \psi_{confined} | \psi_{unconfined} \rangle\right|^2, \tag{5.27}$$

which gives a value of $P \approx 2 * 10^{-4}$. Since this is the worst case scenario we therefore conclude approximating the wavefunctions using unconfined wavefunctions is justified.

The bound states for the time dependent calculations were approximated by employing the states of the unconfined atom, assuming ξ is an integer, therefore neglecting the effect of the confinement. Those eigenstates are available computationally in the GNU Scientific Library. Solving for the exact bound eigenvalues and eigenstates is completely feasible but more complicated and not worth the extra effort for the present work.

The root isolation procedure described previously for positive energies does not work for the negative case because the changes in the wavefunction are very abrupt and extra care must be taken to correctly isolate the roots, so a different algorithm is needed. It is only worth the effort in the case of a small box or to include very high Rydberg states. Also, we expect the effects of the confinement to be noticeable mostly due to the discretized energies

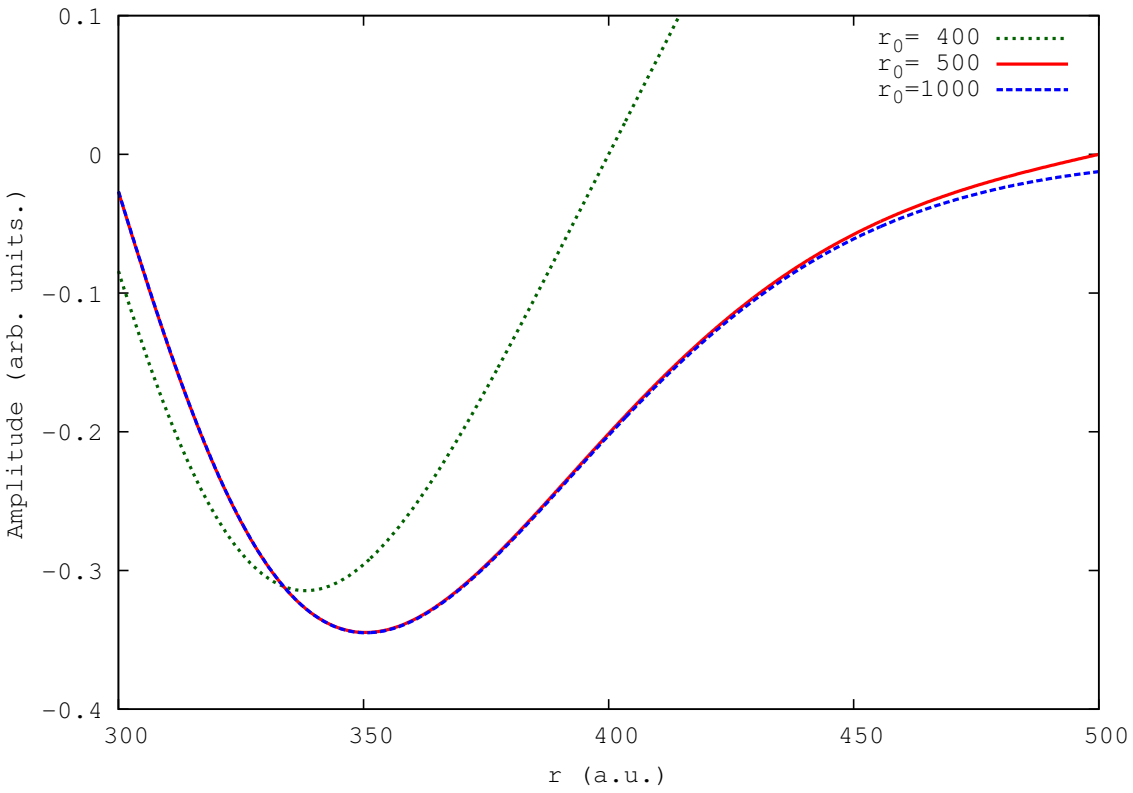

Figure 5.6: The wavefunction for n=14, for different confinement radii, is plotted as a function of the radial distance r. The one with $r_0 = 500$ shows a deviation from the asymptotic value only near the edge of the box.

and their separations, as we will later discuss, rather than small energy deviations. We can see that the obtained positive energies are well separated, so small errors in their values should not make a meaningful difference.

In an unconfined hydrogen atom the potential is of the form $1/r$, which creates the degeneracy between eigenstates with the same n. However, adding the confining potential changes the form of the potential and therefore the eigenstates are no longer degenerate and now have an energy gap. The degeneracy breaking is illustrated in Figs. 5.7 for the negative energy states. The energy gap ΔE is defined as:

$$\Delta E = E_s - E_p, \tag{5.28}$$

where E_s and E_p are the energies of adjacent s and p orbitals respectively with the same quantum number n.

The curves in Fig. 5.7 were obtained by setting r_0 to a given value and then solving for the allowed energies E_s and E_p for different orbitals with $n = 1,2,3$. The vertical lines indicate the critical radii r_{crit} given by Eq. (5.26). One can observe that the gap rapidly disappears as the box gets larger as one would expect, becoming degenerate when $r_0 \to \infty$. Also, for a fixed radius the gap tends to increase with the quantum number n.

The unbound states also show differences in energy caused by the confinement. The allowed energies tend to be similar for different values of l. The energy gap, defined in Eq. (5.26), is plotted in Fig. 5.8 for different state numbers for various confinement radii. Here we notice that the gap tends to get larger for higher states. For any given state the gap diminishes as r_0 gets larger, as expected. The confinement clearly has a much larger effect for these states than for the bound ones. The energy gaps vary with the confining radius, so for high energy states the gaps could become significant. These gaps are associated to possible electronic transitions, requiring the lowest energy. For this approximation to be sufficient the gaps must be small enough to resemble a continuum.

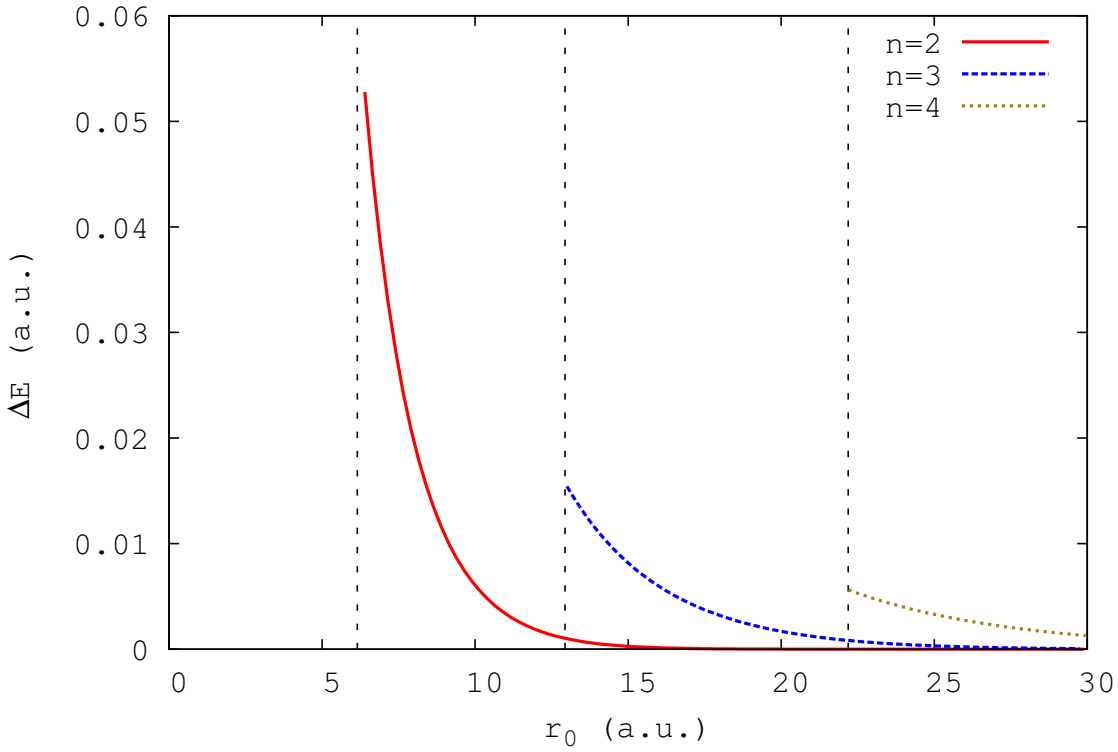

Figure 5.7: The difference in energy, ΔE, between bound states with $l = 0$ and $l = 1$ that have the same quantum number n is plotted as a function of confinement radius r_0 for different values of n. This shift in energy represents the degeneracy breaking which can be seen to tend to zero as the confinement radius increases. The vertical lines represent critical values of r, given by Eq. (5.26).

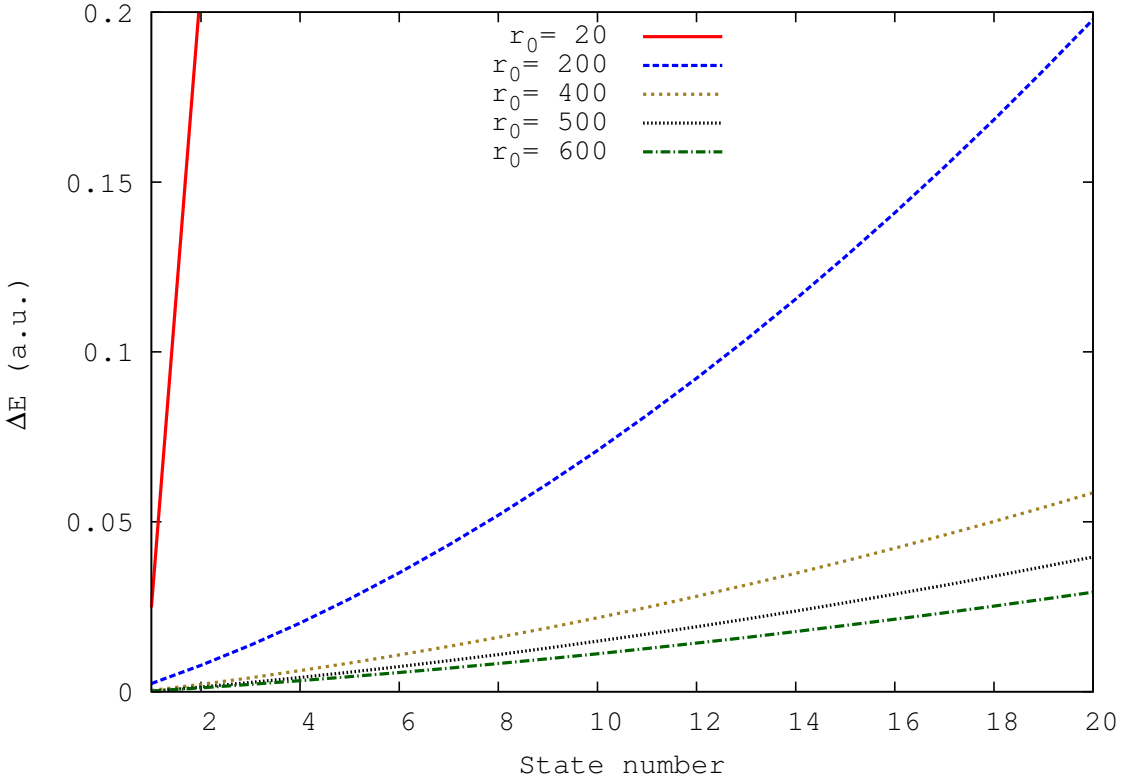

Figure 5.8: The difference in energy, ΔE, between adjacent unbound states with $l = 0$ and $l = 1$ is plotted as a function of the state number, for different confinement radii r_0. This shift in energy represents the degeneracy breaking between levels with different angular momenta.

5.3.3 Dipole matrix elements

We calculate the dipole matrix elements numerically by representing the wavefunctions, bound and unbound, on a radial grid that starts from the origin and ends up to at the maximum allowed radius r_0. The matrix elements that involve bound states are the hardest to calculate using numerical integration because the wavefunctions decay rapidly, requiring a sufficient number of grid points near the origin to get an accurate result.

It is important to consider the convergence of the calculation, with special attention to the dipole moments, which converge slower than the energies. A grid with 70 000 points was first employed for the calculation. Additionally, the results were compared to a calculation done with a finer grid with $1/10$ spacing of the original one to ensure good convergence. The difference in the dipole moments with both grid spacings is around 1% in the worst case, which suggests that they are well converged. A sample calculation for the dipole matrix element corresponding to the 1s-2p transition is shown in Table 5.6 for different grid sizes. All the wavefunctions, bound and unbound, used in matrix element calculation were obtained using the GNU Scientific Library (GSL) functions previously mentioned, using double precision.

For the case of an unconfined atom the matrix elements that involve only bound states can be calculated by the use of existing tables [155, 192] and explicit formulas [185]. A comparison of these to our numerical calculations was done to further confirm good accuracy.

For a basis with a size on the order of 1000 the matrix element calculation can be done in a simple workstation within a several minutes. The big computational bottleneck comes from the time propagation scheme, further described, which can take many hours for the mentioned basis size.

One way to measure the accuracy of the basis and matrix elements is by using oscillator strengths, which are defined as [1]:

N_{grid}	$\langle \psi_{1s} \vert z \vert \psi_{2p} \rangle$
100	2.79537481679193e+00
500	7.65064612516399e-01
1000	7.46399333555785e-01
2000	7.45031163455074e-01
5000	7.44938017607888e-01
10000	7.44935694182621e-01
50000	7.44935539276126e-01
70000	7.44935539092446e-01
100000	7.44935539043323e-01
200000	7.44935539028773e-01
700000	7.44935539027823e-01
1000000	7.44935539027792e-01
"Exact"	7.44935539027803e-01

Table 5.6: The dipole matrix element corresponding to the 1s-2p transition is calculated using different grids ranging from 0 to $r_0 = 500$ a.u. with N_{grid} gridpoints. This is arguably the most important dipole moment for the present work. The "exact"value was obtained computationally by using the explicit formula from Ref. [185], and it is limited only by numerical accuracy.

$$f_{kn} = \frac{2m}{\hbar^2}(E_k - E_n)\left|\langle\psi_n|z|\psi_k\rangle\right|^2, \tag{5.29}$$

where E_k and E_n are the energies corresponding to states ψ_k and ψ_n. The Thomas-Reiche-Kuhn sum rule then states that [1]:

$$\sum_k f_{kn} = 1. \tag{5.30}$$

The sum rule includes all the states, bound and unbound, so it can be considered a measure of completeness of the basis. We can split this sum into bound and unbound states as follows:

$$\sum f_{bound} + \sum f_{unbound} = 1. \tag{5.31}$$

For an unconfined hydrogen atom the sum of the oscillator strengths corresponding to transitions from the ground state to the continuum is equal to $\sum f_{unbound} = 0.4350$ [155]. The value of $\sum f_{unbound}$ was calculated in the present work for different values of r_0, shown in Fig. 5.9. The values for $r_0 = 400$ and $r_0 = 500$ are very close to that of the unconfined atom, although slightly above. This can be anticipated because the confinement is expected to produce an increase in the number of unbound states while eliminating some bound ones. One can observe that for $r_0 = 20$ the final value is higher and reached quite rapidly with a few states, in contrast to the others which require several hundred before settling down.

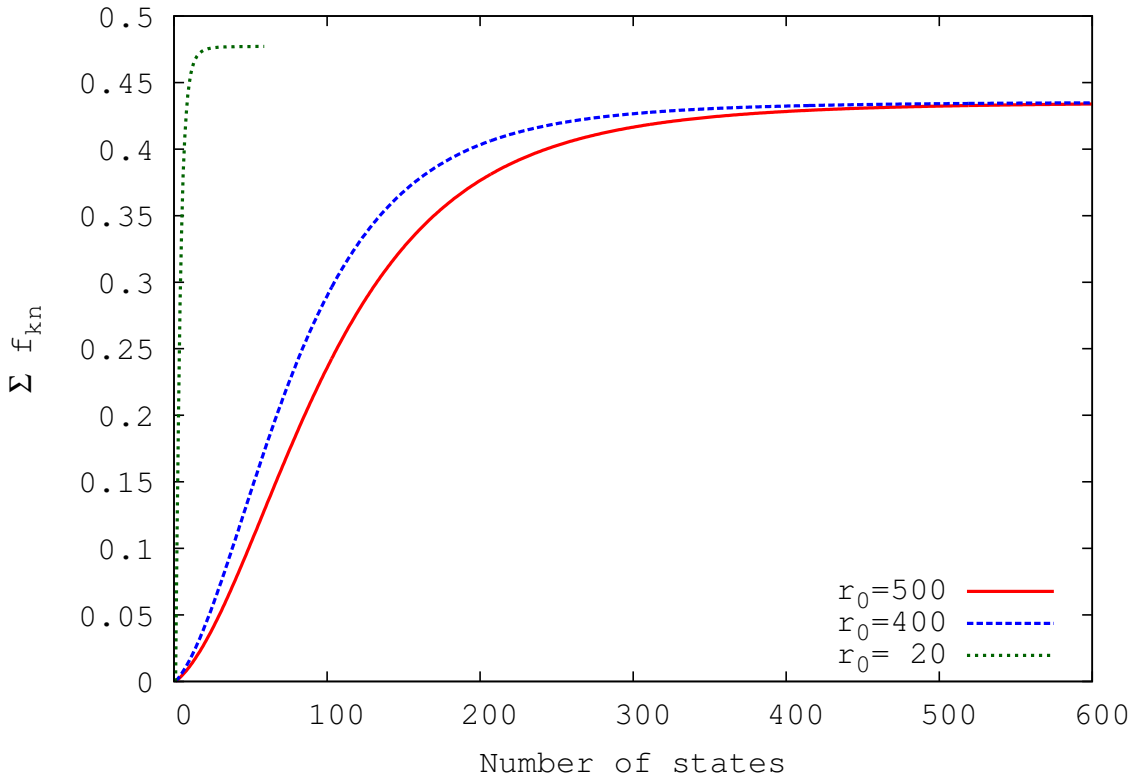

Figure 5.9: The value of $\sum f_{unbound}$, for transitions from the ground state into the positive energy states, is plotted as a function of the number of states in the basis. One can observe that for a smaller box the convergence is much faster. For larger boxes it converges slightly above the known unconfined value 0.4350 [155].

5.4 Time dependent methods

For a time dependent electric field it is necessary to solve the time-dependent Schrödinger equation:

$$i\hbar\frac{\partial|\psi(t)\rangle}{\partial t} = \hat{H}|\psi(t)\rangle, \tag{5.32}$$

which can be solved by using the time propagator [1]:

$$U(t,t') = \exp\left(-iS^{-1}H(t-t')/\hbar\right). \tag{5.33}$$

The S^{-1} in Eq.(5.33) is the inverse of the overlap matrix, which will become the identity matrix for an orthogonal basis.

The time propagator operator will map the wavefunction from its state at time t' to the one at t [1]:

$$\psi(t) = U(t,t')\psi(t'). \tag{5.34}$$

Let t_1, t_2 and t_3 be three time instants. Then the following property exists for the time propagator[1]:

$$U(t_1,t_3) = U(t_2,t_3)U(t_1,t_2) \tag{5.35}$$

This property is important because it allows to break the calculation into multiple time steps $\Delta t = t_{n+1} - t_n$, which can be discrete if one ensures they are small enough. In that case one may apply the operator consecutively for a determined number of time steps in order to propagate a dynamic system.

By inserting Eq.(2.12) into (5.32) and allowing the basis coefficients to take on a time-dependence $c_i(t)$ the following solution for the time-dependent state is obtained:

$$c(t) = \exp\left[\frac{-iS^{-1}}{\hbar}H(t)\Delta t\right]c(0). \tag{5.36}$$

The operator can be approximated by using the Crank-Nicholson method, in which it becomes [1]:

$$\exp\left[\frac{-iS^{-1}}{\hbar}H(t)\Delta t\right] \approx \left(I + \frac{i\Delta t S^{-1}}{2\hbar}H(t)\right)^{-1}\left(I - \frac{i\Delta t S^{-1}}{2\hbar}H(t)\right). \tag{5.37}$$

Unlike the commonly used Taylor expansion method [1], this approximation keeps the propagator operator being unitary, thus allowing the use of relatively larger time steps and longer simulation times while maintaining accuracy.

The HHG spectrum is calculated from the Fourier transform of the dipole moment $d(t)$:

$$\tilde{d}(\omega) = \frac{1}{\tau}\int_0^\tau d(t)W(t)e^{-i\omega t}dt, \tag{5.38}$$

where $W(t)$ is a window function. The window functions can take different shapes, and some of the most common ones are depicted in Fig. 5.10. These window functions will diminish the weight of the values of the signal at the endpoints, making it smoother, while enhancing the weight near the center of the pulse for the Fourier Transform [193]. Some windows, such as the Blackman begin and end at zero, while others such as the Gaussian just reduce the signal to a small value.

We approximate Eq.(5.38) by means of the Fast Fourier Transform (FFT), using a Blackman Window [194], which can be used to ensure the signal is smooth at the endpoints. The length of the window was increased by one extra point to force the resulting signal to be fully periodic [195].

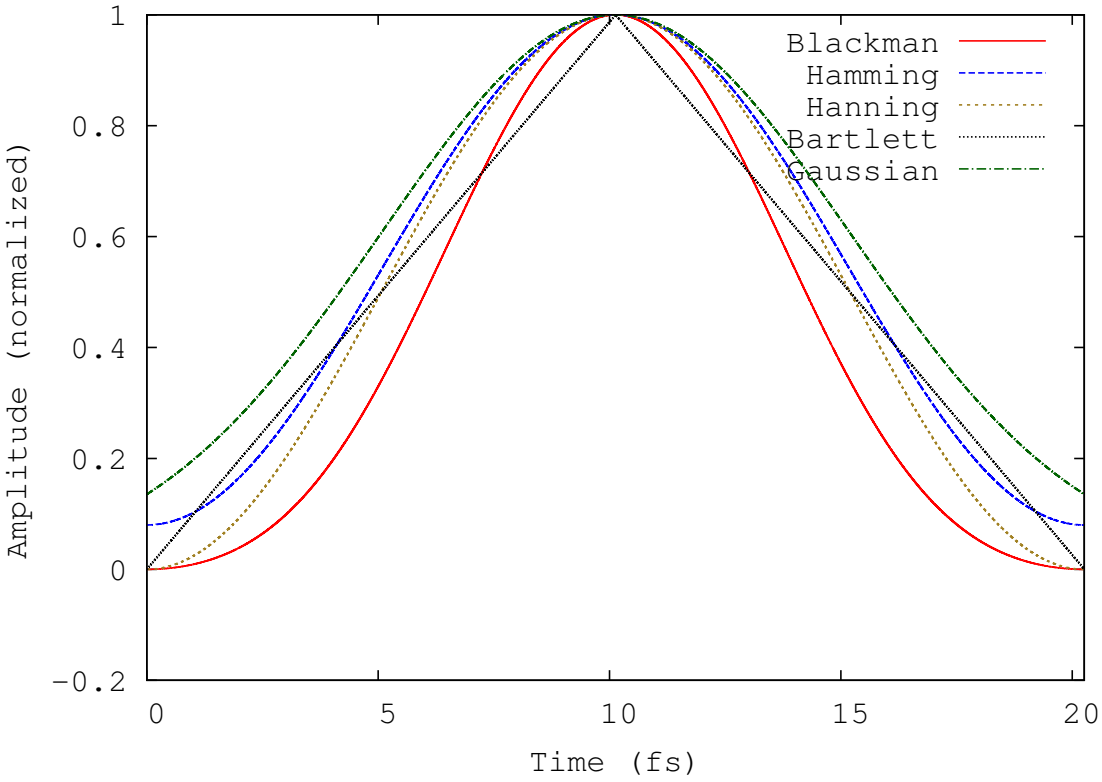

Figure 5.10: Different window functions are plotted as a function of time.

5.4.1 Methods for simulating ionization

One of the limitations of the basis representation is that there is an infinite number of allowed unbound states and it is necessary to truncate leaving only a finite number of them in the Hamiltonian matrix.

The problem is that absorption cannot happen for the highest reachable energy states because there are no higher levels available for the transitions to take place. That means that only stimulated emission is possible from those levels, and this can lead to unphysical features in the spectrum, such as background noise [196]. To prevent this the population of the highest energy states must be kept low during the course of the simulation.

Also, in order to correctly approximate the photo-ionization of an unconfined atom it is necessary to avoid reflections from the boundaries of the box. In the present work we use two methods to address these issues: the heuristic lifetime method [197] and the complex absorbing potential (CAP) [198], both described below.

Heuristic lifetime

The heuristic lifetime method is not as popular as the CAP, but it has received some more attention recently [196, 197, 199–202]. The method assigns each energy level a finite lifetime by adding an imaginary term to each energy E_n, as shown in Eq.(5.39).

$$E_n \rightarrow E_n - i\Gamma_n. \tag{5.39}$$

The value of Γ_n is set using the following criteria:

$$\Gamma_n \equiv \begin{cases} 0 & , \quad E_n < 0 \\ \sqrt{2E_n}/d_n & , \quad E_n > 0 \end{cases} \tag{5.40}$$

In Eq.(5.40) Γ represents the inverse lifetime of the state, while d_n represents the distance the electron with energy E_n would travel classically during the lifetime of the state.

Therefore adjusting the value of d_n to a small value would make the population of the corresponding state disappear faster than for a large d_n.

It is important to set up an appropriate value for d_n. If d_n is too short then ionization could be overestimated; if too long then the highest energy states can become too populated and cause artifacts on the signal, so a compromise is needed.

For simulating HHG most works had the value d_n set to a constant value d for all energies. However, a very recent work [202] employed a two different values of d as follows:

$$d_n \equiv \begin{cases} d & , \quad E_n < E_{cut} \\ d_{cut} & , \quad E_n \geq E_{cut} \end{cases} \tag{5.41}$$

One of the values of d_n in Eq.(5.41) is for the energies that are between the ionization threshold and the classical cutoff energy, (given by Eq.(5.7)), and a smaller one for energies above the cutoff. Such approach gives a better balance and was shown to give results with better agreement with previous grid-based calculations [202].

Complex Absorbing Potential (CAP)

A typical solution to simulate ionizing systems is to place an imaginary potential near the boundaries such that it will absorb any electron wavepackets that are a certain distance away from the atom.

This method has the advantage of not disturbing localized high energy wavepackets near the center. A typical problem that can arise from a CAP is having unphysical reflections or transmissions [198], but these can be diminished with proper choice of parameters.

The method is commonly used for spacial grid-based simulations [1]. However for an eigenstate representation it can have its complications (See for example Ref. [203]). One of the issues that can arise is that the matrix elements of the CAP may not be easy to calculate because the integrals are not always analytically solvable for the needed basis.

A CAP could potentially affect all the states, bound and unbound, meaning that Rydberg states would be absorbed due to their long tails despite them being bound. This problem can be avoided by using a *projector corrected CAP* [203], which can be made to only affect the unbound states.

The addition of a CAP to the Hamiltonian means that the eigenvalues of the Hamiltonian Eq.(5.13) become complex. If any of the new eigenvalues has a positive imaginary part this can cause instability giving completely nonphysical results, so caution must be taken.

The CAP matrix elements were calculated numerically by the same method described in 5.3.3. In the present work the stability issues were avoided by forcing all the CAP matrix elements that involve a bound state to become zero. We only allow the unbound states to be affected by the CAP and check the complex eigenvalues to ensure full stability.

The form of the CAP employed is:

$$V_{CAP}(r) = \begin{cases} ar^4 & , \quad r_{CAP} < r < r_0 \\ 0 & , \quad \text{otherwise} \end{cases} \tag{5.42}$$

More details on this particular shape can be found in Ref. [198].

The heuristic lifetime method has multiple advantages over the CAP such a the simplicity of implementation, it can be used regardless of the type of basis employed or the details of the system, and it guarantees the system will remain stable under all conditions.

A drawback is that it does not have a definite spatial region of action and it will therefore absorb highly localized high energy electron wavepackets regardless of their location, whereas the CAP would not affect such a wavepacket until it approaches the boundaries.

5.5 Results

5.5.1 HHG for long wavelength lasers

The Stochastically enhanced Kaufmann basis was used to simulate HHG using an 800 nm laser, which is typically studied in the literature by different methods [158, 204, 205]. We compare our results to the pseudo-spectral approach in Ref.[204], which employs a complex absorbing potential. The importance of this calculation is showing the capabilities of the employed basis to simulate the ionization of the atom in strong field conditions

The electric field is given by the equation:

$$\varepsilon(t) = \varepsilon_{max} \sin^2(\pi t/\tau) \sin(\omega_0 t), \tag{5.43}$$

where ε_{max} is the maximum amplitude of the electric field, ω_0 the driving angular frequency, and τ is the duration of the simulation. The values for each of the parameters are later specified individually for each simulation.

Extra care is taken to ensure that τ is an integer multiple of the laser period, to minimize the zeroth frequency component of the electric field, as well as optimizing the time steps to ensure that the fundamental frequency and its harmonics have an exact representation (within numerical accuracy) in the discretized Fourier space. If the Fourier space does not have a vector with the exact frequency of the signal then the representation requires a linear combination of many vectors, leading to a broadening of the peaks. If instead the exact frequencies exists in Fourier space then the signal is orthogonal to all but a few of the vectors, leading to a sparse representation and therefore narrow peaks [193]. Therefore, by selecting suitable parameters the accuracy of the representation in frequency space can be enhanced without having to alter the signal. The discrete Fourier Space was made to contain each of the harmonics ($\omega = \omega_0, 2\omega_0, 3\omega_0 ...$) within numerical accuracy. The effect of these careful parameter selections can be seen in the spectra of the laser in Fig. 5.11, where the background noise is many orders of magnitude smaller than the signal.

Parameter	Value	Units
Total simulation time	53.370 2206.4 20	fs au cycles
Time step	0.000533 0.022064 0.000200	fs au cycles
Cutoff energy	1.111 30.23 19.50	au eV photons
Ponderomotive energy	0.193 5.243	au eV
Quiver amplitude	15.41	au
Excursion amplitude	30.82	au
Classical kinetic energy	0.385 10.486	au eV
Ionization energy	0.5000000 13.605698 8.7789852	au eV photons
Laser energy	0.056954191 1.549	au eV
Laser wavelength	800.000 15117.8	nm au
Laser period	2.669 110.3	fs au
Pulse peak intensity	0.05 8.77E+13	au W/cm^2
Pulse duration (τ)	20	cycles
Keldysh parameter	1.13	(none)

Table 5.7: Simulation parameters for the long wavelength laser

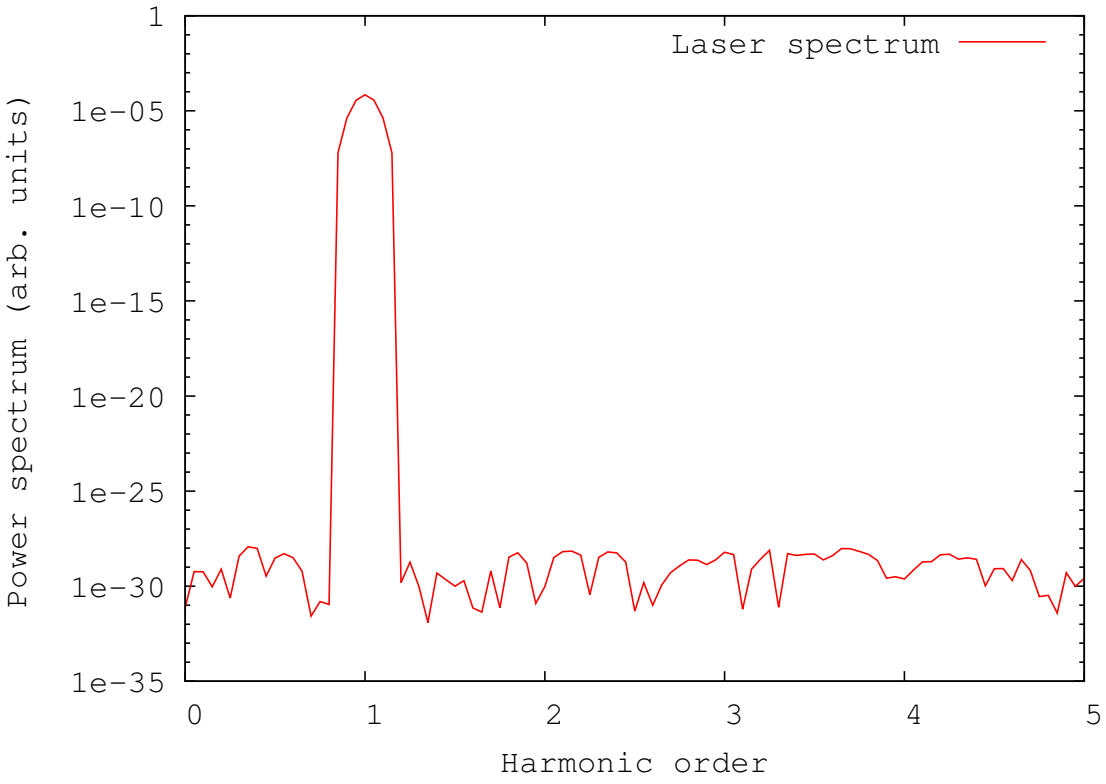

Figure 5.11: The Fourier Transform of the electric field (plotted in 5.12), using the Blackman window is plotted as a function of the harmonic order. The laser parameters are given in detail in Table 5.7. One can observe that the employed laser pulse has a very narrow bandwidth, with practically no DC component, as a consequence of the careful parameter selection.

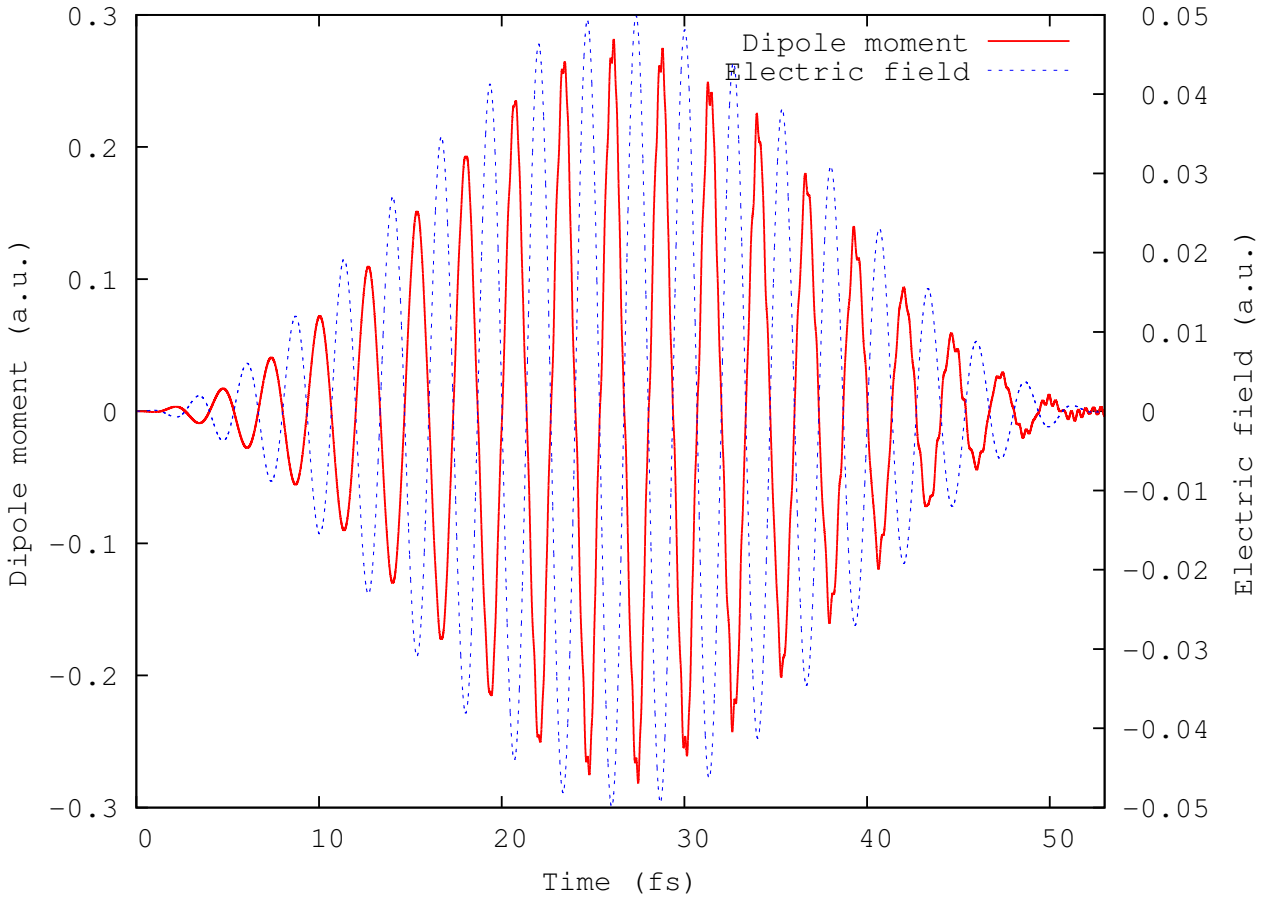

Figure 5.12: The dipole moment $\langle\psi(t)|z|\psi(t)\rangle$, and electric field are plotted as a function of time. The laser wavelength is 800 nm and other details are given in Table 5.7. The dipole moment, which was obtained using the Stochastically enhanced Kaufmann basis, can be seen to oscillate with a very similar shape as the driving laser, although some distortions are visible near the envelope maximum and towards the end.

One of the challenges is to determine suitable parameters d for the Heuristic lifetime method previously described. The typical way is to use the *3-step model* classical electron oscillation amplitude as a guideline to set up the distance d. In the following calculations we use two different values of d_n, as in Eq.(5.41). The one below cutoff, d, is specified for each case while $d_{cut} = 0.1$, unless otherwise specified.

As a first example the value of d is set to 25. The other parameters are given in Table 5.7. The obtained expectation value of dipole moment, $\langle\psi|z|\psi\rangle$, as a function of time is plotted in Fig. 5.11 together with the electric field. The dipole moment shown tries to follow the shape of the laser pulse and also tend to approach zero as the laser pulse decays. However some deviations from the laser shape are visible near the extrema and the endpoints which can be attributed to nonlinear behavior of the system. The distortion if affected by the value of d, so other values are also investigated.

In Figure 5.13 we show the harmonic spectrum for different values of d, as well as the results obtained by Si-Lang et.al.[204] by means of a pseudo-spectral method. The amplitudes were normalized using the amplitude of the fundamental harmonic of each run as a reference. The results show good agreement for the lowest harmonics, which have similar amplitudes, with some differences on the sides of each harmonic. The results from Si-Lang et.al. are noisier in general, with some smaller structures in between peaks which can be attributed in part to the transformation window [193], final values of the dipole moment as the laser envelope decays [193], discretization of the Fourier space and the excitation of Rydberg states [184].

For the 15th harmonic and beyond the pseudo-spectral method tends to give lower values than the ones predicted by our approach. Past the cutoff the amplitudes tend to decay, and the differences between the values of d become more apparent, with larger values yielding a higher amplitude of the signal.

The present method gives a much lower background noise, by several orders of magnitude. This noise can have multiple causes, one of them being the accuracy of the repre-

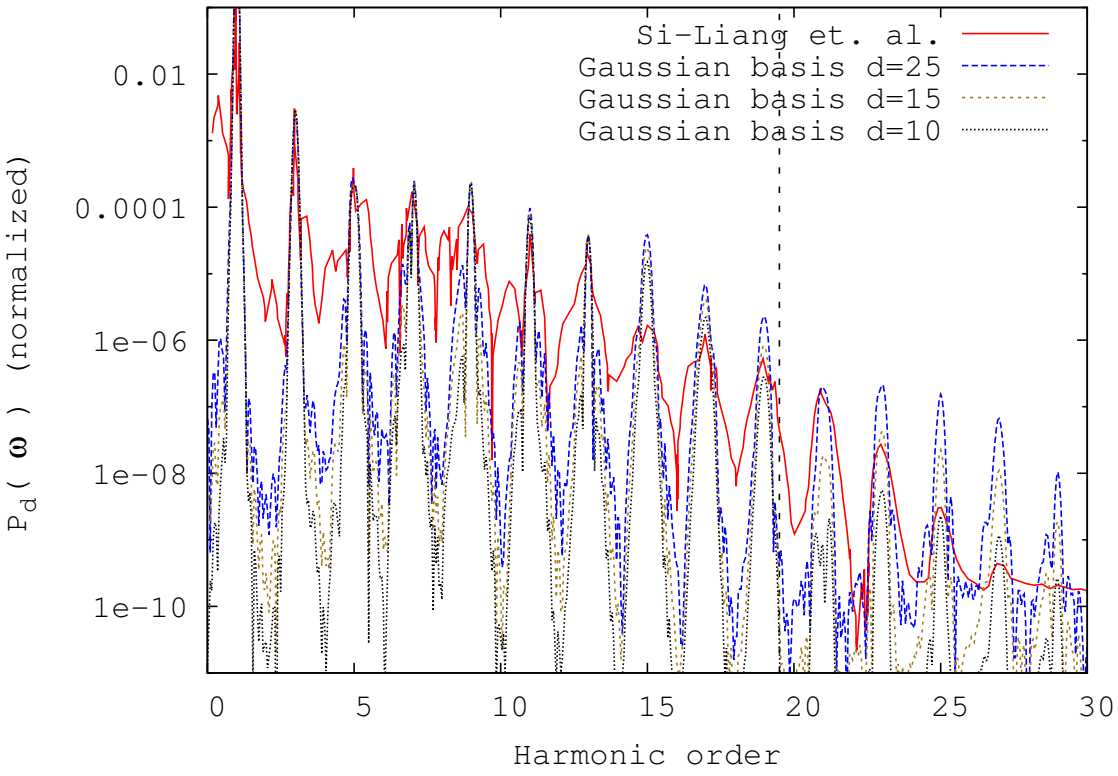

Figure 5.13: We show the HHG spectrum for different values of the heuristic lifetime parameter d of the present work, as well as the results obtained by by Si-Lang et.al. by means of a pseudo-spectral method [204]. The results are normalized to the peak amplitude of the fundamental harmonic. The cutoff frequency is marked by a vertical dashed line. The maximum laser amplitude is $\varepsilon_{max} = 0.05\ a.u.$ and wavelength $\lambda = 800nm$. The other simulation parameters can be found in Table 5.7.

sentation of Rydberg states, whose transitions can persist even in the absence of the laser. For the given conditions the pseudo-spectral method probably has better representation of the Rydberg states in the vicinity of the atom ($r \leq 100$ a.u.) and therefore presents higher background levels than the present method, and therefore a faster decay. On the other hand, the pseudo-spectral method has more structures between peaks (especially among the 7th and 9th harmonic) that indicate the signal has less periodicity than the one with the present method.

5.5.2 Mollow sidebands

We first built a 2-level model of the hydrogen atom, formed by the 1s and the 2p level, with their exact energy and dipole moment which are analytically known [155]. We also construct a 3-level model by adding the 2s state to the 2-level model.

For the Mollow sideband generation we set ω_0 equal to the transition frequency between the 1s and 2p state ($\omega_0 = 0.375$ a.u.). Time dependent simulations were done using four different models for the atom: 2-level, 3-level, Gaussian (Stochastically enhanced Kaufmann basis) and Confined hydrogen. The laser parameters are given in Table 5.8 and are the same for all models. The Heuristic lifetime method is used to create absorption in the case of the Gaussian and Confined hydrogen basis.

Important details can be observed in the expectation value of the dipole moment. As an example we show the $\langle \psi(t)|z|\psi(t)\rangle$, as a function of time, and the driving electric field in Fig. 5.14 (obtained with a confined hydrogen). The first important feature is that the dipole moment shows beats, which is a sign of sideband generations taking place. Secondly, it is important to notice that the oscillations persists even after the laser pulse has decayed entirely, which has a high significance for the current investigation.

The Fourier Transform of the laser pulse, using a Blackman window, is shown in Fig. 5.15. It is here that one can see the bandwidth of the laser is very small, with a practically inexistent amplitude for higher harmonics. The bandwidth of the laser is kept small to

Parameter	Value	Units
Total simulation time	20.264 837.76 50	fs au cycles
Time step	0.00041 0.01676 0.00100	fs au cycles
Cutoff energy	0.557 15.15 1.48	au eV photons
Ponderomotive energy	0.017956 0.489	au eV
Quiver amplitude	0.715	au
Excursion amplitude	1.429	au
Classical kinetic energy	0.0359 0.9772	au eV
Ionization energy	0.5000000 13.605698 1.3333333	au eV photons
Laser energy	0.375 10.204	au eV
Laser wavelength	121.50 2296.06	nm au
Laser period	0.405287959 16.75516082	fs au
Pulse peak intensity	0.10 3.54E+14	au W/cm^2
Pulse duration (τ)	50	cycles
Keldysh parameter (γ)	3.73	(none)

Table 5.8: Simulation parameters for the Mollow sideband generation

ensure any obtained sidebands are generated by Rabi flipping and not by the laser itself. The DC component is also maintained at a minimal level (due to the careful selection of parameters for the simulation), which is important to avoid having the Stark effect alter the dynamics of the atom.

The obtained harmonic spectra for all four models are compared in Fig. 5.16. The generation of sidebands on the fundamental harmonic is observed for all models, however the peak structure shows differences depending on the model employed. An important feature

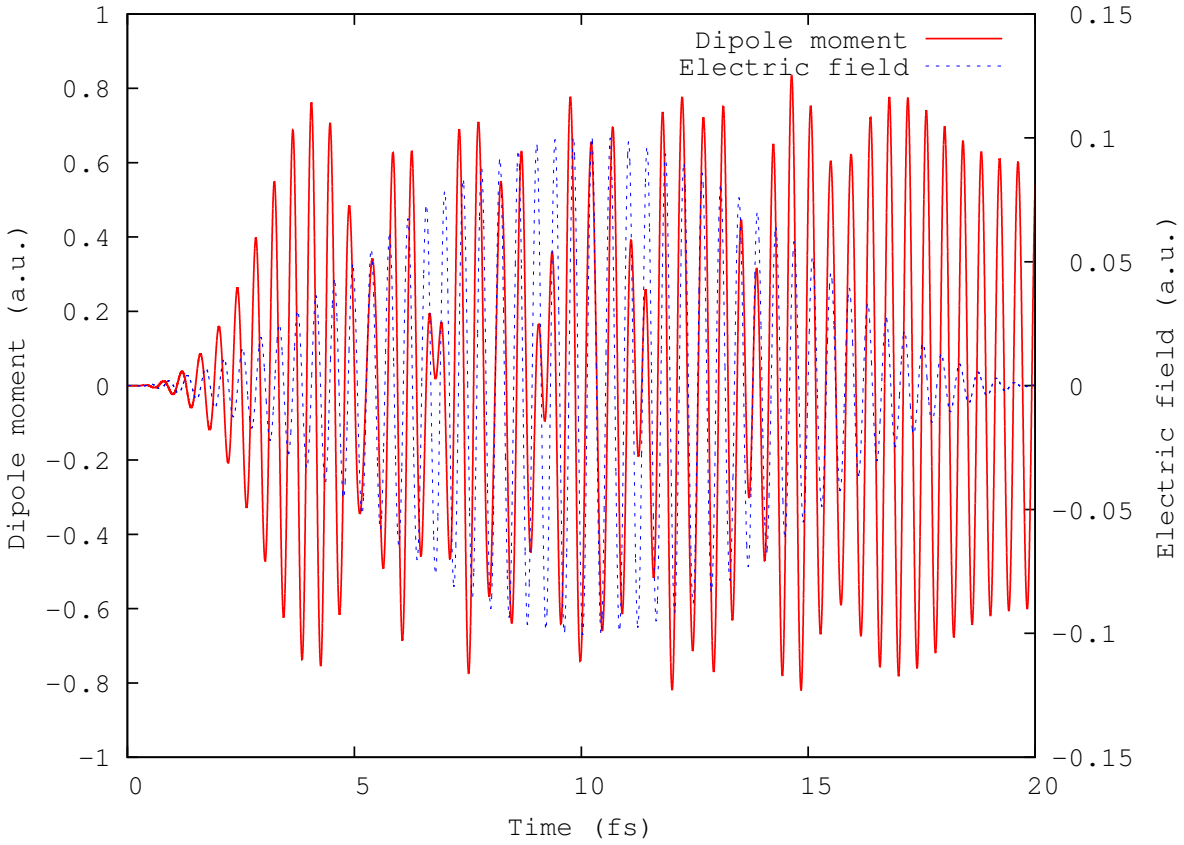

Figure 5.14: The dipole moment (left axis) and electric field (right axis) are plotted as a function of time, using a confined hydrogen model. The laser parameters are given in detail in Table 5.8. The most important features to observe are the beats, produced by Rabi flipping, and the persistence of the dipole moment oscillations after the laser has been turned off.

is that the high harmonics also show a formation of sidebands (with some differences depending on the model of the current work), not just the fundamental. There is no mention of those sidebands in Ref.[166], and it is unclear if they were overlooked or if the formation is beyond the limits of their method.

Two-level and three-level model

In Fig. 5.16 (bottom) one can observe that for the fundamental harmonic, the 2-level and 3-level models give very similar results, but there are big differences for the higher harmonics. One can see that the 2s-2p transition changes the results for the third harmonic

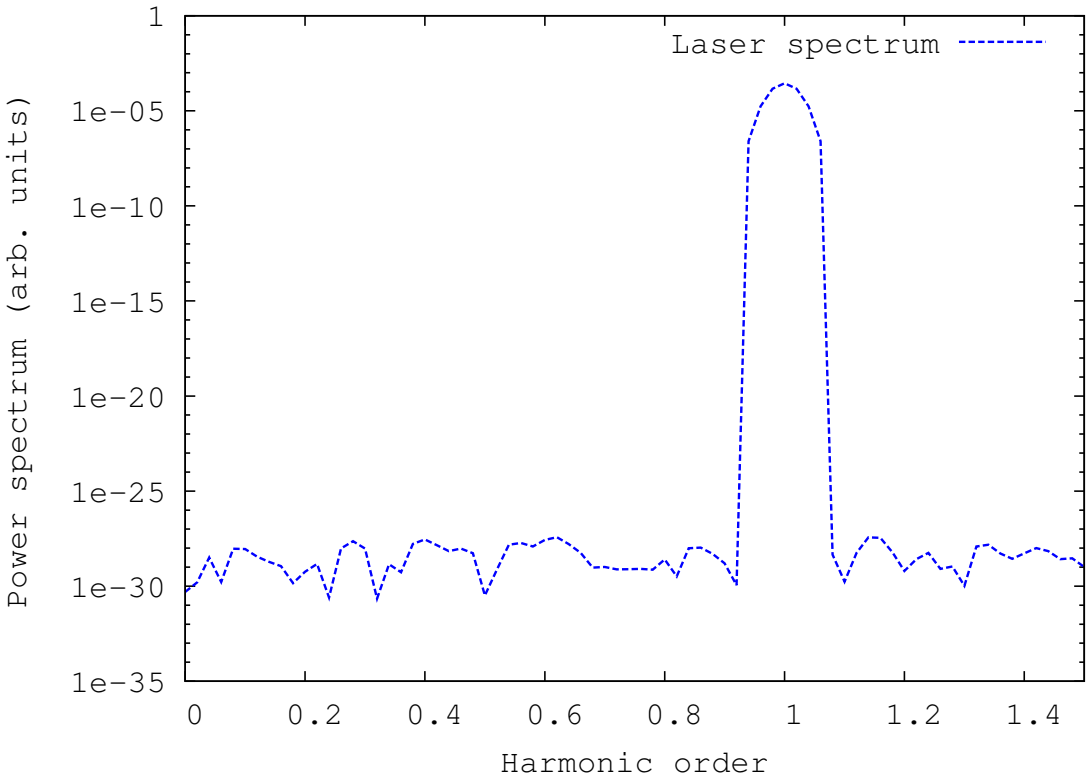

Figure 5.15: The Fourier Transform of the electric field, using the Blackman window is plotted as a function of the harmonic order. The laser parameters are given in detail in Table 5.8. One can observe the bandwidth of the laser is very small, with the DC component being practically inexistent, which is important in order to ensure the sidebands are created solely due to Rabi flipping.

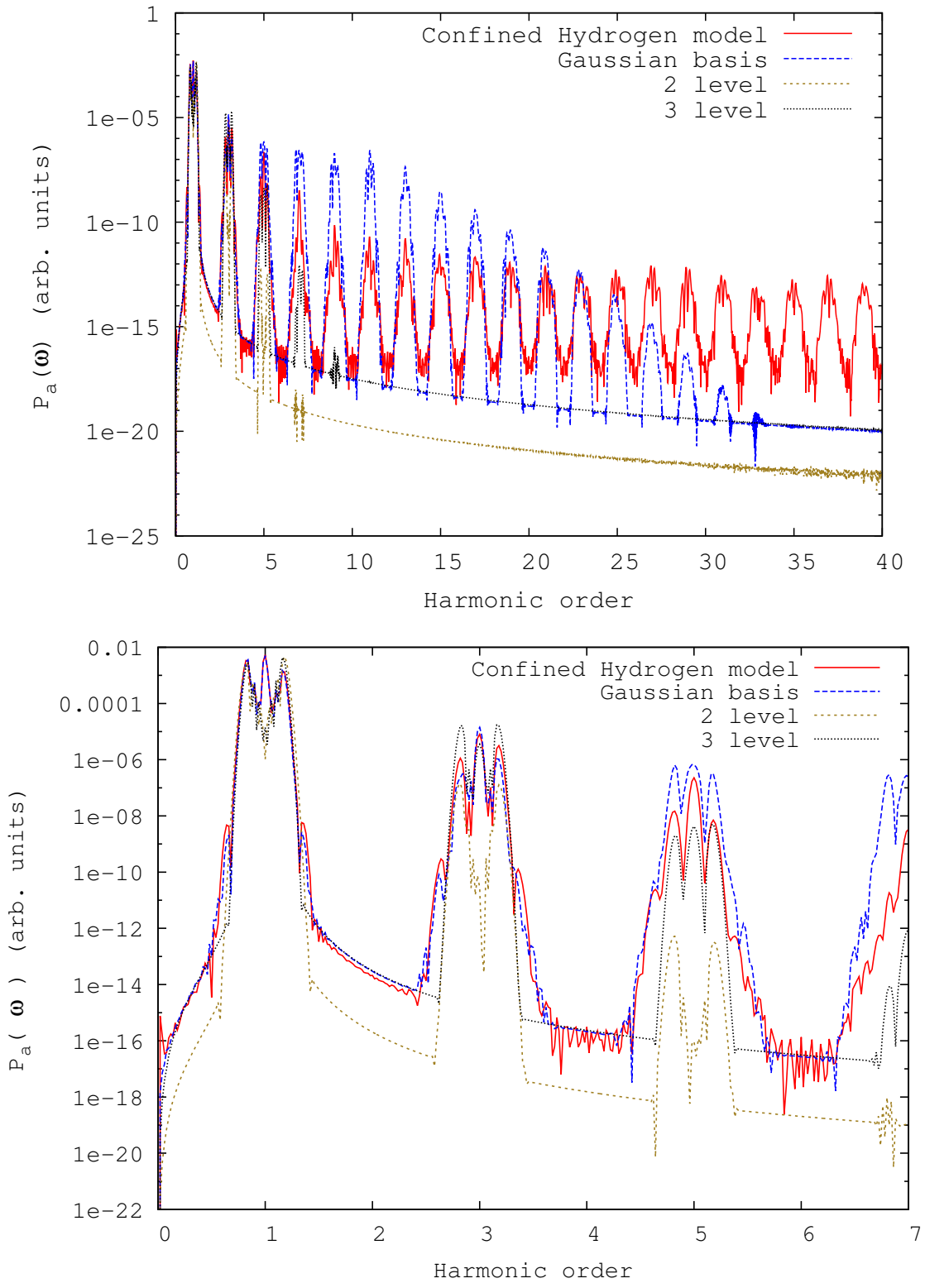

Figure 5.16: (Top) Harmonic spectrum obtained by stimulating atom with an external field with frequency equal to the 1s-2p transition. (Bottom) Shows the same plot but zoomed on the first harmonics. The Heuristic lifetime method is used for absorption. The laser parameters are given in Table 5.8.

and above because the 2-level model predicts a suppression of the harmonic while the other models show a peak. This shows that the 2-level model is therefore completely inapplicable to explain the observed structure on the peaks for the studied case.

The transition between the 2p and 2s state would typically be a forbidden one because there is no energy difference between degenerate levels. No photons are expected to be absorbed or emitted by such transition, giving an oscillator strength of zero. However the dipole moment of this transition is very large [155], and it is responsible for the strong emission lines produced by the fine and hyperfine structure due to the lifting of the degeneracy.

The cause of the 2s-2p transition triggering in this case can only be attributed to the external laser pulse, which brakes the degeneracy of the states. The DC component is practically inexistent, so the Stark effect is not to be the likely cause. We must emphasize that for the confined hydrogen model the bound states are degenerate because the effect of the distant wall was neglected while constructing the basis.

A consequence of this transition being so important is that small perturbations that lift degeneracy and affect the populations of the 2s and 2p levels could potentially alter the harmonic spectrum because of their capability of populating and depleting these states, even with a relatively weak signal.

Both 2-level and 3-level models also show a quick decay in amplitude for high frequencies, and neither of them gives any visible peaks past the 10th harmonic, after which the background signal is dominant.

Multilevel simulation

In this case we employ two different approaches to provide many levels of excitation: a Gaussian basis (a stochastically enhanced Kaufmann basis) and a confined hydrogen atom with the boundary located at $r_0 = 500$. The angular momenta considered ranges from l=0 up to 2, unless otherwise specified. The confined Hydrogen basis contains 39 bound states

and 900 unbound states. The harmonic spectra are also plotted in Fig. 5.16, where one can see differences in the behavior for the highest harmonics (top), and similar results to those of 3-level system for lower harmonics (bottom).

One question that arises is how many angular momentum states are needed to give an accurate description of the system for the given parameters. To help answer this question the calculation was repeated for the confined hydrogen model with a larger basis that has $l_{max} = 3$. The results for this case are plotted in Fig. 5.17. There is a relatively good agreement between the results for the lowest harmonics, the only changes are small differences in amplitude. However, for the seventh harmonic and beyond much larger changes are observed. Since the dipole selection rules only allow $\Delta l = \pm 1$, adding $l = 4$ or higher states is not expected to make any difference on the lower harmonics. We therefore conclude that considering up to $l = 2$ is sufficient for studying the lowest harmonics for the given parameters.

The third harmonic in Fig. 5.16 (bottom) shows a 3-peak structure with sidebands, which are largest for the 3-level model, and smallest for the Gaussian Basis. The energy associated with this peak is 1.125 a.u., which is greater than the ionization energy of hydrogen. This might suggest that the third harmonic sidebands are caused by transitions from the continuum. However, it cannot be the case because the bands are present even for the 2-level and 3-level models, which have no unbound states. It is important to remember that although the field-free eigenstates still form a complete set under strong electric field conditions, they are no longer eigenstates and the energies can be significantly altered.

The generation of high harmonics in a 2-level system, produced by Rabi flipping of bound states, is possible as shown in Refs.[160, 206]. Our model goes beyond the 2-level approximation by including the effects of other transitions. Having higher energy states available for the electron affects the amplitude of the peaks, allowing the apparition of the central 3rd harmonic peak, which is absent in the two-level model in Fig. 5.16.

Multiple window functions were tested out, see Fig. 5.18, to show how these can affect

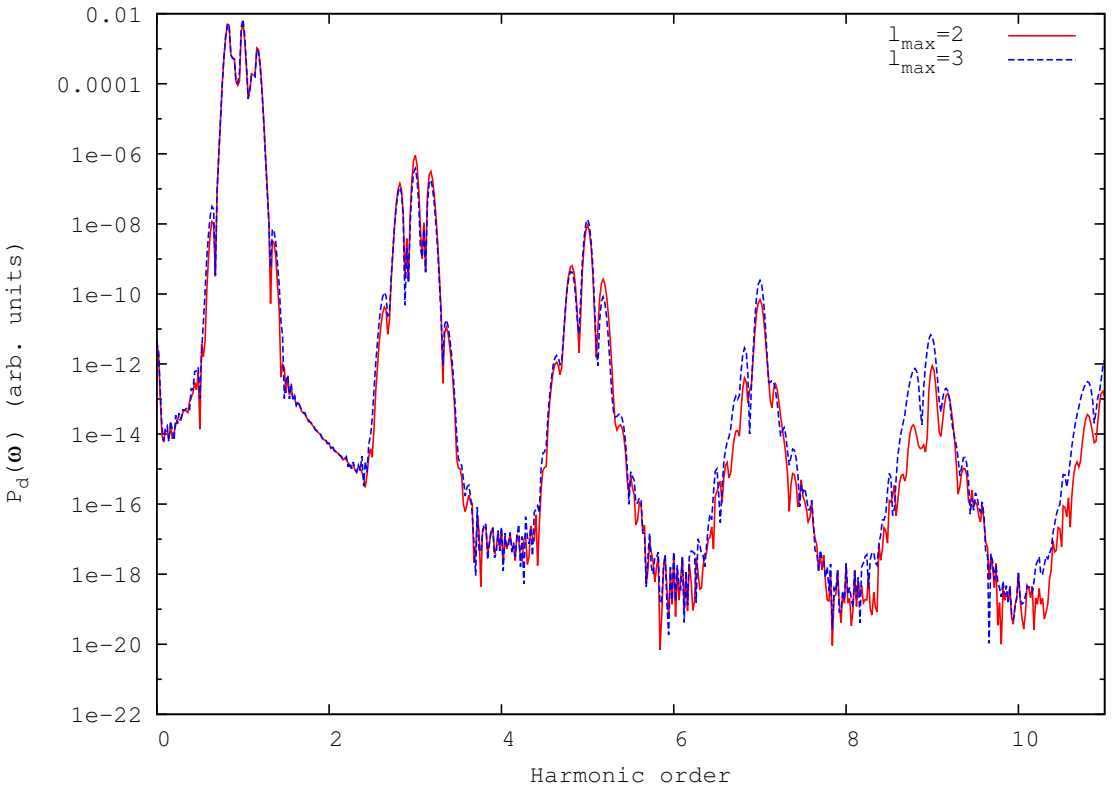

Figure 5.17: The HHG spectrum for the confined hydrogen with a basis with maximum angular momentum $l_{max} = 2$ (same as in Fig.5.16) and an enlarged one with $l_{max} = 3$ are shown. The laser parameters are given in Table 5.8.

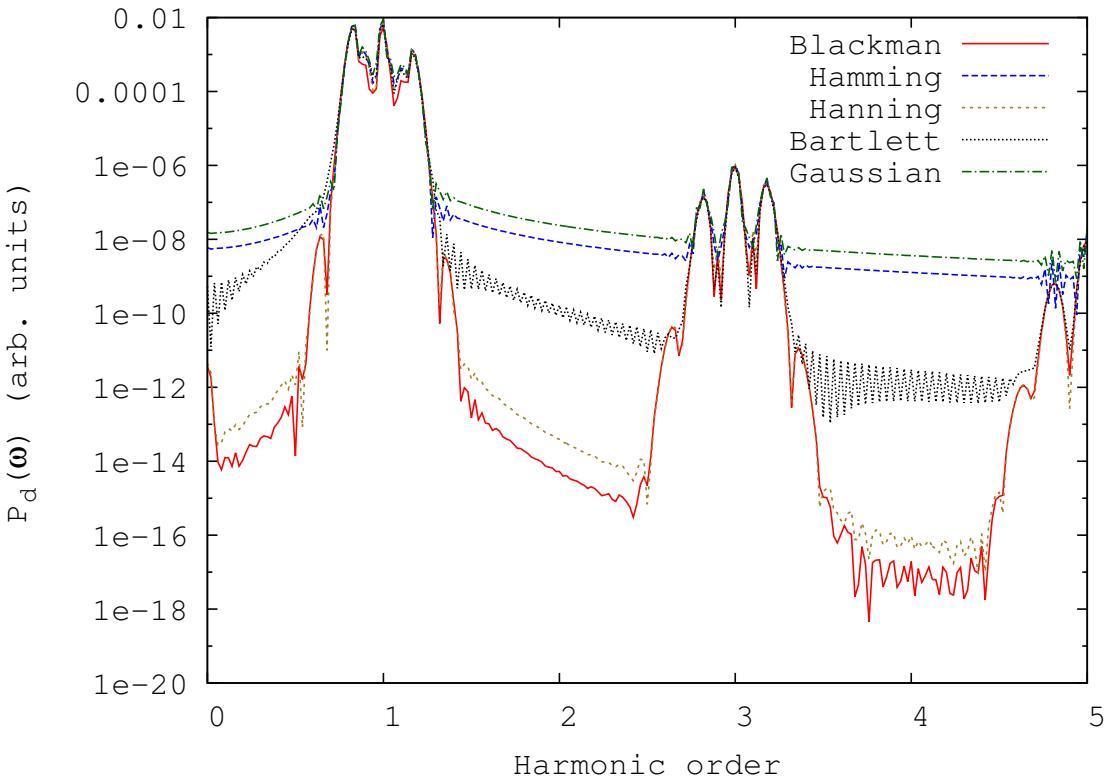

Figure 5.18: The HHG spectrum for the confined hydrogen using different window types is shown. The simulation parameters are given in Table 5.8. The background noise level is clearly more significant for the Gaussian, which can be attributed to its nonzero endpoints, in contrast with the Blackman which starts and ends in zero, giving a much lower level.

the spectra. The background noise level is much higher for the Gaussian window because it does not start or end at zero, unlike the Blackman which does so and gives the lowest background noise. However, the peaks seem to be largely unaffected by the shape of the employed window.

The populations for the 1s, 2s and 2p states are plotted in Figs. 5.19, 5.20, and 5.21 for the 2-level, 3-level and confined hydrogen model respectively. For the 2-level case the typical Rabbi flips can be observed in the 1s and 2p populations. On the other hand the 3-level model shows that during the periods when the 2p state gets highly populated so does the 2s state, and they both get depleted when the 1s state gets repopulated. In the 3-level case, Fig. 5.20, the 2s state population shows almost twice as many peaks as the driving

electric field, which suggests that the transition is becoming enabled every half laser cycle.

The 2-level and 3-level models show a big difference in the final populations, which can be explained by thinking of the 2s state as is it were acting like a retardant for the repopulation of 1s, giving as a result a larger probability for 2p. A similar behavior in the 2s population is observed in the confined hydrogen model, Fig. 5.21, among the 2s and 2p levels but the overall probabilities decrease over time because higher energy states get populated.

In order to further investigate into the 2p-2p transition the 3-level system was studied under different electric field intensities. The average and maximum populations for the 2s state are plotted in Fig. 5.24. It is clear that an increase in the electric field intensity gives a larger population of the 2s state, and for strengths above 0.1 a.u. it can even become momentarily the state with the largest population. The average population increases in a nearly linear fashion with the electric field maximum amplitude. This increase can be attributed to the degeneracy breaking, which is larger for stronger fields.

For a hydrogen atom the transitions that involve an increase in both energy and angular momentum tend to be preferred over those with only one of these quantities increasing and the other one decreasing [155]. The presence of the 2s state allows a downwards transition in angular momentum from the 2p, which has a high dipole moment and enters in a competition with the transitions to 1s and d states. The apparition of an additional pathway therefore alters the spectrum and ionization probabilities. These competitions can be evidenced in Figs. 5.20, and 5.21, giving as a result different final populations. The 1s final population does not vary too much between the confined hydrogen and the 3-level case, but the 2p is much more depleted for the confined hydrogen.

To further illustrate this competition between transitions we made a modified confined hydrogen basis which has the 2s-2p dipole moment matrix element set to zero, and repeated the calculation for the same previous parameters. The obtained populations are shown in Fig. 5.22. The blocking of the transition clearly hinders the ability of the 2s state to popu-

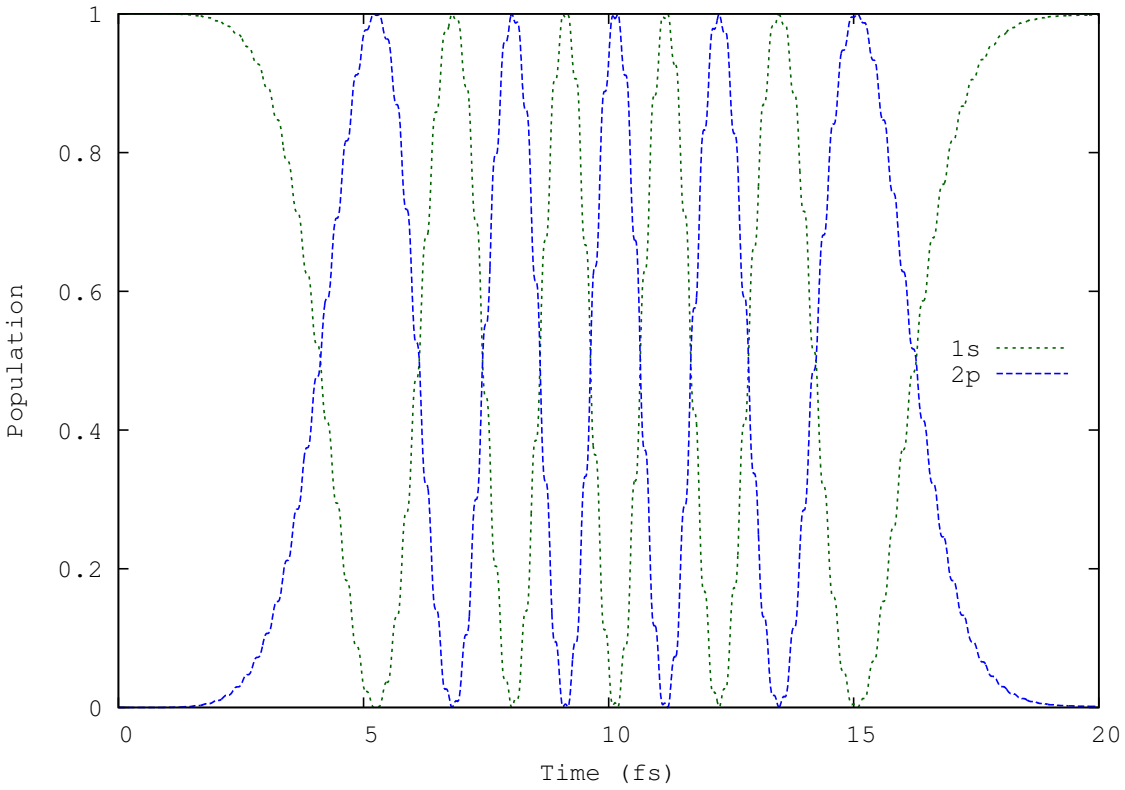

Figure 5.19: The populations of the 1s and 2p states are plotted as a function of time for the 2-level model. The Rabi flipping can be clearly observed in the oscillations of the populations. The simulation parameters are given in Table 5.8.

late. The 2p population curves in Figs. 5.22 and 5.21 are plotted side by side in Fig. 5.23 for ease of comparison. Upon careful inspection one can see that the multiple small valleys in the curve descend to very low levels with the transition enabled, but with no longer descend as deep in the blocked case. The final populations of the p state are also different and the peaks are shifted towards earlier times when the transition is blocked. In the present case the existence of the 2s-2p transition diminished the probability of ionization.

The employed electric field is very intense, so ionization cannot be neglected. The ionization probability is plotted in Fig.5.25. The ionization values obtained in the present work are near 50%, while Ref. [166] obtained near 40% using a pseudo-spectral method.

The exact value of the ionization probability can vary depending on the Heuristic lifetime parameters employed, so further investigation was done. The calculation was repeated

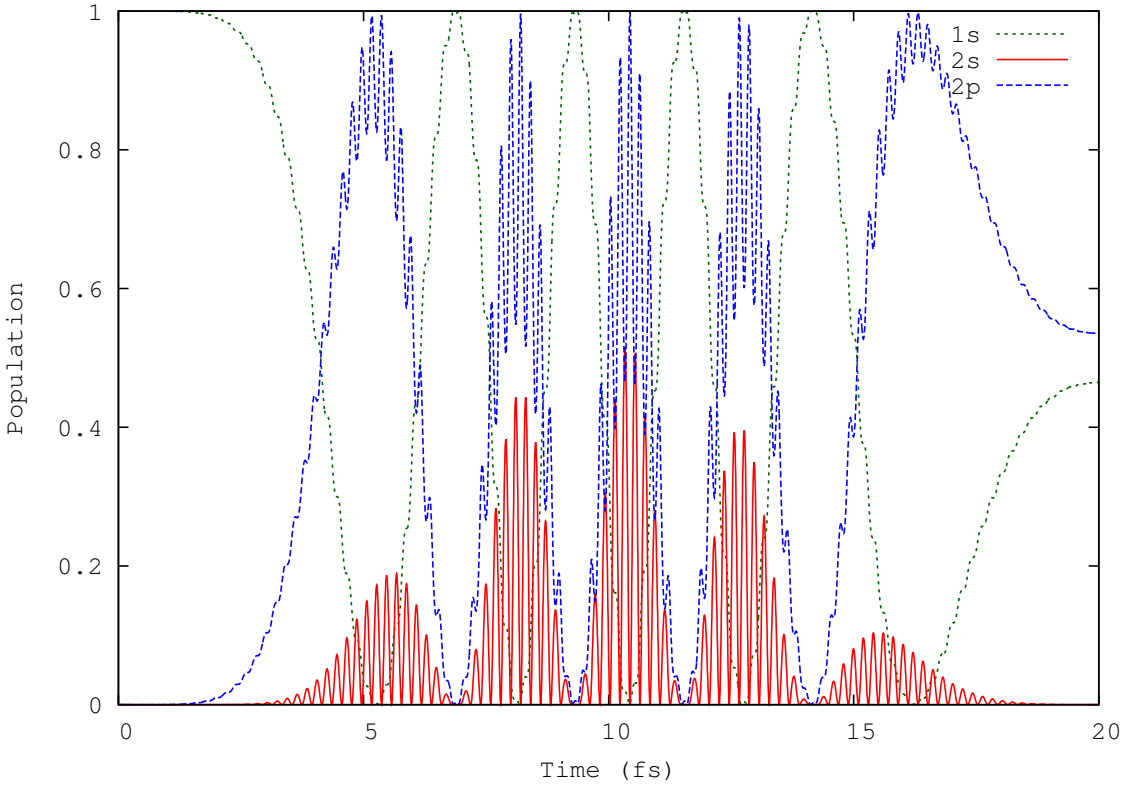

Figure 5.20: The populations of the 1s, 2s and 2p states are plotted as a function of time for the 3-level model. The simulation parameters are given in Table 5.8. One can observe that the 2s state populates due to the 2s-2p transition, which would be typically forbidden because the levels have the same energy in the absence of the laser. It is important to notice that the 2s state populates whenever the 2p does too, and both deplete almost completely.

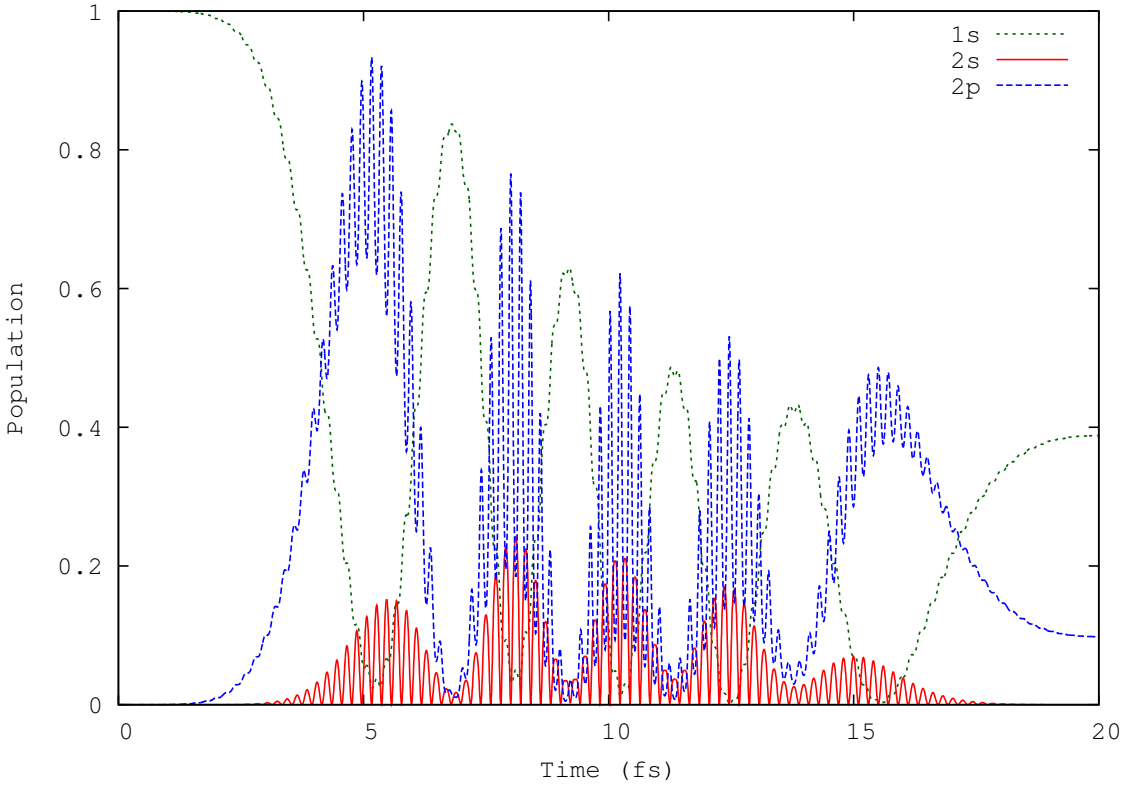

Figure 5.21: The populations of the 1s, 2s and 2p states are plotted as a function of time for the confined hydrogen model. The simulation parameters are given in Table 5.8. One can observe the 2s state populates together with the 2p, and although the populations tend to decay the oscillations persist. The final population differs from the 3-level system due to excitation of higher orbitals and competitions between the transitions.

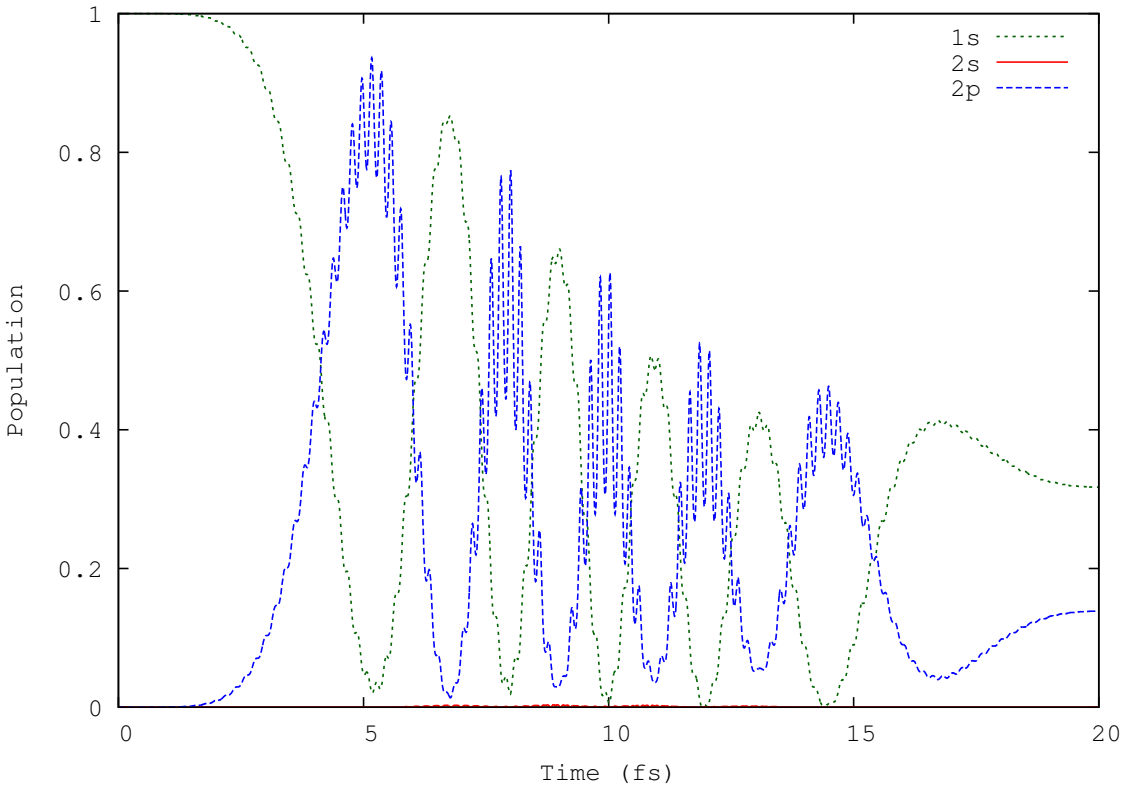

Figure 5.22: Populations for a modified confined hydrogen basis, with the 2s-2p dipole matrix element set to zero. All other settings are identical to the ones used in Fig. 5.21. One can see that the 2s state remains mostly unpopulated.

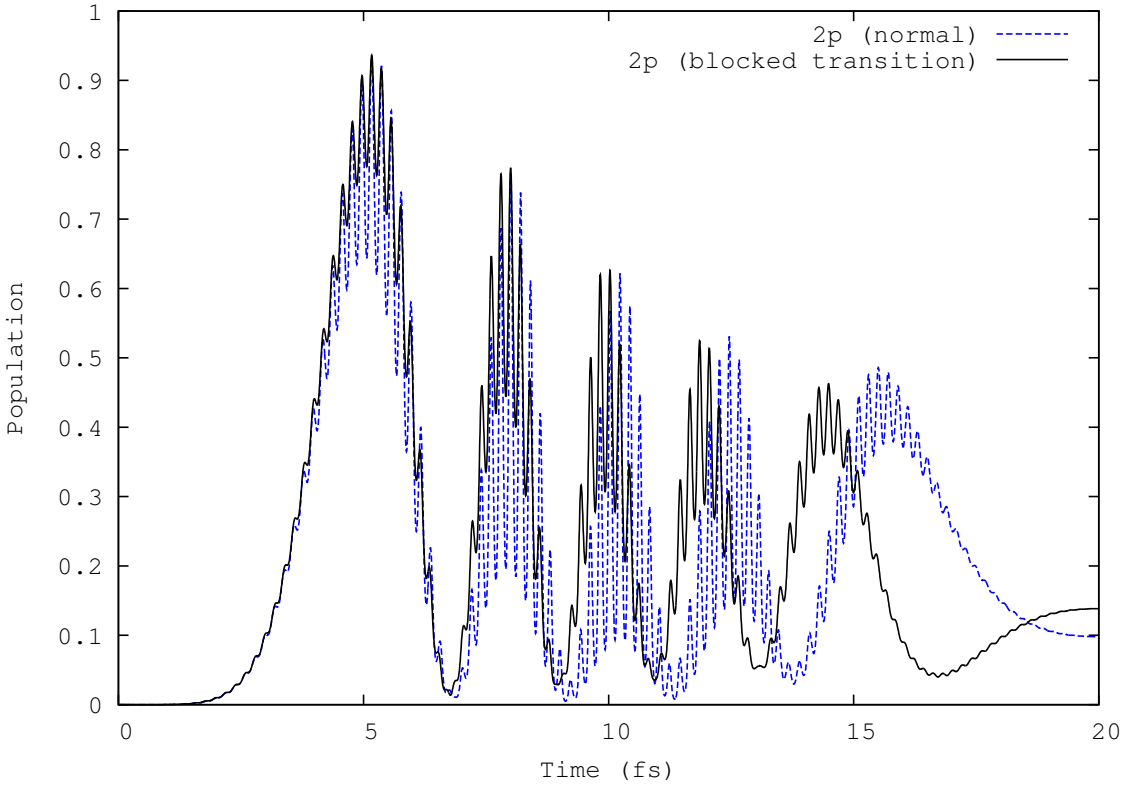

Figure 5.23: Comparison of the populations for the 2p from the modified confined hydrogen basis, and the unaltered curve from Fig. 5.21. One can see that the final population levels are different and the envelope maxima are time shifted due to the inability of the electron to undergo a 2s-2p transition. This blockade also makes the atom more likely to ionize.

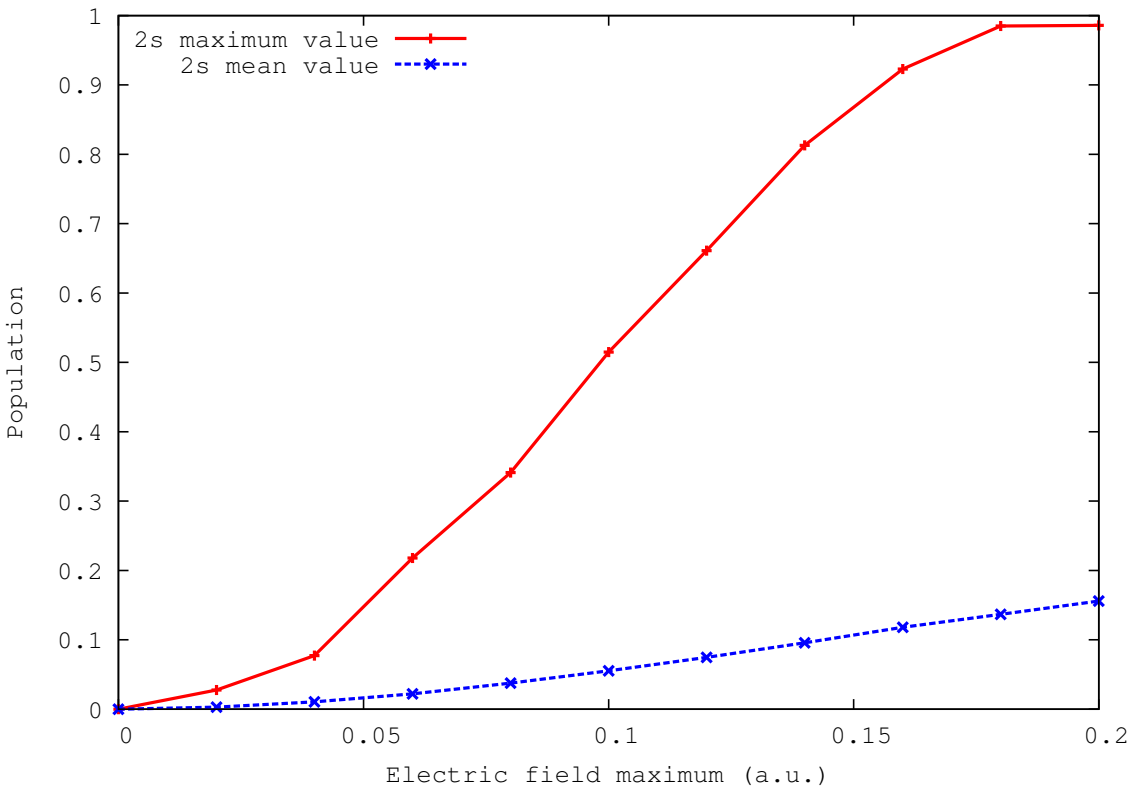

Figure 5.24: The average and maximum populations of the 2s state is shown plotted as a function the maximum electric field intensity. A clear increase in population is observed for larger fields and it even become the most populated state in some cases.

with different values of d, for the Gaussian basis, with different electric field intensities. These results are shown in 5.26, together with the results of Zhang et. al. [166]. Their value is close to our calculation for the case of large d (long lifetimes). In summary, the results of our calculations with heuristic lifetimes range about $0-10$ percentage points above those of Zhang et. al. [166].

We additionally did a calculation using the confined hydrogen model and a CAP, defined in Eq.(5.42), and the ionization probability calculated was about 55%. Overall, our results tend to overestimate the ionization rate of Zhang et. al. However, despite all these differences in ionization rates, for all the simulations done in the present work the peak structure persists in the spectra.

We also repeated the calculation for different electric field intensities and observed the shift of the sidelobes respect to the central one, for the fundamental and the third harmonic. The sidebands were analyzed by using a peak detection algorithm, based on the Python *PeakUtils* library. The obtained position of the peaks, upper and lower sidelobes, are plotted as a function of the electric field in Fig.5.27 (top and bottom). The theory predicts a linear dependence between the Rabi flipping and the applied electric field for the fundamental harmonic [166], although deviations can occur. We can observe that the linearity was best obtained for $\varepsilon_{max} \geq 0.12$ a.u. For the third harmonic the splitting also shows to increase monotonously with the laser intensity for both the upper and lower sidebands for higher intensities, while for lower ones the splitting was not observed with the employed laser parameters. Since the variations are smooth, it seems plausible to control the sidebands, and hence the emission, by changing the shape of the laser pulse.

Deviations in the detected positions of the peaks can occur due to several reasons such as: insufficient frequency resolution, laser bandwidth, the window shape employed to calculate the FFT, the signal to noise ratio, and the value of the dipole moment at $t = \tau$. For smaller intensities the sidebands can be very hard to distinguish since it would require good frequency resolution and therefore a very long pulse. However, for higher intensities the

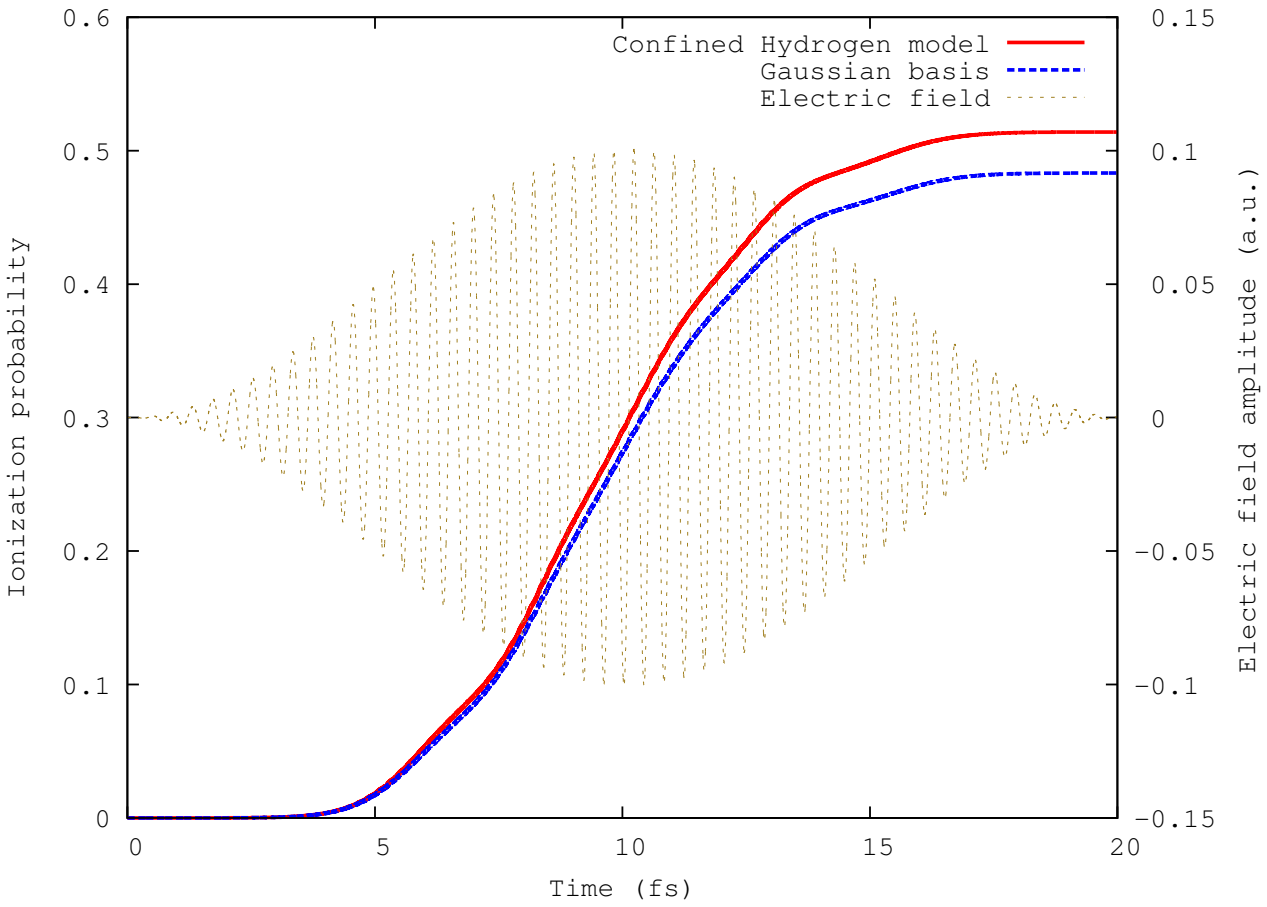

Figure 5.25: The Ionization probability is plotted as a function of time, together with the electric field. The laser parameters are given in Table 5.8. One can observe both the Gaussian basis and confined hydrogen yield similar results in this case.

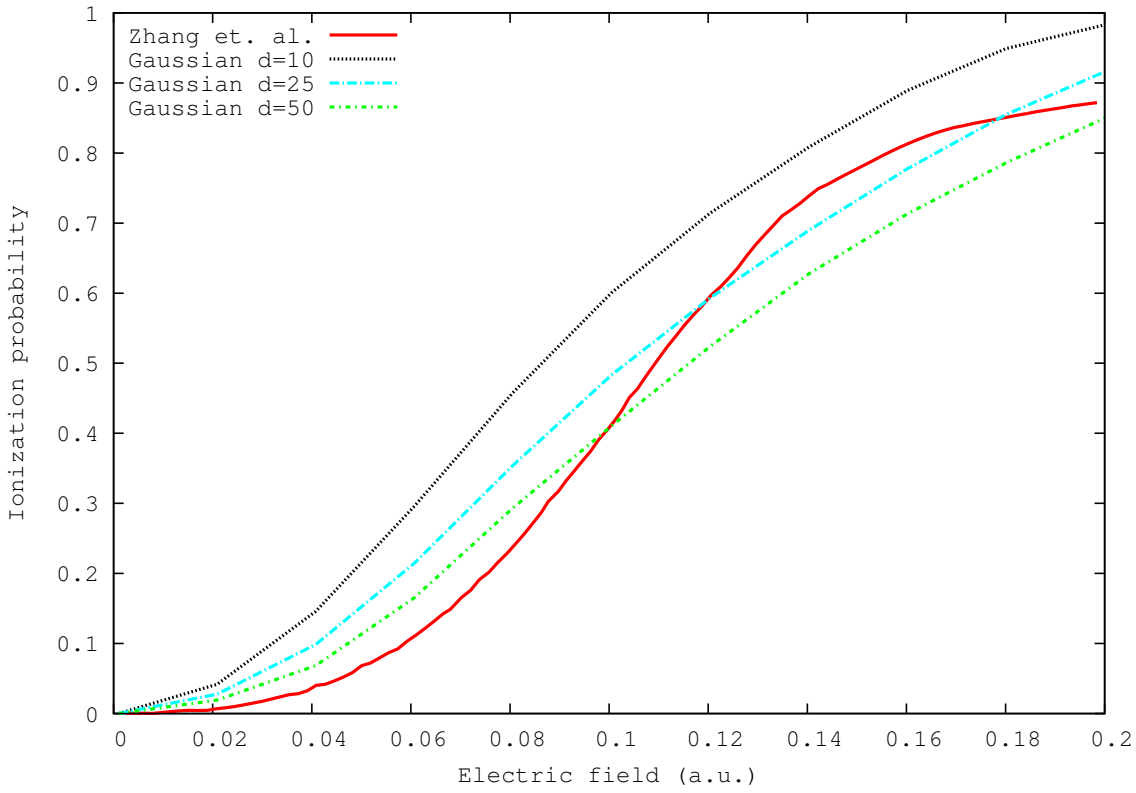

Figure 5.26: The Ionization probability is plotted as a function of the maximum electric field amplitudes for different heuristic lifetime parameters. The value of the distance parameter d,defined in Eq.(5.40), is shown for every curve. We also included the results obtained by Zhang et. al. from Ref.[166]. The laser parameters are those in Table 5.8, with the exception of the electric field maximum amplitude, as well as the quantities that depend on it.

ionization becomes significant and a long pulse would be undesirable in such case. The final value of the dipole moment when the laser is turned off can also affect the sidelobes due to the apparition of artifacts, such as an increase in background noise in the spectrum [193]. Since the Rabi flipping is a consequence of the intensity, each simulation will have a different flipping rate. It is possible to tailor each laser pulse duration such that it is turned off when the absorption is near saturation to compensate for this artifact, but it comes at the cost of making the conditions for different field strengths unequal. Nevertheless the trend observed is clear in Fig.5.27(top and bottom) .

Further studies into the effects of the pulse shape might be able to provide ways to gain additional control over the system, maximizing the HHG and minimizing the ionization. In other works these types of studies on pulse shaping have been done using genetic algorithms and other machine learning techniques [207]. Given the fact that our Kaufmann enhanced basis requires little computation time, optimization by such procedures is quite feasible.

Future works could also address the effects of the confinement by impenetrable barriers on HHG, taking advantage of the developed code's capabilities, with some slight modifications. For a confined hydrogen system the allowed k values, (see (5.23)), tend to appear in a nearly periodic manner, but the allowed energies come with increasing gap sizes. Consequently the confinement should have an effect on the energy gaps, and therefore the populations of different levels, suppressing or enhancing certain emission in frequencies.

We conclude that the apparition of the 3-peak structure on the third harmonic is related to the enabling of the 2p-2s transition by means of degeneracy breaking caused by the strong electric field, together with transitions to the d levels, due to their oscillator strengths. Both methods, the confined hydrogen model and Stochastically enhanced Kaufmann basis give a reasonable agreement on the HHG and ionization rate, despite it being not having eigenstates as accurate as the confined hydrogen model. The enhanced Kaufmann basis has the additional advantage of being compact, and gives good computational performance.

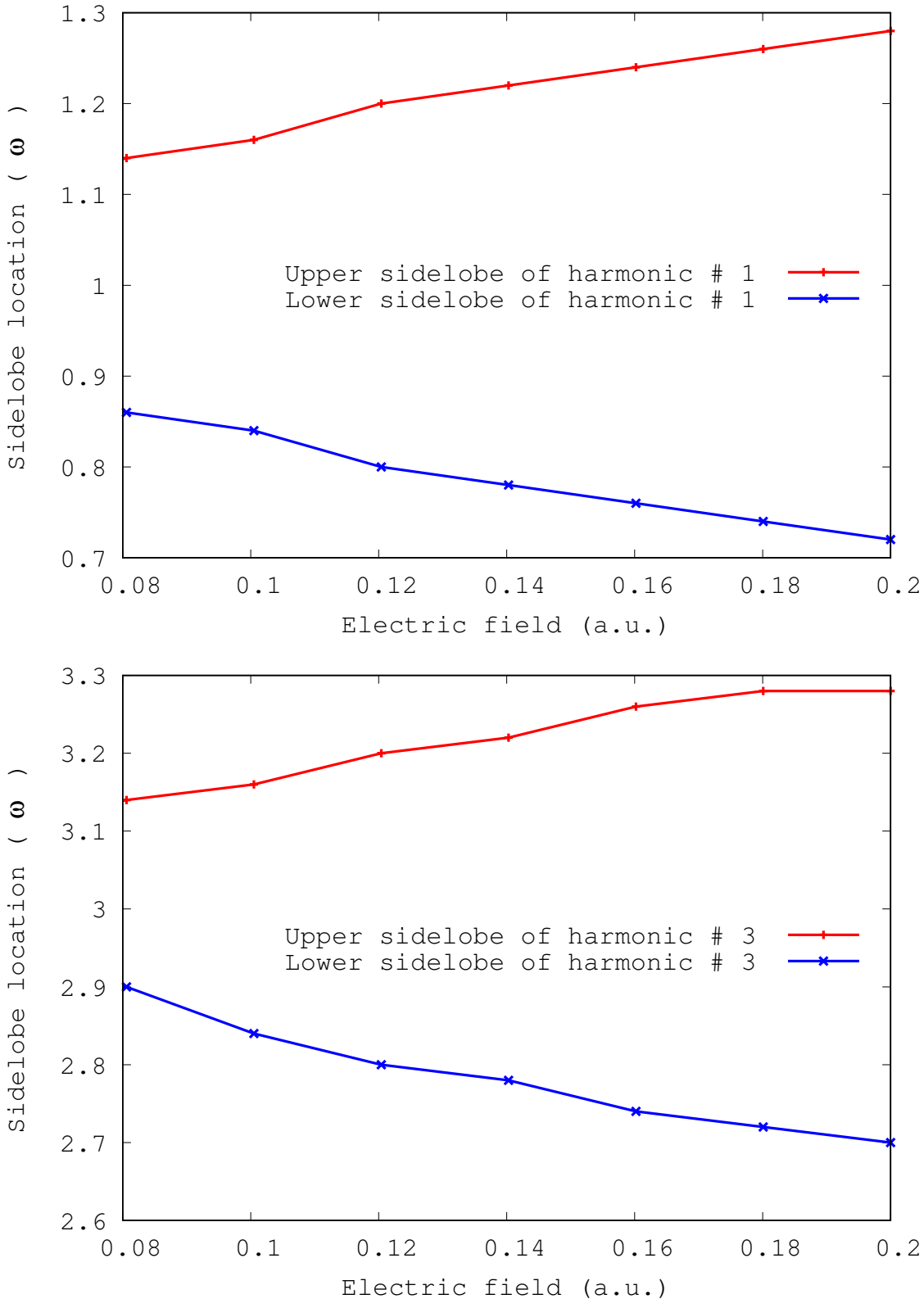

Figure 5.27: The upper and lower sidelobes of the fundamental (upper plot) and third harmonic (lower plot) are plotted for different values of the electric field. ω is normalized to the angular frequency of the fundamental harmonic.

The result could have implications for the study of HHG in systems that can be modeled as being hydrogen-like. The advantage of generating the Mollow sidebands is that they are tunable by altering the laser pulse shape and amplitude, although their limitation is set by the possibility of ionization due to high intensities. The observed peak structure could also be used as a test to see how degenerate are the eigenstates with quantum number $n = 2$ and indicate the presence of perturbations. Due to the strong dipole moment of the 2s-2p transition any slight change in the population due to external radiation can manifest itself in the HHG. The idea of controlling the HHG by degeneracy breaking can be further explored in future works by simulating a pump-probe scheme that drives the transitions between 2s and 2p, while at the same time triggering the 1s-2p transition.

Outlook

A natural extension for the Stochastically enhanced Kaufman basis is for single electron systems such as He^+ and other isoelectronic ions, as well as other systems that are modeled as hydrogen atoms such as positronium or excitons.

Using the Kaufmann basis directly for systems with more electrons is possible, although computationally expensive since the number of required functions grows very rapidly. For the case of Helium the representation of the unbound states is not easy for multiple reasons. Single active electron approximations are commonly used in Helium to describe its optical properties [208], but fail for strong intensities due to transitions into doubly excited states which are not stable [209]. Furthermore the Rydberg and unbound states are not easy to represent [210], and augmented quantum chemistry standard tabulated basis sets can become unsuitable for high intensities[211], making Helium hard to represent. However, these difficulties have prompted the recent development of exponentially tampered Gaussian sets, which are used in conjunction with complex scaling, [210, 211] with improved results. One new possibility for simulating Helium could then arise by using the latter method, instead of the Kaufman basis, in combination with the SVM.

On the other hand, the Kaufmann basis might have a better prospect for Lithium, which is commonly represented in terms of single active electron approximations. The Kaufmann basis itself has been previously extended for such representation [175]. However a drawback with the approach is that the overlaps of the basis functions can become large and difficult to handle with finite arithmetic. This is a consequence of the high excited states becomes close in energies and the solutions gaining high oscillatory behavior [175]. Its solely a numerical problem and not a problem of the basis set. Therefore it may be possible to use a Stochastically enhanced Kauffman basis to obtain Lithium states and further work would focus on handling any numerical issues properly.

CHAPTER 6

CONCLUSIONS AND FURTHER REMARKS

Benchmark calculations for small boson systems were obtained with good accuracy, and with potential for multiple applications such as the study of formation of Wigner crystals, Helium trimers, and Efimov states. These results have been considered very accurate and used for envelope theory in Refs.[212, 213]. The real limit for our present method comes from the number of permutations arising from the symmetry of the wavefunction.

We have proven the effectiveness of the SVM method to calculate accurate energies employing deformed Explicitly Correlated Gaussians for 3-electron systems in strong magnetic fields. This approach was capable of giving the lowest variational values in the literature up to date for these systems. This success is due to the fact that the exact solution of a charged particle in a magnetic field is given by a Gaussian function, the solution to the harmonic oscillator potential, which makes the convergence faster than the Hylleraas approach. Additionally, this method can be employed for any number of particles, being only limited by computational resources.

The stability of three-electron systems was studied using a non-relativistic Hamiltonian. The model is in agreement with the theoretical prediction of formation of magnetically induced He^{-}, which would be typically unstable. Furthermore the energies, ranges of stability and the corresponding ground state configurations were determined. The structure of the system was also studied, and compared to the other systems of the isoelectronic sequence. The different energy contributions of each term of the Hamiltonian were also shown in order to elucidate more of the underlying physics and the competition between the Coulomb forces and the magnetic ones. Our calculations revealed the existence of stable atomic states with unpaired spins with very strong diamagnetism, contrary to the typical cases where diamagnetism is overshadowed by paramagnetism. Nevertheless the model does not

account for the motion of the center of mass, as well as other effects that can alter the stability. Further studies can include some of the mentioned effects in the model. Another important aspect is the study of the electronic transitions and their wavelengths, which would be the experimentally observable quantities. Also, the formation of more complex systems like molecules or solids by means of paramagnetic bonding is another topic of recent interest than could be investigated. In particular the study of changes in stability of fermion systems, such as 2 positrons and 3 electrons, is another possible subject for further investigation. Other possibilities could include corrections due to non-homogeneous fields or using a periodic code to study the formation of long molecular chains.

For interactions with electric fields we have used a stochastically enhanced Kaufmann basis to show the appearance of Mollow sidebands upon the higher harmonics of the spectrum of the hydrogen atom. We have also determined the importance of the 2s-2p transition in the higher harmonics as well as the insufficiency of the 2-level model to correctly describe the peak structure. In weak field models the 2s-2p transition is not allowed because it has no energy difference, but with strong electric fields the degeneracy is broken, enabling the transition and reshaping the high harmonic Mollow sidebands. These results, to the best of our knowledge, have not been previously published. We further confirmed the results by the use of a confined hydrogen model, which has the correct form of the wavefunction for scattering states. Both methods give ionization levels with a reasonable agreement with each other and with those previously published for the same intensity. The results could have applications for HHG in systems that can be modeled as hydrogenic. The speed performance of the stochastically enhanced Kaufmann basis seems make the use of machine learning optimization algorithms feasible for the purpose of controlling the Mollow sidebands and ionization. Further works could address the simulations of more complex systems, such as He or Li, for which the extension of the present method is not straightforward, but other variations could be attempted.

BIBLIOGRAPHY

[1] Kalman Varga and J. A. Driscoll. *Computational Nanoscience*. Cambridge University Press, 2011.

[2] K. Varga and Y. Suzuki. Stochastic variational method with a correlated gaussian basis. *Phys. Rev. A*, 53:1907–1910, Mar 1996.

[3] Egil A. Hylleraas. The Schrödinger Two-Electron Atomic Problem. In Per-Olov Löwdin, editor, , volume 1 of *Advances in Quantum Chemistry*, pages 1–33. Academic Press, 1964.

[4] Jim Mitroy, Sergiy Bubin, Wataru Horiuchi, Yasuyuki Suzuki, Ludwik Adamowicz, Wojciech Cencek, Krzysztof Szalewicz, Jacek Komasa, D. Blume, and Kálmán Varga. Theory and application of explicitly correlated gaussians. *Rev. Mod. Phys.*, 85:693–749, May 2013.

[5] D.J. Griffiths. *Introduction to Quantum Mechanics*. Pearson international edition. Pearson Prentice Hall, 2005.

[6] Jorge A. Salas, Kalman Varga, Jia-An Yan, and Kirk H. Bevan. Electron talbot effect on graphene. *Phys. Rev. B*, 93:104305, Mar 2016.

[7] N. L. Guevara and A. V. Turbiner. Heliumlike and lithiumlike ionic sequences: Critical charges. *Phys. Rev. A*, 84:064501, Dec 2011.

[8] Dong Xiao, Oganov Artem R., Goncharov Alexander F., Stavrou Elissaios, Lobanov Sergey, Saleh Gabriele, Qian Guang-Rui, Zhu Qiang, Gatti Carlo, Deringer Volker L., Dronskowski Richard, Zhou Xiang-Feng, Prakapenka Vitali B., Konôpková Zuzana, Popov Ivan A., Boldyrev Alexander I., and Wang Hui-Tian. A stable com-

pound of helium and sodium at high pressure. *Nat Chem*, advance online publication, feb 2017.

[9] C. Kittel. *Introduction to Solid State Physics*. Wiley, 2004.

[10] Maksim Kunitski, Stefan Zeller, Jörg Voigtsberger, Anton Kalinin, Lothar Ph. H. Schmidt, Markus Schöffler, Achim Czasch, Wieland Schöllkopf, Robert E. Grisenti, Till Jahnke, Dörte Blume, and Reinhard Dörner. Observation of the Efimov state of the helium trimer. *Science*, 348(6234):551–555, 2015.

[11] Sergiy Bubin and Ludwik Adamowicz. Explicitly correlated gaussian calculations of the 2po rydberg spectrum of the lithium atom. *The Journal of Chemical Physics*, 136(13):–, 2012.

[12] Jim Mitroy, Sergiy Bubin, Wataru Horiuchi, Yasuyuki Suzuki, Ludwik Adamowicz, Wojciech Cencek, Krzysztof Szalewicz, Jacek Komasa, D. Blume, and Kálmán Varga. Theory and application of explicitly correlated gaussians. *Rev. Mod. Phys.*, 85:693–749, May 2013.

[13] Yasuyuki Suzuki and Kalman Varga. *Stochastic Variational Approach to Quantum-Mechanical Few-Body Problems*. Springer, 1998.

[14] Jiyun Kuang and C D Lin. Molecular integrals over spherical gaussian-type orbitals: I. *Journal of Physics B: Atomic, Molecular and Optical Physics*, 30(11):2529, 1997.

[15] K. Varga and Y. Suzuki. Precise solution of few-body problems with the stochastic variational method on a correlated gaussian basis. *Phys. Rev. C*, 52:2885–2905, Dec 1995.

[16] Zong-Chao Yan and G W F Drake. Computational methods for three-electron atomic systems in hylleraas coordinates. *Journal of Physics B: Atomic, Molecular and Optical Physics*, 30(21):4723, 1997.

[17] Mara Beln Ruiz. Hylleraas method for many-electron atoms. i. the hamiltonian. *International Journal of Quantum Chemistry*, 101(3):246–260, 2005.

[18] Toshikatsu Koga. Hylleraas wave functions revisited. *The Journal of Chemical Physics*, 96(2):1276–1279, 1992.

[19] Frederick W. King. Calculations on the ^{2}S ground states of some members of the li i isoelectronic series. *Phys. Rev. A*, 40:1735–1747, Aug 1989.

[20] Sven Larsson. Calculations on the ^2s ground state of the lithium atom using wave functions of hylleraas type. *Phys. Rev.*, 169:49–54, May 1968.

[21] J. Horne, J. A. Salas, and K. Varga. Energy and Structure of Few-Boson Systems. *Few-Body Systems*, 55(12):1245–1252, 2014.

[22] F. Dalfovo, S. Giorgini, L. P. Pitaevskii, and S. Stringari. Theory of bose-einstein condensation in trapped gases. *Rev. Mod. Phys.*, 71:463, 1999.

[23] E. Braaten and H.-W. Hammer. Universality in few-body systems with large scattering length. *Phys. Rep.*, 428:259, 2006.

[24] S. Giorgini, L. P. Pitaevskii, and S. Stringari. Theory of ultracold atomic fermi gases. *Rev. Mod. Phys.*, 80:1215, 2008.

[25] I. Bloch, J. Dalibard, and W. Zwerger. Many-body physics with ultracold gases. *Rev. Mod. Phys.*, 80:885, 2008.

[26] C. Chin, R. Grimm, P. Julienne, and E. Tiesinga. Feshbach resonances in ultracold gases. *Rev. Mod. Phys.*, 82:1225, 2010.

[27] Piatecki Swann and Krauth Werner. Efimov-driven phase transitions of the unitary Bose gas. *Nat Commun*, 5, mar 2014.

[28] Makotyn P., Klauss C. E., Goldberger D. L., Cornell E. A., and Jin D. S. Universal dynamics of a degenerate unitary Bose gas. *Nat Phys*, 10(2):116119, feb 2014.

[29] M. Gattobigio, A. Kievsky, and M. Viviani. Energy spectra of small bosonic clusters having a large two-body scattering length. *Phys. Rev. A*, 86:042513, Oct 2012.

[30] L. Platter, H. W. Hammer, and U. G. Meissner. Four-boson system with short-range interactions. *Phys. Rev. A*, 70:052101, 2004.

[31] H. W. Hammer and L. Platter. Universal properties of the four-body system with large scattering length. *Eur. Phys. J. A*, 32:113, 2007.

[32] J. von Stecher, J. P. D'Incao, and C. H. Greene. Signatures of universal four-body phenomena and their relation to the efimov effect. *Nature Phys.*, 5:417, 2009.

[33] J. P. D'Incao, J. von Stecher, and C. H. Greene. Universal four-boson states in ultracold molecular gases: Resonant effects in dimer-dimer collisions. *Phys. Rev. Lett.*, 103:033004, 2009.

[34] A. Deltuva. Shallow efimov tetramer as inelastic virtual state and resonant enhancement of the atom-trimer relaxation. *Europhys. Lett.*, 95:43002, 2011.

[35] A. Deltuva. Universality in bosonic dimer-dimer scattering. *Phys. Rev. A*, 84:022703, 2011.

[36] M. R. Hadizadeh, M. T. Yamashita, L. Tomio, A. Delfino, and T. Frederico. Scaling properties of universal tetramers. *Phys. Rev. Lett. (to appear)*, 2011.

[37] N. K. Timofeyuk. Convergence of the hyperspherical-harmonics expansion with increasing number of particles for bosonic systems. *Phys. Rev. A*, 86:032507, Sep 2012.

[38] M. Gattobigio, A. Kievsky, and M. Viviani. Six-bodies calculations using the hyperspherical harmonics method. *Few-Body Systems*, 54(5-6):657–666, 2013.

[39] T. Frederico, A. Delfino, M.R. Hadizadeh, Lauro Tomio, and M.T. Yamashita. Universality in four-boson systems. *Few-Body Systems*, 54(5-6):559–568, 2013.

[40] D. Blume and Chris H. Greene. Monte carlo hyperspherical description of helium cluster excited states. *The Journal of Chemical Physics*, 112(18):8053–8067, 2000.

[41] N. K. Timofeyuk. Improved procedure to construct a hyperspherical basis for the *n*-body problem: Application to bosonic systems. *Phys. Rev. C*, 78:054314, Nov 2008.

[42] Hiroya Suno and B. D. Esry. Adiabatic hyperspherical study of triatomic helium systems. *Phys. Rev. A*, 78:062701, Dec 2008.

[43] E. Hiyama and M. Kamimura. Variational calculation of ^{4}he tetramer ground and excited states using a realistic pair potential. *Phys. Rev. A*, 85:022502, Feb 2012.

[44] Tapan Kumar Das, Barnali Chakrabarti, and Sylvio Canuto. Use of correlated potential harmonic basis functions for the description of the 4he trimer and small clusters. *The Journal of Chemical Physics*, 134(16):–, 2011.

[45] E Nielsen, D V Fedorov, and A S Jensen. The structure of the atomic helium trimers: halos and efimov states. *Journal of Physics B: Atomic, Molecular and Optical Physics*, 31(18):4085, 1998.

[46] Vladimir Roudnev and Michael Cavagnero. Benchmark helium dimer and trimer calculations with a public few-body code. *Journal of Physics B: Atomic, Molecular and Optical Physics*, 45(2):025101, 2012.

[47] F. Werner and Y. Castin. Unitary quantum three-body problem in a harmonic trap. *Phys. Rev. Lett.*, 97:150401, 2006.

[48] Ioannis Brouzos and Peter Schmelcher. Controlled excitation and resonant acceleration of ultracold few-boson systems by driven interactions in a harmonic trap. *Phys. Rev. A*, 85:033635, Mar 2012.

[49] M. Thgersen, D. V. Fedorov, and A. S. Jensen. N-body efimov states of trapped bosons. *EPL (Europhysics Letters)*, 83(3):30012, 2008.

[50] M. Gattobigio, A. Kievsky, and M. Viviani. Spectra of helium clusters with up to six atoms using soft-core potentials. *Phys. Rev. A*, 84:052503, Nov 2011.

[51] E. Nielsen, D.V. Fedorov, A.S. Jensen, and E. Garrido. The three-body problem with short-range interactions. *Physics Reports*, 347(5):373–459, 2001.

[52] A. R. Janzen and R. A. Aziz. An accurate potential energy curve for helium based on ab initio calculations. *The Journal of Chemical Physics*, 107(3):914–919, 1997.

[53] Ronald A. Aziz and Martin J. Slaman. An examination of ab initio results for the helium potential energy curve. *The Journal of Chemical Physics*, 94(12):8047–8053, 1991.

[54] A. Kievsky, E. Garrido, C. Romero-Redondo, and P. Barletta. The Helium Trimer with Soft-Core Potentials. *Few-Body Systems*, 51(2):259–269, 2011.

[55] V. Efimov. Energy levels arising from resonant 2-body forces in a 3-body system. *Phys. Lett.*, 33B:563, 1970.

[56] Francesca Ferlaino and Rudolf Grimm. Trend: Forty years of Efimov physics: How a bizarre prediction turned into a hot topic. *Physics*, 3, Jan 2010.

[57] V Efimov. Weakly-bound states of three resonantly-interacting particles. *Sov. J. Nucl. Phys*, 12(589):101, 1971.

[58] T. Kraemer, M. Mark, P. Waldburger, J. G. Danzl, C. Chin, B. Engeser, A. D. Lange, K. Pilch, A. Jaakkola, H.-C. Nägerl, and R. Grimm. Evidence for efimov quantum states in an ultracold gas of caesium atoms. *Nature*, 440(7082):315–318, Mar 2006.

[59] F. Ferlaino, S. Knoop, M. Berninger, W. Harm, J. P. D'Incao, H.-C. Nägerl, and R. Grimm. Evidence for universal four-body states tied to an efimov trimer. *Phys. Rev. Lett.*, 102:140401, 2009.

[60] S. E. Pollack, D. Dries, and R. G. Hulet. Universality in three- and four-body bound states of ultracold atoms. *Science*, 326:1683, 2009.

[61] Bo Huang, Leonid A. Sidorenkov, Rudolf Grimm, and Jeremy M. Hutson. Observation of the second triatomic resonance in efimov's scenario. *Phys. Rev. Lett.*, 112:190401, May 2014.

[62] Sólyom, J. Wigner crystals: New realizations of an old idea. *EPJ Web of Conferences*, 78:01009, 2014.

[63] Emmanuel Rousseau, Dmitri Ponarin, Likourgos Hristakos, Olivier Avenel, Eric Varoquaux, and Yuri Mukharsky. Addition spectra of wigner islands of electrons on superfluid helium. *Phys. Rev. B*, 79:045406, Jan 2009.

[64] K. Varga, P. Navratil, J. Usukura, and Y. Suzuki. Stochastic variational approach to few-electron artificial atoms. *Phys. Rev. B*, 63:205308, Apr 2001.

[65] J. A. Salas and K. Varga. He^- in a magnetic field: Structure and stability. *Phys. Rev. A*, 89:052501, May 2014. http://dx.doi.org/10.1103/PhysRevA.89.052501.

[66] J. A. Salas, I. Pelaschier, and K. Varga. Three-electron atoms and ions in a magnetic field. *Phys. Rev. A*, 92:033401, Sep 2015. https://doi.org/10.1103/PhysRevA.92.033401.

[67] Victor G. Bezchastnov, Peter Schmelcher, and Lorenz S. Cederbaum. Bound states of negatively charged ions induced by a magnetic field. *Phys. Rev. A*, 61:052512, Apr 2000.

[68] Victor G. Bezchastnov, Lorenz S. Cederbaum, and Peter Schmelcher. Stability of negatively charged ions moving in a magnetic field. *Phys. Rev. Lett.*, 86:5450–5453, Jun 2001.

[69] Victor G. Bezchastnov, Peter Schmelcher, and Lorenz S. Cederbaum. Magnetically induced anions. *Phys. Chem. Chem. Phys.*, 5:4981–4997, 2003.

[70] Victor G. Bezchastnov, Peter Schmelcher, and Lorenz S. Cederbaum. Quantum states of magnetically induced anions. *Phys. Rev. Lett.*, 95:113002, Sep 2005.

[71] Victor G. Bezchastnov, Peter Schmelcher, and Lorenz S. Cederbaum. Magnetically induced anions: Classical dynamics. *Phys. Rev. A*, 65:042512, Apr 2002.

[72] Cleanthes A. Nicolaides, Yannis Komninos, and Donald R. Beck. Bound states and decay mechanisms of he^-. *Phys. Rev. A*, 24:1103–1106, Aug 1981.

[73] J. Avron, I. Herbst, and B. Simon. Formation of negative ions in magnetic fields. *Phys. Rev. Lett.*, 39:1068–1070, Oct 1977.

[74] A. W. Weiss. Configuration interaction in simple atomic systems. *Phys. Rev.*, 122:1826–1836, Jun 1961.

[75] E. Holøien and S. Geltman. Variational calculations for quartet states of three-electron atomic systems. *Phys. Rev.*, 153:81–86, Jan 1967.

[76] J. Avron, I. Herbst, and B. Simon. Formation of negative ions in magnetic fields. *Phys. Rev. Lett.*, 39:1068–1070, Oct 1977.

[77] Victor G. Bezchastnov, Peter Schmelcher, and Lorenz S. Cederbaum. Theory of magnetically induced anions. *Phys. Rev. A*, 75:052507, May 2007.

[78] M. V. Ivanov and P. Schmelcher. Ground state of the lithium atom in strong magnetic fields. *Phys. Rev. A*, 57:3793–3800, May 1998.

[79] Victor G. Bezchastnov, Peter Schmelcher, and Lorenz S. Cederbaum. Magnetically induced anions. *Phys. Chem. Chem. Phys.*, 5:4981–4997, 2003.

[80] R. Cohen, J. Lodenquai, and M. Ruderman. Atoms in superstrong magnetic fields. *Phys. Rev. Lett.*, 25:467–469, Aug 1970.

[81] Roger G. Newton. Atoms in superstrong magnetic fields. *Phys. Rev. D*, 3:626–627, Jan 1971.

[82] D. H. Constantinescu and P. Rehák. Ground state of atoms and molecules in a superstrong magnetic field. *Phys. Rev. D*, 8:1693–1706, Sep 1973.

[83] J. C. Kemp, J. B. Swedlund, J. D. Landstreet, and J. R. P. Angel. Discovery of circularly polarized light from a white dwarf. *Astrophys. J. Lett.*, 161:L77, aug 1970.

[84] J. R. P. Angel, E. F. Borra, and J. D Landstreet. The magnetic fields of white dwarfs. *Astrophys. J.*, 45:457–474, March 1981.

[85] J. Truemper, W. Pietsch, C. Reppin, W. Voges, R. Staubert, and E. Kendziorra. Evidence for strong cyclotron line emission in the hard X-ray spectrum of Hercules X-1. *Astrophys. J. Lett.*, 219:L105–L110, February 1978.

[86] Christopher Thompson and Robert C. Duncan. The soft gamma repeaters as very strongly magnetized neutron stars. ii. quiescent neutrino, x-ray, and alfvn wave emission. *The Astrophysical Journal*, 473(1):322, 1996.

[87] Rudolf A. Treumann, Wolfgang Baumjohann, and André Balogh. The strongest magnetic fields in the universe: how strong can they become? *Frontiers in Physics*, 2:59, 2014.

[88] The largest and highest powered magnet lab in the world - maglab. https://nationalmaglab.org/.

[89] Glenn Elert. The physics factbook.

[90] Jianjun Fang, Helena Pais, Sidney Avancini, and Constan ça Providência. Larger and more heterogeneous neutron star crusts: A result of strong magnetic fields. *Phys. Rev. C*, 94:062801, Dec 2016.

[91] N. Afram and S. V. Berdyugina. Molecules as magnetic probes of starspots. *A&A*, 576:A34, 2015.

[92] E. I. Tellgren, A. M. Teale, J. W. Furness, K. K. Lange, U. Ekstrm, and T. Helgaker. Non-perturbative calculation of molecular magnetic properties within current-density functional theory. *The Journal of Chemical Physics*, 140(3):–, 2014.

[93] Erik I. Tellgren and Heike Fliegl. Non-perturbative treatment of molecules in linear magnetic fields: Calculation of anapole susceptibilities. *The Journal of Chemical Physics*, 139(16):–, 2013.

[94] Erik I. Tellgren, Alessandro Soncini, and Trygve Helgaker. Nonperturbative ab initio calculations in strong magnetic fields using london orbitals. *The Journal of Chemical Physics*, 129(15):–, 2008.

[95] Kai K. Lange, E. I. Tellgren, M. R. Hoffmann, and T. Helgaker. A paramagnetic bonding mechanism for diatomics in strong magnetic fields. *Science*, 337(6092):327–331, 2012.

[96] Erik I. Tellgren, Simen S. Reine, and Trygve Helgaker. Analytical giao and hybrid-basis integral derivatives: application to geometry optimization of molecules in strong magnetic fields. *Phys. Chem. Chem. Phys.*, 14:9492–9499, 2012.

[97] Erik I. Tellgren, Trygve Helgaker, and Alessandro Soncini. Non-perturbative magnetic phenomena in closed-shell paramagnetic molecules. *Phys. Chem. Chem. Phys.*, 11:5489–5498, 2009.

[98] Sarah Reimann, Ulf Ekstrom, Stella Stopkowicz, Andrew M. Teale, Alex Borgoo, and Trygve Helgaker. The importance of current contributions to shielding constants in density-functional theory. *Phys. Chem. Chem. Phys.*, 17:18834–18842, 2015.

[99] Ryan D. Reynolds and Toru Shiozaki. Fully relativistic self-consistent field under a magnetic field. *Phys. Chem. Chem. Phys.*, 17:14280–14283, 2015.

[100] Hctor Medel Cobaxin and Alexander Alijah. Vibrating H3+ in a Uniform Magnetic Field. *The Journal of Physical Chemistry A*, 117(39):98719881, 2013. PMID: 23461566.

[101] Yu. P. Kravchenko and M. A. Liberman. Hydrogen molecule in a strong parallel magnetic field. *Phys. Rev. A*, 57:3403–3418, May 1998.

[102] D. Baye and M. Vincke. Center-of-mass problem in a magnetic field: Unified treatment of charged and neutral systems. *Phys. Rev. A*, 42:391–396, Jul 1990.

[103] G. Vignale and Mark Rasolt. Density-functional theory in strong magnetic fields. *Phys. Rev. Lett.*, 59:2360–2363, Nov 1987.

[104] C. Riva, F. M. Peeters, and K. Varga. Excitons and charged excitons in semiconductor quantum wells. *Phys. Rev. B*, 61:13873–13881, May 2000.

[105] C. Riva, F. M. Peeters, and K. Varga. Magnetic field dependence of the energy of negatively charged excitons in semiconductor quantum wells. *Phys. Rev. B*, 63:115302, Feb 2001.

[106] C. Riva, F. M. Peeters, and K. Varga. Positively charged magnetoexcitons in a semiconductor quantum well. *Phys. Rev. B*, 64:235301, Nov 2001.

[107] Ashoori R. C. Electrons in artificial atoms. *Nature*, 379(6564):413419, feb 1996. 10.1038/379413a0.

[108] K. L. Litvinenko, M. Pang, Juerong Li, E. Bowyer, H. Engelkamp, V. B. Shuman, L. M. Portsel, A. N. Lodygin, Yu. A. Astrov, S. G. Pavlov, H.-W. Hübers, C. R. Pidgeon, and B. N. Murdin. High-field impurity magneto-optics of si:se. *Phys. Rev. B*, 90:115204, Sep 2014.

[109] Victor G. Bezchastnov, Lorenz S. Cederbaum, and Peter Schmelcher. Magnetically induced anions: Basic theory. *Phys. Rev. A*, 65:032501, Feb 2002.

[110] C. F. Bunge and A. V. Bunge. Calculations of atomic electron affinities. *Int. J. Quantum Chem.*, 14(S12):345 – 355, 1978.

[111] V S Popov and B M Karnakov. Hydrogen atom in a strong magnetic field. *Physics-Uspekhi*, 57(3):257, 2014.

[112] W. Becken and P. Schmelcher. Higher-angular-momentum states of the helium atom in a strong magnetic field. *Phys. Rev. A*, 63:053412, Apr 2001.

[113] W. Becken and P. Schmelcher. Electromagnetic transitions of the helium atom in a strong magnetic field. *Phys. Rev. A*, 65:033416, Feb 2002.

[114] O.-A. Al-Hujaj and P. Schmelcher. Helium in superstrong magnetic fields. *Phys. Rev. A*, 67:023403, Feb 2003.

[115] Omar-Alexander Al-Hujaj and Peter Schmelcher. Electromagnetic transitions of the helium atom in superstrong magnetic fields. *Phys. Rev. A*, 68:053403, Nov 2003.

[116] Omar-Alexander Al-Hujaj and Peter Schmelcher. Lithium in strong magnetic fields. *Phys. Rev. A*, 70:033411, Sep 2004.

[117] Omar-Alexander Al-Hujaj and Peter Schmelcher. Beryllium in strong magnetic fields. *Phys. Rev. A*, 70:023411, Aug 2004.

[118] M.V. Ivanov and P. Schmelcher. The beryllium atom and beryllium positive ion in strong magnetic fields. *The European Physical Journal D - Atomic, Molecular, Optical and Plasma Physics*, 14(3):279–288, 2001.

[119] Anand Thirumalai, Steven J. Desch, and Patrick Young. Carbon atom in intense magnetic fields. *Phys. Rev. A*, 90:052501, Nov 2014.

[120] M. V. Ivanov and P. Schmelcher. Ground states of h, he,. . . , ne, and their singly positive ions in strong magnetic fields: The high-field regime. *Phys. Rev. A*, 61:022505, Jan 2000.

[121] P Proschel, W Rosner, G Wunner, H Ruder, and H Herold. Hartree-Fock calculations for atoms in strong magnetic fields. I. Energy levels of two-electron systems. *Journal of Physics B: Atomic and Molecular Physics*, 15(13):1959, 1982.

[122] Yin Tang, Liming Wang, Xuanyu Song, Xiaofeng Wang, Z.-C. Yan, and Haoxue Qiao. Bound-state energies of lithium in magnetic fields using hylleraas basis functions. *Phys. Rev. A*, 87:042518, Apr 2013.

[123] A. V. Turbiner and J. C. Lopez Vieyra. Stable he^- can exist in a strong magnetic field. *Phys. Rev. Lett.*, 111:163003, Oct 2013.

[124] M Hesse and D Baye. Helium atoms in a strong magnetic field studied with the lagrange-mesh method. *J. Phys. B: At. Mol. Opt. Phys.*, 37:3937, Oct 2004.

[125] Sebastian Boblest, Christoph Schimeczek, and Günter Wunner. Ground states of helium to neon and their ions in strong magnetic fields. *Phys. Rev. A*, 89:012505, Jan 2014.

[126] Christoph Schimeczek, Sebastian Boblest, Dirk Meyer, and Günter Wunner. Atomic ground states in strong magnetic fields: Electron configurations and energy levels. *Phys. Rev. A*, 88:012509, Jul 2013.

[127] C. Schimeczek and G. Wunner. Accurate 2d finite element calculations for hydrogen in magnetic fields of arbitrary strength. *Computer Physics Communications*, 185(2):614 – 621, 2014.

[128] Anand Thirumalai and Jeremy S. Heyl. Two-dimensional pseudospectral hartree-fock method for low-z atoms in intense magnetic fields. *Phys. Rev. A*, 89:052522, May 2014.

[129] Haoxue Qiao and Baiwen Li. Calculations of lithium in magnetic fields with a modified freezing full-core method. *Phys. Rev. A*, 62:033401, Aug 2000.

[130] J.E. Avron, I.W. Herbst, and B. Simon. Schrdinger operators with magnetic fields. *Communications in Mathematical Physics*, 79(4):529–572, 1981.

[131] L. B. Zhao and P. C. Stancil. B-spline algorithm for magnetized multielectron atomic structures. *Phys. Rev. A*, 77:035401, Mar 2008.

[132] C. Schimeczek and G. Wunner. Accurate 2d finite element calculations for hydrogen in magnetic fields of arbitrary strength. *Computer Physics Communications*, 185(2):614 – 621, 2014.

[133] Yu. P. Kravchenko, M. A. Liberman, and B. Johansson. Exact solution for a hydrogen atom in a magnetic field of arbitrary strength. *Phys. Rev. A*, 54:287–305, Jul 1996.

[134] D Baye, M Vincke, and M Hesse. Simple and accurate calculations on a lagrange mesh of the hydrogen atom in a magnetic field. *Journal of Physics B: Atomic, Molecular and Optical Physics*, 41(5):055005, 2008.

[135] W Becken et al. The helium atom in a strong magnetic field. *J. Phys. B: At. Mol. Opt. Phys.*, 32:1557, Mar 1999.

[136] W Becken and P Schmelcher. Non-zero angular momentum states of the helium atom in a strong magnetic field. *J. Phys. B: At. Mol. Opt. Phys.*, 33:545, Feb 2000.

[137] Zhao Ji-Jun et al. Accurate calculations of the helium atom in magnetic fields. *Chinese Phys. B*, 19:113102, Nov 2010.

[138] O.-A. Al-Hujaj and P. Schmelcher. Ground and excited states of the hydrogen negative ion in strong magnetic fields. *Phys. Rev. A*, 61:063413, May 2000.

[139] Victor G. Bezchastnov, Peter Schmelcher, and Lorenz S. Cederbaum. Bound states of negatively charged ions induced by a magnetic field. *Phys. Rev. A*, 61:052512, Apr 2000.

[140] Victor G. Bezchastnov, Lorenz S. Cederbaum, and Peter Schmelcher. Magnetically induced anions: Basic theory. *Phys. Rev. A*, 65:032501, Feb 2002.

[141] Victor G. Bezchastnov, Peter Schmelcher, and Lorenz S. Cederbaum. Quantum states of magnetically induced anions. *Phys. Rev. Lett.*, 95:113002, Sep 2005.

[142] Victor G. Bezchastnov, Lorenz S. Cederbaum, and Peter Schmelcher. Stability of negatively charged ions moving in a magnetic field. *Phys. Rev. Lett.*, 86:5450–5453, Jun 2001.

[143] Victor G. Bezchastnov, Peter Schmelcher, and Lorenz S. Cederbaum. Magnetically induced anions: Classical dynamics. *Phys. Rev. A*, 65:042512, Apr 2002.

[144] Victor G. Bezchastnov, Peter Schmelcher, and Lorenz S. Cederbaum. Theory of magnetically induced anions. *Phys. Rev. A*, 75:052507, May 2007.

[145] Zhao Ji-Jun, Wang Xiao-Feng, and Qiao Hao-Xue. High accuracy calculation of the hydrogen negative ion in strong magnetic fields. *Chinese Physics B*, 20(5):053101, 2011.

[146] M. V. Ivanov and P. Schmelcher. Ground state of the lithium atom in strong magnetic fields. *Phys. Rev. A*, 57:3793–3800, May 1998.

[147] Xiaofeng Wang and Haoxue Qiao. Full-core-plus-correlation method in cylindrical coordinates: Lithium atom in strong magnetic fields. *Phys. Rev. A*, 75:033421, Mar 2007.

[148] Matthew D. Jones, Gerardo Ortiz, and David M. Ceperley. Hartree-fock studies of atoms in strong magnetic fields. *Phys. Rev. A*, 54:219–231, Jul 1996.

[149] Zach Medin and Dong Lai. Density-functional-theory calculations of matter in strong magnetic fields. i. atoms and molecules. *Phys. Rev. A*, 74:062507, Dec 2006.

[150] Wuming Zhu, Liang Zhang, and S. B. Trickey. Comparative studies of density-functional approximations for light atoms in strong magnetic fields. *Phys. Rev. A*, 90:022504, Aug 2014.

[151] Anand Thirumalai and Jeremy S. Heyl. Chapter Five - Energy Levels of Light Atoms in Strong Magnetic Fields. In Paul R. Berman Ennio Arimondo and Chun C. Lin, editors, , volume 63 of *Advances In Atomic, Molecular, and Optical Physics*, pages 323–358. Academic Press, 2014.

[152] Sebastian Boblest, Christoph Schimeczek, and Günter Wunner. Ground states of helium to neon and their ions in strong magnetic fields. *Phys. Rev. A*, 89:012505, Jan 2014.

[153] A. V. Turbiner and J. C. Lopez Vieyra. Stable he^- can exist in a strong magnetic field. *Phys. Rev. Lett.*, 111:163003, Oct 2013.

[154] C. Kittel. *Introduction to Solid State Physics*, chapter 11. Wiley, 2004.

[155] HA Bethe and EE Salpeter. *Quantum mechanics of one-and two-electron atoms*. Plenum Publishing Corp., New York, 1977.

[156] Turker Topcu and Francis Robicheaux. Dichotomy between tunneling and multiphoton ionization in atomic photoionization: Keldysh parameter γ versus scaled frequency Ω. *Phys. Rev. A*, 86:053407, Nov 2012.

[157] M. Lewenstein, Ph. Balcou, M. Yu. Ivanov, Anne L'Huillier, and P. B. Corkum. Theory of high-harmonic generation by low-frequency laser fields. *Phys. Rev. A*, 49:2117–2132, Mar 1994.

[158] A. D. Bandrauk, S. Chelkowski, D. J. Diestler, J. Manz, and K.-J. Yuan. Quantum simulation of high-order harmonic spectra of the hydrogen atom. *Phys. Rev. A*, 79:023403, Feb 2009.

[159] Yuqing Xia and Agnieszka Jaron-Becker. Mollow sidebands in high order harmonic spectra of molecules. *Opt. Express*, 24(5):4689–4697, Mar 2016.

[160] T. Tritschler, O. D. Mücke, and M. Wegener. Extreme nonlinear optics of two-level systems. *Phys. Rev. A*, 68:033404, Sep 2003.

[161] P M Farrell and W R MacGillivray. On the consistency of Rabi frequency calculations. *Journal of Physics A: Mathematical and General*, 28(1):209, 1995.

[162] Dr. Rdiger Paschotta. Rabi oscillations, Feb 2017.

[163] B. R. Mollow. Power spectrum of light scattered by two-level systems. *Phys. Rev.*, 188:1969–1975, Dec 1969.

[164] UlhaqA., WeilerS., UlrichS. M., RoszbachR., JetterM., and MichlerP. Cascaded single-photon emission from the Mollow triplet sidebands of a quantum dot. *Nat Photon*, 6(4):238–242, Apr 2012. 10.1038/nphoton.2012.23.

[165] O. D. Mücke, T. Tritschler, M. Wegener, U. Morgner, and F. X. Kärtner. Signatures of carrier-wave rabi flopping in gaas. *Phys. Rev. Lett.*, 87:057401, Jul 2001.

[166] Qingyi Li, Zhiyuan Zhang, Yunfeng Zhang, Suyu Li, Fuming Guo, and Yujun Yang. Light emission induced by an xuv laser pulse interacting resonantly with atomic hydrogen. *Journal of Physics B: Atomic, Molecular and Optical Physics*, 49(1):015003, 2016.

[167] Flagg E. B., Muller A., Robertson J. W., Founta S., Deppe D. G., Xiao M., Ma W., Salamo G. J., and Shih C. K. Resonantly driven coherent oscillations in a solid-state quantum emitter. *Nat Phys*, 5(3):203–207, Mar 2009. 10.1038/nphys1184.

[168] M. F. Ciappina, J. A. Pérez-Hernández, A. S. Landsman, T. Zimmermann, M. Lewenstein, L. Roso, and F. Krausz. Carrier-wave rabi-flopping signatures in high-order harmonic generation for alkali atoms. *Phys. Rev. Lett.*, 114:143902, Apr 2015.

[169] Hyochul Kim, Thomas C. Shen, Kaushik Roy-Choudhury, Glenn S. Solomon, and Edo Waks. Resonant interactions between a mollow triplet sideband and a strongly coupled cavity. *Phys. Rev. Lett.*, 113:027403, Jul 2014.

[170] Jiahua Li, Rong Yu, Chunling Ding, Duo Zhang, and Ying Wu. Enhanced harmonic generation and carrier-envelope phase-dependent effects in cavity quantum electrodynamics. *Phys. Rev. A*, 92:013849, Jul 2015.

[171] Andrey V. Soldatov. Laser frequency down-conversion by means of a monochromatically driven two-level system. *Modern Physics Letters B*, 30(27):1650331, 2016.

[172] J. Feist, S. Nagele, R. Pazourek, E. Persson, B. I. Schneider, L. A. Collins, and J. Burgdörfer. Nonsequential two-photon double ionization of helium. *Phys. Rev. A*, 77:043420, Apr 2008.

[173] Cody Covington, Daniel Kidd, Justin Gilmer, and Kálmán Varga. Simulation of electron dynamics subject to intense laser fields using a time-dependent volkov basis. *Phys. Rev. A*, 95:013414, Jan 2017.

[174] B M Nestmann and S D Peyerimhoff. Optimized Gaussian basis sets for representation of continuum wavefunctions. *Journal of Physics B: Atomic, Molecular and Optical Physics*, 23(22):L773, 1990.

[175] K Kaufmann, W Baumeister, and M Jungen. Universal Gaussian basis sets for an optimum representation of Rydberg and continuum wavefunctions. *Journal of Physics B: Atomic, Molecular and Optical Physics*, 22(14):2223, 1989.

[176] *NIST Digital Library of Mathematical Functions*. http://dlmf.nist.gov/, Release 1.0.14 of 2016-12-21. F. W. J. Olver, A. B. Olde Daalhuis, D. W. Lozier, B. I. Schneider, R. F. Boisvert, C. W. Clark, B. R. Miller and B. V. Saunders, eds.

[177] N Aquino and R A Rojas. The confined hydrogen atom: a linear variational approach. *European Journal of Physics*, 37(1):015401, 2016.

[178] J. Humblet. Bessel function expansions of coulomb wave functions. *Journal of Mathematical Physics*, 26(4):656–659, 1985.

[179] J. Boersma. Expansions for Coulomb wave functions. *Mathematics of Computation*, 23(105):51–51, Jan 1969.

[180] Learner A and Robson BA. Coulomb Wave Functions. *Australian Journal of Physics*, 11(1):138–142, Mar 1958.

[181] E Hiyama, Y Kino, and M Kamimura. Gaussian expansion method for few-body systems. *Progress in Particle and Nuclear Physics*, 51(1):223–307, 2003.

[182] E Hiyama, Y Kino, and M Kamimura. Gaussian expansion method for few-body systems. *Progress in Particle and Nuclear Physics*, 51(1):223–307, Jan 2003.

[183] Alexis Chacón, Marcelo F. Ciappina, and Alvaro Peralta Conde. High-order harmonic generation enhanced by coherent population return. *The European Physical Journal D*, 69(5):133, 2015.

[184] Eleonora Luppi and Martin Head-Gordon. The role of rydberg and continuum levels in computing high harmonic generation spectra of the hydrogen atom using time-dependent configuration interaction. *The Journal of Chemical Physics*, 139(16):164121, 2013.

[185] Bruno Blaive and Michel Cadilhac. A comparison of the hydrogenlike dipole radial matrix elements with overlap integrals and a step toward explicit expressions of the multipole matrix elements. *Journal of Physics B: Atomic, Molecular and Optical Physics*, 42(16):165002, 2009.

[186] L. M. Ugray and R. C. Shiell. Elucidating fermi's golden rule via bound-to-bound transitions in a confined hydrogen atom. *American Journal of Physics*, 81(3):206–210, 2013.

[187] N. Aquino, G. Campoy, and H. E. Montgomery. Highly accurate solutions for the confined hydrogen atom. *International Journal of Quantum Chemistry*, 107(7):1548–1558, 2007.

[188] M. Galassi et al. GNU Scientific Library reference manual.

[189] Whittaker M function. https://www.mathworks.com/help/symbolic/whittakerm.html.

[190] Fredrik Johansson et al. *mpmath: a Python library for arbitrary-precision floating-point arithmetic (version 0.18)*, December 2013. `http://mpmath.org/`.

[191] S.H. Patil and Y.P. Varshni. Properties of confined hydrogen and helium atoms. volume 57 of *Advances in Quantum Chemistry*, pages 1 – 24. Academic Press, 2009.

[192] Kjell Bockasten. Mean values of powers of the radius for hydrogenic electron orbits. *Phys. Rev. A*, 9:1087–1089, Mar 1974.

[193] A.V. Oppenheim, R.W. Schafer, and J.R. Buck. *Discrete-time Signal Processing*, chapter 10. Prentice Hall international editions. Prentice Hall, 1999.

[194] Numpy Blackman window, Jan 2017. NumPy v1.12 Manual.

[195] Blackman window - MATLAB. https://www.mathworks.com/help/signal/ref/blackman.html.

[196] Alec F. White, Chiara Josephine Heide, Peter Saalfrank, Martin Head-Gordon, and Eleonora Luppi. Computation of high-harmonic generation spectra of the hydrogen molecule using time-dependent configuration-interaction. *Molecular Physics*, 8976(January 2016):1–10, dec 2015.

[197] Stefan Klinkusch, Peter Saalfrank, and Tillmann Klamroth. Laser-induced electron dynamics including photoionization: A heuristic model within time-dependent configuration interaction theory. *The Journal of Chemical Physics*, 131(11):114304, sep 2009.

[198] U. V. Riss and H.D. Meyer. Investigation on the reflection and transmission properties of complex absorbing potentials. *The Journal of Chemical Physics*, 105(4):1409–1419, 1996.

[199] Eleonora Luppi and Martin Head-Gordon. The role of Rydberg and continuum levels in computing high harmonic generation spectra of the hydrogen atom using time-dependent configuration interaction. *Journal of Chemical Physics*, 139(16), 2013.

[200] Pascal Krause, Jason A. Sonk, and H. Bernhard Schlegel. Strong field ionization rates simulated with time-dependent configuration interaction and an absorbing potential. *The Journal of Chemical Physics*, 140(17):174113, May 2014.

[201] Emanuele Coccia and Eleonora Luppi. Optimal-continuum and multicentered Gaus-

sian basis sets for high-harmonic generation spectroscopy. *Theoretical Chemistry Accounts*, 135(2):43, Feb 2016.

[202] Emanuele Coccia, Bastien Mussard, Marie Labeye, Jrmie Caillat, Richard Taeb, Julien Toulouse, and Eleonora Luppi. Gaussian continuum basis functions for calculating high-harmonic generation spectra. *International Journal of Quantum Chemistry*, 116(14):1120–1131, 2016.

[203] Kálmán Varga. Time-dependent density functional study of transport in molecular junctions. *Phys. Rev. B*, 83:195130, May 2011.

[204] Zeng Si-Liang, Zou Shi-Yang, and Yan Jun. Generalized pseudospectral method for solving the time-dependent schrdinger equation involving the coulomb potential. *Chinese Physics Letters*, 26(5):053202, 2009.

[205] Emanuele Coccia and Eleonora Luppi. Optimal-continuum and multicentered gaussian basis sets for high-harmonic generation spectroscopy. *Theoretical Chemistry Accounts*, 135(2):43, 2016.

[206] Dejan B. Milosevic. Theoretical analysis of high-order harmonic generation from a coherent superposition of states. *J. Opt. Soc. Am. B*, 23(2):308–317, Feb 2006.

[207] E. Balogh, B. Bódi, V. Tosa, E. Goulielmakis, K. Varjú, and P. Dombi. Genetic optimization of attosecond-pulse generation in light-field synthesizers. *Physical Review A*, 90(2):023855, Aug 2014.

[208] H.A. Bethe and E.E. Salpeter. *Quantum mechanics of one- and two-electron atoms*. Springer, 1957.

[209] Armin Scrinzi and Bernard Piraux. Two-electron atoms in short intense laser pulses. *Phys. Rev. A*, 58:1310–1321, Aug 1998.

[210] Petra Ruth Kaprlov-nsk, Jan mydke, and Svatopluk Civi. Excitation of helium rydberg states and doubly excited resonances in strong extreme ultraviolet fields: Full-dimensional quantum dynamics using exponentially tempered gaussian basis sets. *The Journal of Chemical Physics*, 139(10):104314, 2013.

[211] Petra Ruth Kaprlov-nsk and Jan mydke. Gaussian basis sets for highly excited and resonance states of helium. *The Journal of Chemical Physics*, 138(2):024105, 2013.

[212] Claude Semay. Numerical Tests of the Envelope Theory for Few-Boson Systems. *Few-Body Systems*, 56(4):149–156, 2015.

[213] Claude Semay. Improvement of the envelope theory with the dominantly orbital state method. *The European Physical Journal Plus*, 130(7):156, 2015.